Title

Synthesis of Conductive Nanoparticles and Their Applications as Thermal-Responsive Polymer Switching Composites for Battery Safety

Author

Li, Mingqian

Publication Date

2021

Peer reviewed|Thesis/dissertation

UNIVERSITY OF CALIFORNIA SAN DIEGO

Synthesis of Conductive Nanoparticles and Their Applications as Thermal-Responsive Polymer Switching Composites for Battery Safety

A dissertation submitted in partial satisfaction of the
requirements for the degree Doctor of Philosophy

in

Chemical Engineering

by

Mingqian Li

Committee in Charge:

Professor Zheng Chen, Chair
Professor Renkun Chen
Professor Ping Liu
Professor Tina Ng
Professor Andrea Tao

2021

The dissertation of Mingqian Li is approved, and it is acceptable in quality and form for publication on microfilm and electronically.

University of California San Diego

2021

DEDICATION

This dissertation is dedicated to my supervisors, friends, and parents.

TABLE OF CONTENTS

LIST OF FIGURES

LIST OF TABLES

ACKNOWLEDGEMENTS

In all, I would like to express my heartfelt thanks to my advisor, Professor Zheng Chen. I am grateful for his opportunity to allow me to do research and consistently supports. I am impressed with his passion and patience, guiding me through my projects and writings. In addition, I sincerely acknowledge the committee members: Professor Ping Liu, Professor Tina Ng, Professor Renkun Chen, and Professor Andrea Tao, for their valuable time, encouragement, and suggestions.

Secondly, I would like to thank my collaborators: Dr. Haodong Liu, Qizhang Yan, Dawei zhang, Xingyu Guo for their valuable suggestions and work. In addition, I would like to thank my labmates, Hongpeng Gao, John Holoubek, Dr.Guorui Cai, Dawei Xia for the good time with them during the PhD study. Also, I'm grateful for all the help from Ms. Dana Jimenez.

Finally, I would like show my gratitude to my parents, who support me to finish my PhD and always encourage me to overcome difficulties.

Chapter 2, in full, is a reprint of the material "Bio-Inspired Nanospiky Metal Particles Enable Thin, Flexible, and Thermo-Responsive Polymer Nanocomposites for Thermal Regulation" as it appears in Advanced Functional Materials, Mingqian Li, Yang Shi, Hongpeng Gao, Zheng Chen, 2020, 30, 1910328. The dissertation author was the first author of this paper and conducted all the essential research work.

Chapter 3, in full, is a reprint of the material "Scalable Solvent-Based Fabrication of Thermo-Responsive Polymer Nanocomposites for Battery Safety Regulation" as it is in preparation, Mingqian Li, Panpan Xu, Suk-woo Lee, Bum-young Jung, Zheng Chen The dissertation author was the first author of this paper and conducted all the essential research work.

Chapter 4, in full, is a reprint of the material "Synthesis of Appearance Controllable Carbides as Conductive Fillers of Thermo-Responsive Polymer Nanocomposites for Battery Safety" as it is in preparation, Mingqian Li, Hongpeng Gao, Zheng Chen. The dissertation author was the first author of this paper and conducted all the essential research work.

I would like to acknowledge the financial support from the LG chemistry and Jacob School of Engineering at UC San Diego.

VITA

2016	B.S., Chemical Engineering, Hefei University of Technology
2021	Ph.D., Chemical Engineering, University of California San Diego, La Jolla, CA

PUBLICATIONS

1. Shi, Y., Tang, H.M, Jiang, S.L., Kayser L.V., **Li,M.Q.**, Liu, F., Ji,F., Lipomi, D. J., Ong, S. P., Chen, Z. 2018. Understanding the Electrochemical Properties of Naphthalene Diimide: Implication for Stable and High-Rate Lithium-Ion Battery Electrodes. Chemistry of Materials, 10, pp. 3508–3517.

2. Ji,F., Shi, Y., **Li,M.Q.**, Jiang, S.L., Chen, G., Liu, F., Chen.Z. 2018. Scalable synthesis of uniform nanosized microporous carbon particles from rigid polymers for rapid ion and molecule adsorption. ACS applied materials & interfaces, 10, 30, 25429–25437

3. Ji,F., Wang, L., Yang, J., Wu, X., **Li,M.Q.**, Jiang, S.L., Lin, S.H., Chen, Z. 2019. Highly compact, free-standing porous electrodes from polymer-derived nanoporous carbons for efficient electrochemical capacitive deionization, Journal of Materials Chemistry A, 7, 1768-1778.

4. Shi, Y., Tan, D.H.S., **Li,M.Q**., Chen.Z. 2019. Nanohybrid electrolytes for high-energy lithium-ion batteries: recent advances and future challenges, Nanotechnology, 30, 302002.

5. Wang, D.D., Liu, H.D., **Li,M.Q**., Wang, X.F., Bai, S., Shi, Y., Tian, J.H., Shan, Z.Q., Meng, Y.S., Liu, P., Chen.Z. 2019. Nanosheet-assembled hierarchical Li4Ti5O12 microspheres for high-volumetric-density and high-rate Li-ion battery anode, Energy Storage Materials, 21, 361-371.

6. Holoubek, J., Yin, Y.J., **Li,M.Q**., Yu, M.Y., Meng, Y.S., Liu, P., Chen.Z. 2019. Exploiting Mechanistic Solvation Kinetics for Dual-Graphite Batteries with High Power Output at Extremely Low Temperature, Angewandte Chemie International Edition, 18892-18897.

7. Cai, G.R., Holoubek, J., Xia, D.W., **Li,M.Q**., Yin, Y.J., Xing, X., Liu, P., Chen.Z. 2020. An ester electrolyte for lithium–sulfur batteries capable of ultra-low temperature cycling, Chemical Communications, 56, 9114-9117

8. Holoubek, J., Yu, M.Y., Yu, S.C., **Li,M.Q**., Wu, Z.H., Xia, D.W., Bhaladhare, P., Gonzalez, S.M., Pascal, T.A., Liu, P., Chen.Z. 2020. An All-Fluorinated Ester Electrolyte for Stable High-Voltage Li Metal Batteries Capable of Ultra-Low-Temperature Operation, ACS Energy Letters, 5, 5, 1438–1447.

9. **Li,M.Q**., Shi, Y., Gao, H.P., Chen.Z. 2020. Bio-Inspired Nanospiky Metal Particles Enable Thin, Flexible, and Thermo-Responsive Polymer Nanocomposites for Thermal Regulation, Advanced Functional Materials, 30, 23, 1910328.

10. Wang, D.D., Liu, H.D., **Li,M.Q**., Xia, D.W., Holoubek, J., Deng, Z., Yu, M.Y., Tian, J.H., Shan, Z.Q., Ong, S.P., Liu, P., Chen.Z. 2020. A long-lasting dual-function electrolyte additive for stable lithium metal batteries, Nano Energy, 75, 104889.

11. Gao, H.P., Yan, Q.Z., Xu, P.P., Liu,H.D., **Li,M.Q**., Liu, P., Luo, J., Chen.Z. 2020. Efficient Direct Recycling of Degraded LiMn2O4 Cathodes by One-Step Hydrothermal Relithiation, ACS Applied Materials & Interfaces, 12, 46, 51546–51554.

12. Xu, P.P., Dai, Q., Gao, H.P., Liu, H.D., Zhang, M.H., **Li,M.Q**., Chen, Y., An, K., Meng, Y.S., Liu, P., Li, Y.R., Spangenberger, J.S., Gaines, L., Lu, J., Chen, Z. 2020. Efficient Direct Recycling of Lithium-Ion Battery Cathodes by Targeted Healing, Joule, 4, 12, 2609-2626.

13. Zhang, Y., Zhang, R., Chen, S.C., Gao, H.P., **Li,M.Q**., Song, X.L., Xin, H.L., Chen, Z. 2020, Diatomite-Derived Hierarchical Porous Crystalline-AmorphousNetwork for High-Performance and Sustainable Si Anodes, Advanced Functional Materials, 30, 50, 2005956.

14. Wang, D.D., Yan, Q.Z., **Li,M.Q**., Gao, H.P., Tian, J.H., Shan, Z.Q., Wang, N., Luo, J., Zhou, M., Chen, Z. 2021. Boosting the cycling stability of Ni-rich layered oxide cathode by dry coating of ultrastable Li3V2(PO4)3 nanoparticles, Nanoscale, 13, 2811-2819.

15. Xu, P.P., Yang, Z.Z., Yu, X.L., Holoubek, J., Gao, H.P., **Li,M.Q**., Cai, G.R., Bloom, I., Liu,H.D., Chen, Y., An, K., Pupek, K. Z., Liu, P., Chen.Z. 2021. Design and Optimization of the Direct Recycling of Spent Li-Ion Battery Cathode Materials, ACS Sustainable Chemistry & Engineering, 9, 12, 4543-4553.

16. Cho, Y.G. †, **Li,M.Q**. †, Holoubek, J. †, Li, W.K., Yin, Y.J., Meng, Y.S., Chen, Z. 2021. Enabling the Low-Temperature Cycling of NMC||Graphite Pouch Cells with an Ester-Based Electrolyte, ACS Energy Letters, 6, 5, 2016-2023.

17. **Li,M.Q**., Xu, P.P., Lee, S.W., Jung, B.Y, Chen, Z. 2021. Scalable Solvent-Based Fabrication of Thermo-Responsive Polymer Nanocomposites for Battery Safety Regulation, Submitted.

18. **Li,M.Q**., Chen, Z. 2021. Thermo-responsive Polymers for Thermal Regulation in Electrochemical Energy Devices, Submitted.

19. **Li,M.Q**., Gao, H.P., Chen, Z. 2021. Synthesis of Appearance Controllable Carbides as Conductive Fillers of Thermo‐Responsive Polymer Nanocomposites for Battery Safety, In preparation.

ABSTRACT OF THE DISSERTATION

Synthesis of Conductive Nanoparticles and Their Applications as Thermal-Responsive Polymer Switching Composites for Battery Safety

by

Mingqian Li

Doctor of Philosophy in Chemical Engineering

University of California San Diego, 2021

Professor Zheng Chen, Chair

Great advances have been made in lithium-ion batteries (LIBs) since they were first invented in 1970s. High energy density, fast charging rate and wide temperature operation have been achieved, which paves their way to broad applications in portable electronic devices, electric vehicles (EVs) and grid energy storage. However, despite their rapid performance improvement in recent years, safety issue is still the sword of Damocles of LIBs due to their inherent flammability and thermodynamically non-equilibrium operation, which can lead to catastrophic consequences once they are exposed to extreme conditions such as overheating, shorting or cracking.

In this thesis, strategies to foreclose potential safety hazards in LIBs have been explored in the level of material design. By integrating thermo-responsive polymer switching composites (TRPS) into the LIBs, it can successfully inhibit the heat generation when cells suffer from thermal abuses, which can prevent the occurrence of thermal runaway. To make TRPS materials more attractive in practical applications, we synthesized nanospiky Ni as the conductive fillers for the TRPS materials, which not only successfully reduce the thickness and improve the energy density of cell equipped with TRPS, but also boost the electrical conductivity of TRPS. To make TRPS materials can be seamlessly transferred to the industrial scale, we developed a solvent-based fabrication method to prepare PE-based TRPS materials on current collectors which can be directly integrated into the electrode production process. We revealed that the size distribution range of conductive fillers plays a critical role for the temperature response capability. The processing parameters such as substrate temperature, drying out time can affect the distribution of fillers in the polymer matrix, which determines the properties of TRPS

films. We obtained TRPS films in a large size with uniform quality and demonstrated the protective effect in pouch cells. We also designed a general synthetic method to obtain carbides with a desired morphology. Systematic investigations were conducted by characterizations and calculations to understand the phase and morphology evolution process of as-prepared tungsten carbide. Spherical tungsten carbide was synthesized and employed as fillers for TRPS, which boosts the conductivity of WC-based TRPS materials.

Overall, this dissertation offers a deep understanding and guidance for designing and fabrication of TRPS materials, taking one step further for the industrial production and real applications of TRPS to provide more safety protection of LIBs.

Chapter 1. Introduction

1.1. Background

The prosperity of the global economy in recent decades cannot shadow the energy crisis brought by the increasingly depleted natural resource and environmental pollution incurred by rapid industrialization. The energy demand was projected to increase 6 % between 2020 to 2030 through the United States, while the majority still contributed by fossil fuels, which is more than 76%. [1] At the same time, the CO_2 emissions is projected to grow around 0.6% per year until 2050,[1] further aggravating global warming. An alternative energy source is desperately needed to alleviate the energy crisis and inhibit environmental pollution.

Renewable energy is a rising focus for the post-oil era. Abundant sources such as solar, wind, hydro and geothermal energy can provide sustainable supports for the different geographical environment. Carbon neutral features guarantee no CO_2 emissions and environmental pollutions. To widely promote and use renewable energy, various energy forms are converted into electricity for the convenience of storage, so electrochemical energy storage devices are indispensable. Lithium-ion batteries (LIBs) are one of the most promising solutions due to their high energy density, high power, low maintenance, low-cost and long calendar life. They play critical roles from grid energy storage to each customer terminal, such as smart phones and electrical vehicles (EVs). The market share of EVs is projected to increase from 2.7% to 58% from 2020 to 2040, which is about 54 million EVs.[2] They are the game-changer on the table determining the battle of mainstream energy sources.

In short, LIBs are boosters of the popularization of renewable energy. The development of LIBs with superior performance and more reliable safety should be the focus and the top priority for the battery society.

1.2. LIBs: Components and work mechanisms

LIBs was first invented at 1970s, which gained tremendous attentions from the community. Sony Co. commercialized the first LIBs. Since then, great advances have been made in lithium-ion batteries (LIBs). Batteries are made of four components: anode, cathode, separator and electrolyte. The cathode and anode act as the host for the lithium, and the electrolytes can connect cathode and anode ionically by allowing lithium ions shuttle through the separator back and forth. Higher energy density, faster charge rate and wider temperature operations have been achieved, which paves their way to broad applications. New chemistries of cathode were investigated consistently from Lithium manganese oxide (LMO), Lithium iron phosphate (LFP) to Nickel Cobalt Manganese Oxide (NCM) to pushing the capacity limit while manage to maintain good capacity retention and electrochemical stability. The anode design enables larger capacities with higher rate performance by switching from intercalation to conversion or alloy chemistry such as Si materials. Electrolyte engineering can extent the application scenarios to ultra-low temperature by tuning the solid-electrodes interphase (SEI) and cathode electrolyte interphase (CEI) composition as well as the Lithium-ion/solvent structure.

However, the popularization of lithium-ion batteries (LIBs) will be impeded until their safety issues are settled. When they exposed to hazardous scenarios such as overheating, shorting and cracking, the source of clean energy could be a fatal bomb

instantly. Such uncertainties stem from their inherent flammability of the non-aqueous electrolytes and thermodynamically non-equilibrium operation conditions.

To address the safety issue, various strategies have been developed to foreclose potential safety hazards in LIBs. In the aspect of system design, with the help of big data and machine learning,[3] battery management systems (BMSs) are developed to monitor and control critical information such as voltage, current and temperature to predict, react and prevent latent dangers.[4] In the aspect of structural engineering, with the help of advanced modules arrangement [5]and cooling system, battery packs can suffer from more violent mechanical and thermal abuses. In the aspect of material design, Functional separators,[6] electrolyte additives,[7] non-flammable electrolytes[8, 9] and all-solid-state electrolytes (ASSEs)[10] have been explored to improve intrinsic cell safety. They are often realized by compensation performance and additional cost for devices components and fabrications.

1.3. Challenges in Opportunities

Despite great efforts have been put in solving the safety issues of LIBs, it is still a long way to eliminate the potential safety hazards and gain trust from the public again. Thermo-responsive polymer switching materials (TRPS), which was introduced by Chen *et al*. [11] into the interior structure of LIBs as an extra thermo-responsive switching (TRPS) layer between current collectors (i.e. Al/Cu) and electrode materials, are capable to effectively protect batteries from thermal abuses.

Essentially, conductive fillers (i.e. Carbon black, CNT, Ni) and a polymer matrix (Polyvinylidene fluoride (PVDF), Polyethylene (PE)) are indispensable for TRPS

materials. The working mechanism is that, at room temperature (R.T.), electrons can transport through the conductive pathway formed by conductive fillers unconstrainedly; while the volume expansion of the thermo-responsive polymer under the elevated temperature will lead to a disconnection between fillers and restrict the transfer of electrons. The internal resistance increases and suppresses the heat generation from Joule heating and therefore prevent the occurrence of thermal runaway. Such an intrinsic response to thermal abuses can provide the most rapid and accurate protections for each single LIB, which may offer a new pathway to the solution for the safety hazard.

1.4. Motivation and Outline of the Thesis

As discussed above, TRPS-embedded LIBs can provide intrinsic protection against dangerous circumstances. The ultimate goals of this thesis are: 1) to further push the limit of TRPS, approaching the ideal TRPS materials which have a high electrical conductivity, fast response to abuses, large PTC intensity (the logarithm of the ratio of the maximum resistivity to the resistivity at room temperature), reversible switching capability and an ultra-thin thickness. 2) to develop a fabrication method which can be easily scaled up and seamlessly integrated into state-of-art electrodes production process.

Chapter 2 discusses the strategy to boost the performance of TRPS by the application of the as-synthesized nano-spiky Ni particles, which greatly increases the conductivity and reduces the thickness of TRPS. **Chapter 3** shows a new production procedure which can be directly incorporated into industrial mass production to obtain high-quality PE-based TRPS films. The demonstration of TRPS in pouch cells was exhibited for the first time. Possible electrical abuse protection is also displayed. **Chapter**

4 describes a universal method to synthesize morphology-controllable carbides for the applications in TRPS for battery safety.

Chapter 2. Ni-based TRPS materials

Positive temperature coefficient (PTC) materials can rapidly increase their resistance as the temperature rises to a certain point (the "switching temperature", or Ts) to shut down their current flow. However, most of the previous PTC materials have relatively low room temperature (R.T.) conductivity (σ <1 S cm^{-1}) and/or small PTC intensity (2 to 3),[12-14] which still limits their effectiveness in current regulation for LIBs. Ni as one of the most common metal, has a good electrical conductivity (1.43 $\times 10^5$ S cm^{-1}) and can be synthesized through diverse methods with different size and shape, which makes it as an ideal candidate as conductive fillers for TRPS materials.

2.1. Introduction

2.1.1. Literature review of safety issues of LIBs

A lot of efforts have been dedicated to designing novel materials and structures to improve the LIB safety properties. Focus has been put on developing internal safety strategies because they have the potential to more effectively prevent thermal runaway than external components due to their direct response to local safety events.[15] Various functional separators[16,17,14,18,19] and electrolyte additives,[20,21,22,23] have been designed to improve thermal stability or to shut down batteries at elevated temperatures. However, the irreversible shutdown based on relatively slow polymer melting and/or chemical reaction mechanisms limit their effectiveness. Strategies can rapidly prevent or control the heat generation and temperature increase inside batteries remains needed.[24]

2.1.2. Inspirations and strategies

To achieve high conductivity and large PTC intensity, conductive fillers with suitable size and shape should be selected. To realize rapid switching rate and tunable switching range, the ratio between polymer matrix and filler-to-matrix needs to optimized. And for good reversibility, it requires uniform size distribution of conductive fillers in the polymer matrix.[11, 25, 26] We previously reported a class of PTC-based thermo-responsive polymer composites made from 3 to 5 μm size metallic nickel (Ni) particles with nanoscale surface protrusions and polyethylene (PE) as the polymer matrix. These materials showed rapid response to temperature increase and repeatable shut-down capability of LIB under overheating conditions,[11] suggesting the beneficial role of surface structures in enhancing electrical properties. However, since the size of the conductive fillers are large, the thickness of the composite film has been limited to ~20 μm to form an effective particle network. Because the energy density of LIBs is very sensitive to their volume and weight, adding such an electrochemical inert film into each individual cell inevitably has negative impact on its volumetric and mass energy density. In addition, the large filler size and large surface protrusions (200-300 nm) also limits the composite conductivity, requiring particle loading to be as high as ~20 vol% (volume fraction) to achieve sufficient R.T. conductivity (*e.g.*, ~10 S cm^{-1}). Therefore, significant advancements in increasing composite conductivity and reducing film thickness has to be made before such composite can be used for practical cells.

Inspired by uniform hierarchical structures created by nature, such as sweetgum fruit and jimson weeds, here we developed a new class of PTC-based thermo-responsive polymer switching (TRPS) materials based on uniform nanospiky Ni particles (~500 nm)

as the conductive filler to achieve high R.T. conductivity with small film thicknesses. Compared with micron-size Ni particles, the uniform and small nanospiky Ni particles can significantly increase the network conductivity by shorten the average distance between fillers, reducing the thickness of TRPS films while maintain the conductive network to provide sufficient electrical conductivity, as well as increase the energy density of LIBs.

Table 2.1 Data summary of PTC composites properties in literature

Composites	Conductive filler ratio (wt%)	Resistivity change rate (Ω cm^{-1} °C^{-1})	R.T. Conductivity (S cm^{-1})	PTC intensity (log ($R_{max}/R_{R.T.}$))	ref
Nanospiky Ni /PVDF	40	2×10^5	108	8.04	This work
Carbon black /Nylon 11	40	2.55×10^5	0.0009	3.85	[27]
Carbon black /Acetal Resin	40	1.1×10^4	0.16	4.49	[27]
Carbon black /PVDF	50	17	5	3.41	[27]
Carbon black/Poly(methyl methacrylate)	10	7.23×10^3	0.0003	2	[28]
Polyethylene oxide/ethylene vinyl acetate/acetylene black	24	1.59×10^4	0.0012	2.33	[25]
P-doped P3OT	100	6.36×10^3	0.005	2.98	[29]

2.2. Synthesis of Ni for high conductive TRPS materials

2.2.1. Experimental

2.2.1.1. Synthesis of nanospiky Ni particles

Spiky Ni was synthesized by an aqueous solution method. Typically, 15 g of nickel acetate ($Ni(N_2H_4)_3](CH_3CO_2)_2$, Sigma Aldrich) was dissolved in 105 mL of DI water. 17.2 g of hydrazine hydrate ($N_2H_4 \cdot H_2O$, Sigma Aldrich) was added to the solution to obtain nickel hydrazine complexes at 50 ℃ and further heated to 65 ℃ for an hour. When the system cools down to 50 ℃, aqueous NaOH solution was added, followed by being heated to 70 ℃ for 3 hours. The as-synthesized particles were collected after aging for 24 hours, washed by DI water, ethanol and toluene and dried in a vacuum oven at 50 ℃ overnight.

As-synthesized Ni was reduced under forming gas (5% hydrogen + 95% N2) in a tube furnace (Thermo Scientific HTF55322A) with 5 ℃ min-1 ramping rate to a certain reduction temperature (range from 250 to 400 ℃) for 2 hours and natural cooling to room temperature.

2.2.1.2. Preparation of TRPS materials

Hot melting-cast method preparation of PE-based TRPS: PE-TRPS films were made by directly mixing PE (Sigma) and conductive fillers such as Ni (commercial spiky Ni, Novamet), or carbon-based conductive fillers such as Super P, Ketjen black, graphite flakes (US Research Nanomaterials), graphite particles (US Research Nanomaterials), carbon nanotubes and graphene (Cheaptubes) at different ratio on a glass heating by a hot

plate at 130 ℃ (above the melting point of PE) until the WC particles were well-mixed. Films were tear off after cooling down to room temperature.

Solvent-casting method preparation of PVDF-based TRPS: conductive fillers Ni (commercial spiky Ni, Novamet) were mixed with PVDF (Sigma) at different ratio in n-methyl-2-pyrrolidone (NMP) by a Thinky mixer (Model ARE-310) in a 12 ml container. The slurry was then coated on a glass substrate by a doctor. After drying in vacuum oven at 80 ºC for 4 hours, free-standing TRPS films can be obtained.

2.2.1.3. Preparation of TRPS materials

Conductivity measurement: The electrical conductivity at R. T. was measured by a four-point probe with a Keithley 2400. The sample were prepared into a size of 12.7 mm×5 mm stripe and the thickness was measured by a micrometer. To obtain accurate test results, each sample was measured for multiple times at different positions and the average value were calculated to represent the conductivity.

Intensity of Switching Response (PTC intensity) measurement: For PVDF-based TRPS films, the temperature-dependent resistance measurement of various composites were conducted with a two-probe method by increasing temperature at a rate of 10 ℃ min^{-1} in a muffle oven (type MTI KSL-1100X-S-UL-LD), and a multimeter (Etekcity MSR-R500) was connected to the samples to record the resistance change. While for the PE-based TRPS films, the test temperature range is R.T. to 100 ºC.

Switching reversibility measurement: To obtain the performance of switching performance under repetitive heating/cooling cycle, as-prepared TRPS films heated in a muffle oven (type MTI KSL-1100X-S-UL-LD) until switching under overheating, then

removed from the oven and cooled down to room temperature naturally until the conductivity resumed. Repeat this process consistently to get reversible switching performance a multimeter (Etekcity MSR-R500) was connected to the samples to record the resistance change.

Shuntdown repeatability measurement: A hot-air gun (YiHua SMD Reworks Station 852D+) was used for repeatable shutdown tests, with a temperature of 145 ℃ to heat TRPS films above its Ts in a short time to trigger the shutdown response. After the resistance resumed to normal at room temperature, repeat this process for 40 times. All samples were cut into strips (12.7 mm×5 mm), and the thickness was measured by a micrometer.

Shutdown tests for the LED circuit: A circuit with components of a Ni/PVDF film, leads, a LED light and a 2032 cell was constructed. The TRPS film were heated by a hot plate up to the Ts and the light intensity was checked to demonstrate the resistance switching capability of the TRPS film.

2.2.1.4. Preparation of TRPS materials

Cathode preparation: Cathode were made by mixing NCM111 (Toda), PVDF (HSP-1800) and Super P at a mass ratio of 8:1:1 in NMP solvent by a Thinky mixer (Model ARE-310) at 2000 rpm for 30 mins. The slurry was cast by an auto-coater (MSK-AFA-II-VC-FH) on an Al current collector or an Al-TRPS current collector and dried at a vacuum at 80 ℃ for 10 h. For coin cells, the electrodes were cut by a pouch cutter with a 12mm-diameter.

Battery fabrications: The control group of 2032 coin cells were fabricated with the as-prepared cathode, a lithium disc and separator (25 μm Celgard 2500). The electrolyte was 1 M $LiPF_6$ in ethylene carbonate/diethylcarbonate (1:1 v/v) (LP40). The experimental group of 2032 coin cells were prepared with a structure of Cathode cap ‖ TRPS film ‖ cathode ‖ separator ‖ Li disc ‖ spacer ‖ spring ‖ anode cap. The TRPS films were cut into a circular shape with a diameter of 19 mm ahead before putting into the cell.

2.2.1.5. Battery tests

Cycling Tests: Galvanostatic charge/discharge cycling was performed on Neware BTS-4000 for tracking cycling performance. The typical cycle condition for NCM half-cell is at the constant current 0.1 C (1C = 160 mA) for first 2 cycles from 3 to 4.3 V (vs Li/Li^+), then the rest is cycle at 1C. All cells cycled after resting for 12 hours.

Overheating Tests: The TRPS-based batteries were tested in a convection oven (MTI EQ-DHG-9015) held at 100 ºC to verify the thermal shutdown capability. Once the temperature reaches Ts, the batteries shut down immediately. After cooling down to room temperature, the batteries can resume their capacities without decay. The reversible shutdown property was tested in the same way by repeating above process during battery cycling. The voltage and temperature changes were recorded by the Neware.

2.2.1.6. Characterizations

The morphology of the purchased and as-synthesized Ni particles and the surface and cross section of TRPS films were examined with Scanning Electron Microscopy (SEM) using a FEI Quanta 250 SEM. X-ray diffraction (XRD) patterns were obtained by

an X-ray diffractometer equipped with a Cu Kα radiation source (λ=1.5146 Å) at 30 kV and 10 mA (Bruker D2 Phaser, Germany). X-ray photoelectron spectroscopy (XPS) (Kratos Analytical, Kratos AXIS Supra) was conducted with an Al anode source at 15 kV and all the peaks were fitted based on the reference C-C bond at 284.6 eV in CasaXPS. The spiky tips of Ni nanoparticles were examined by Transmission Electron Microscopy (TEM) (FEITitan 80–300 kV S/TEM).

2.2.1.7. Calculations of quantum tunneling effect

Quantum tunneling effects are extensively studied by Simmons in 1960s,[30] and the tunneling current is determined by the properties and thickness of the insulating layer and the voltage bias between the gap. By neglecting the varied height and thickness of potential barrier and assuming a rectangular one, the current density can be calculated by:

$$J = (6.2 \times 10^{10}/\Delta s^2)\left\{\varphi_I \exp\left(-1.025\Delta s \varphi_I^{\frac{1}{2}}\right)\right\} - (\varphi_I + V)\exp\left[-1.025\Delta s(\varphi_I + V)^{\frac{1}{2}}\right] \quad (1)$$

Where

$\varphi_I = \varphi_0 - \left(\frac{V}{2D}\right)(s_1 + s_2) - \left[\frac{5.75}{\epsilon_r(s_2 - s_1)}\right] In[s_2(D - s_1)/s_1(D - s_2)]$, $\Delta s = s_2 - s_1$, $s_1 = 6/\epsilon_r\varphi_0$ and $s_2 = D[1 - 46/(3\varphi_0\epsilon_r D + 20 - 2V\epsilon_r D)] + 6/\epsilon_r\varphi_0$ if $V < \varphi_0$, and $s_2 = (\varphi_0\epsilon_r D - 28)/\epsilon_r V$, if $V > \varphi_0$.The symbol φ_0 is the height of rectangular barrier and can be approximately taken as $\varphi_0 = W/e$, and ϵ_r is the dielectric constant of the insulator, which is for PE=2.3 here. When $V \sim 0$, the current formula can be simplified as:

$$J = (3.16 \times 10^{10}/\Delta s)\varphi_I{}^{1/2} V \exp\left(-1.025\Delta s \varphi_I{}^{\frac{1}{2}}\right) \quad (2)$$

Where

$$\varphi_I = \varphi_0 - \left[\frac{5.75}{\epsilon_r(s_2 - s_1)}\right] In[s_2(D - s_1)/s_1(D - s_2)] \ , \quad s_1 = 6/\epsilon_r\varphi_0 \ , \quad and\ s_2 = D - 6/\epsilon_r\varphi_0$$

, which shows a linear J-V characteristics.

2.2.2. Results and discussions

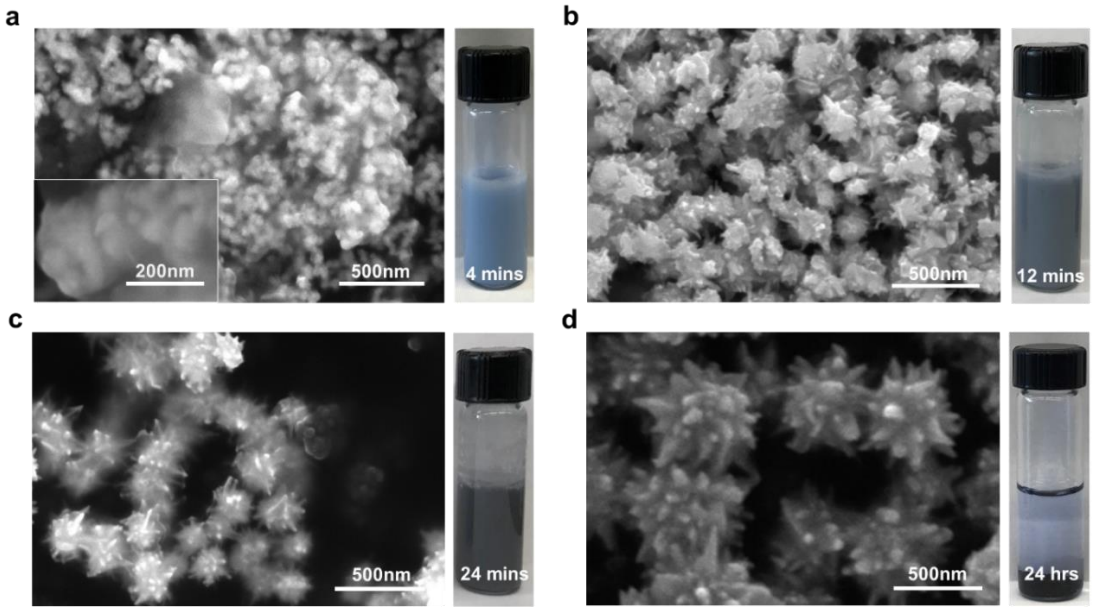

Figure 2.1 SEM images of reaction intermediates during the synthesis of uniform nanospiky Ni at different reaction time: (a) t = 4 mins, and the inset shows the aggregation of Ni spherical nanoparticles; (b) t = 10 mins; (c) t = 12 mins; (d) final product after aging for 24 hours. Insets show the solutions color at different reaction time when t = 4, 12, 24 mins, respectively. (f) Jimson weed with spiky structure.

Size-uniform nanospiky Ni particles were synthesized by aqueous reduction of nickel acetate tetrahydrate ($Ni(CH_3CO_2)_2{\cdot}4H_2O$) with hydrazine hydrate ($N_2H_4{\cdot}H_2O$) as the reducing agent under alkaline conditions (see experimental methods). To understand

the growth mechanism and control the growth of the sub-micron nanospiky Ni particles, reaction intermediates were collected at different reaction time and corresponding scanning electron microscope (SEM) images were shown in **Figure 2.1**. After 4 mins of reaction, the original pale-purple solution turned into cyan color, generated trace amounts of Ni nanoparticles (**Figure 2.1a**). These small Ni nanoparticles tended to fuse into larger size particles. It can be also found that these particles were covered by a thin film after drying, which might be $Ni(N_2H_4)_3$ complex[31] as the reaction intermediate. The size of these primary Ni particles is about 80-100 nm. After 12 mins, the reaction solution turned into dark grey following the formation of larger Ni agglomerates with an average size of 200-300 nm (**Figure 2.1b**). It can be also observed that surface nanospikes start to evolve with an irregular fashion. After 24 mins, the solution color changes to black, and the overall size of Ni nanoparticles further increased to 300-400 nm due to the continuous protrusion of the surface nanospikes (**Figure 2.1c**). The nanospiky Ni particles continued to grow during the aging process, leading to final product with the average size of 500-600 nm after aging (**Figure 2.1d**).

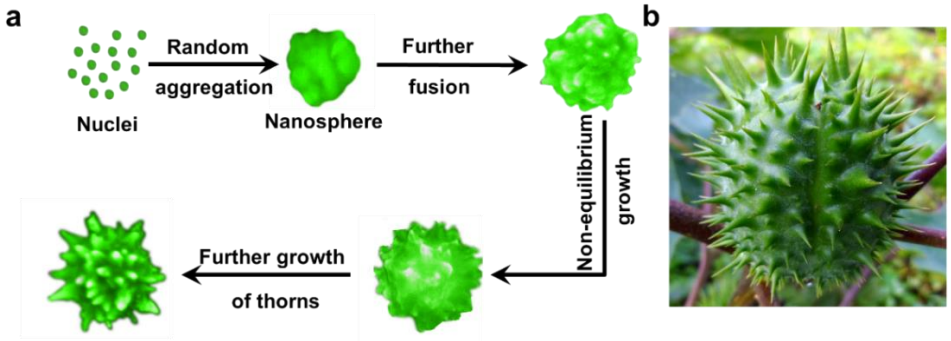

Figure 2.2 (a) Schematic illustration of the growth mechanism of the nanospiky Ni. (b) Jimson weed with spiky structure.

Based on the above observations, a magnetic assembly process[32] can possibly be adopted to describe the formation process of the spiky Ni nanostructure (**Figure 2.2a**). The Ni complex ($[Ni(Ni_2H_4)_3](CH_3CO_2)_2$) was first decomposed under basic condition and was converted into $Ni(OH)_2$, which can be further reduced by N_2H_4 to form Ni nuclei. Then Ni nuclei aggregated and grew into irregular polyhedrons, finally forming nanospiky Ni particles driven by the magnetic anisotropy energy, which exhibits a hierarchical morphology similar to sweetgum fruit and jimson weeds (**Figure 2.2b**).

The pH value influences the reduction pathways of Ni^{2+} by $N_2H_4 \cdot H_2O$. Reactions (1-2) and (3-4) indicate different redox pathways in acid and basic conditions as follows:

Acid environment:

$$N_2H_5^+ - 4e^- = 5H^+ + N_2 \qquad E^0 = -0.23\,V \quad vs\ SHE \qquad (1)$$

$$Ni^{2+} + 2e^- = Ni \qquad E^0 = -0.25\,V \quad vs\ SHE \qquad (2)$$

Alkaline environment:

$$Ni(OH)_2 + 2e^- = Ni + 2OH^- \qquad E^0 = -0.72\,V \quad vs\ SHE \qquad (3)$$

$$N_2H_4 + 4OH^- - 4e^- = N_2 + 4H_2O \qquad E^0 = -1.15\,V\ vs\ SHE \qquad (4)$$

The overall reactions involved in the growing process can be expressed as the following:

$$2[Ni(N_2H_4)_3]^{2+} + 4OH^- \rightarrow 2Ni \downarrow + N_2 \uparrow + 4H_2O + 5N_2H_4 \qquad (5)$$

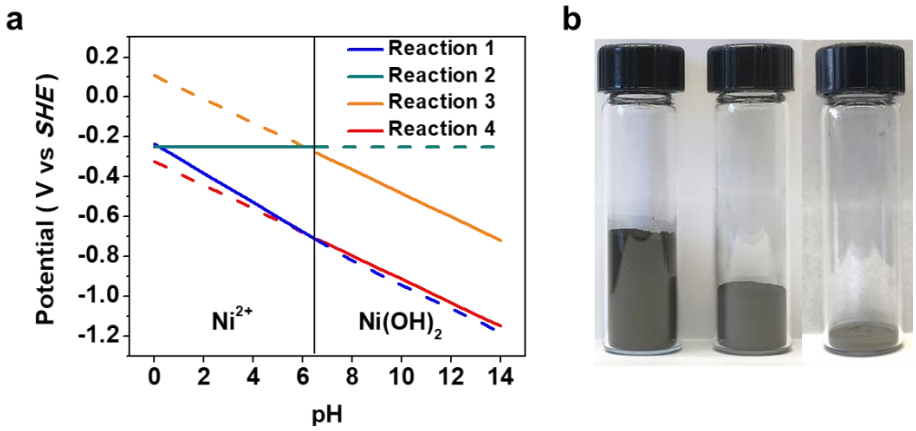

Figure 2.3 (a) Calculated reduction potentials dependence on pH value for different possible reaction pathways in acid (1, 2) and alkaline (3, 4) environment. Details of potential calculation are shown below. (b) 1 gram of as-synthesized nanospiky Ni (left) sample, commercial micron-spiky Ni (middle) sample (these samples are denoted as "HM-Ni" and "C-Ni", respectively, in the following sections) and commercial spherical Ni (right).

Based on Nernst equation $E = E_0 + \frac{RT}{nF} ln \frac{Red}{Ox}$, the reduced potentials vary with pH were calculated and shown in **Figure 2.3a**. Thermodynamically, Ni^{2+} or $Ni(OH)_2$ tends to be reduced to Ni even in acid conditions, while in fact it only can be reduced at base condition,[33] which is attributed to the exist of $[Ni(N_2H_4)_3](CH_3CO_2)_2$. Before adding KOH, there is no free Ni^{2+} ion in the solution, because most $[Ni(N_2H_4)_3]^{2+}$ complexes have very small solubility constant (K_{sp} for $[Ni(N_2H_4)_3](X^-)_2$, X = Cl^-, SO_4^{2-}, NO_3^- are in the range of 5×10^{-10} to 1.5×10^{-22}).[34] On the other hand, $Ni(OH)_2$ has a $K_{sp}=[Ni^{2+}]\cdot[OH^-]^2= 5.48\times10^{-16}$ in alkaline solutions,[35] so $[Ni(N_2H_4)_3](CH_3CO_2)_2$ prefers to decompose and convert into $Ni(OH)_2$ at elevated temperature, further reducing to Ni, which is consistent with previously research.[36] Due to the small size and nanospiky structures, the tap density of the synthesized Ni particles is only 0.58 g cm^{-3}, much lower than that of the 3-5 μm Ni (1.51 g cm^{-3}) and the spherical Ni particles (5.59 g cm^{-3}) (**Figure 2.3b**).

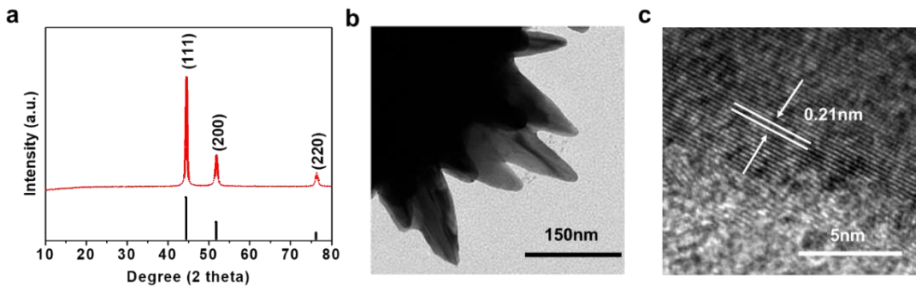

Figure 2.4 (a) The X-ray diffraction (XRD) pattern of as-synthesized nanospiky Ni and the metallic Ni standard. (b) TEM images of surface nanospikes (30-50 nm) of HM-Ni particles; (c) HRTEM image of one representative nanospike on the HM-Ni particle.

All the diffraction peaks in the XRD pattern (**Figure 2.4a**) match well with those of the PDF card (JCPDS card No.04-850, *Fm3m*), which confirms its face-centered cubic structure. Also, the (111)-to-(200) peak intensity ratio (2.95) is much higher than the normal value (2.32),[32] indicating the growth direction of the Ni particles is preferred to be <111>. No other impurity phases such as NiO can be identified within the XRD detection limit. High-resolution transmission electron microscopy (HRTEM) (**Figure 2.4b**) was implemented to further exam the growth direction. The lattice spacing of 0.21 nm corresponds to the crystal facet of the {111} cubic Ni, which further confirms that the growth of spikes was oriented along the <111> direction (**Figure 2.4c**).

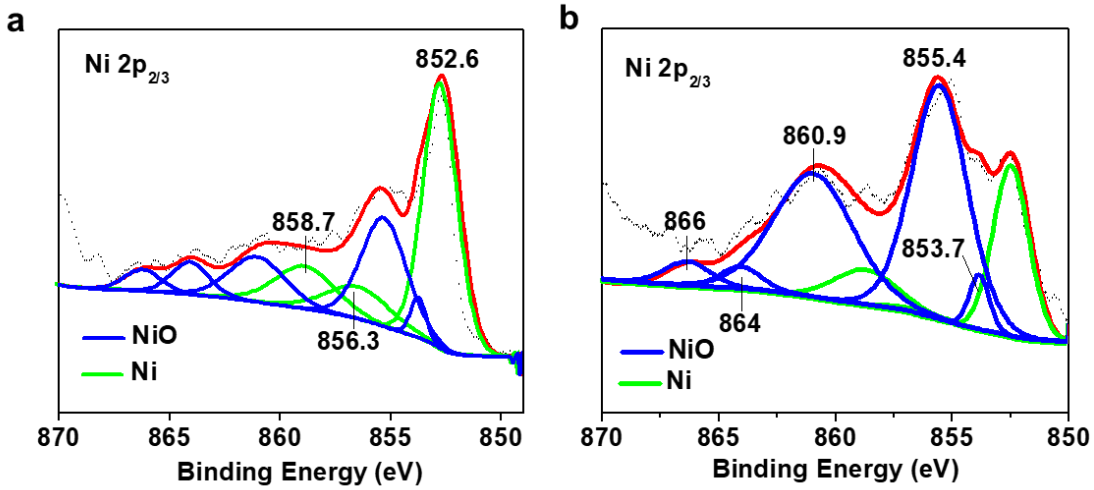

Figure 2.5. (a-b) XPS spectra of nanospiky Ni before and after thermal reduction at 350 ℃ for 2h in forming gas.

X-ray photoelectron spectroscopic (XPS) measurement was conducted to investigate the surface composition of the as-synthesized nanospiky Ni particles (**Figure 2.5a**). Peaks with binding energy of 853.7, 855.4, 860.9, 864 and 866 eV can be assigned to Ni^{2+}.[37] Quantitative analysis by integrating corresponding peaks areas suggests that ~75 % of Ni exists as NiO on the surface of the Ni particles. The fact that NiO was not detected by XRD suggests that the sample is metallic Ni in its bulk form while the strong XPS signal arising from NiO on the surface is attributed to the high surface activity of Ni nanoparticles which is commonly recognized.[38, 39]

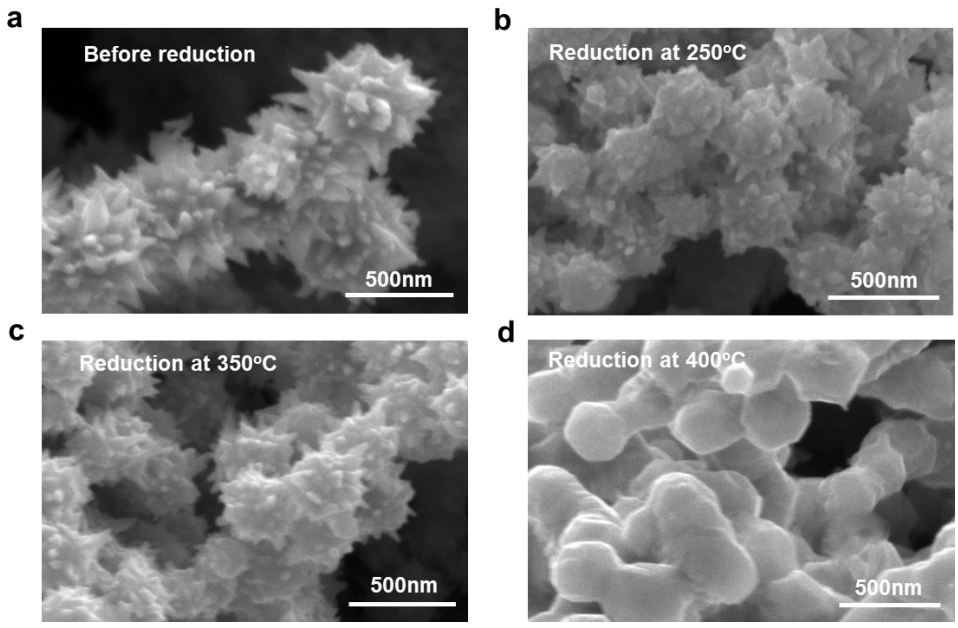

Figure 2.6. SEM images of spiky Ni morphology structure before (a) and after reduced at 250 ℃ (b), 350 ℃ (c),400 ℃ (d) (the samples are denoted as "R250", "R350" and "R400" based on their thermal reduction temperature).

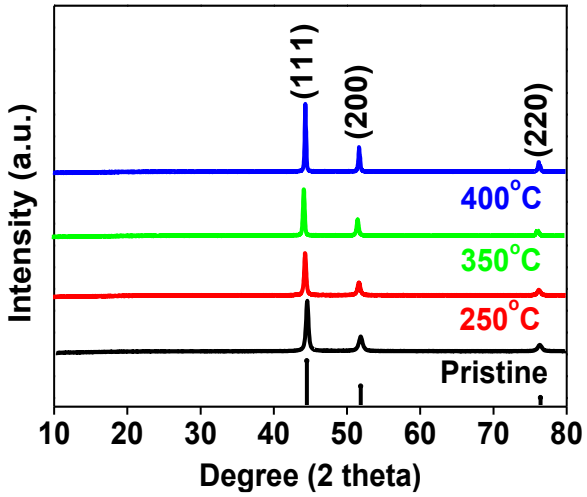

Figure 2.7 XRD patterns of as-synthesized spiky Ni before and after reduction treatment at temperatures in a range of 250 ℃ to 400 ℃ in forming gas.

Since the surface NiO layer is not conducting, to remove NiO the as-synthesized Ni particles were thermally reduced under forming gas (5% hydrogen + 95% N_2) at different temperatures. To achieve high Ni purity and void morphological change, the

crystal structure of Ni particle samples was carefully monitored during the reduction treatment. **Figure 2.6a-d** show the morphology evolution of spiky Ni particles with the increase of the thermal reduction temperature. Up to 350 ℃, the nanospiky morphology had little change during reduction annealing. When the temperature was further increased to 400 ℃, the spiky tips disappeared, indicating a thermal stability window below this temperature.[40] The size of Ni nanoparticles was also reduced to 350-400 nm after reduction treatment, coalescing to form larger clumps structure. Compared with pristine particles, all the peak positions remain no change while their intensity increased as increasing the annealing temperature, suggesting increased crystallinity of nanostructured Ni particles (**Figure 2.7**). XPS was also conducted to exam the change of their surface composition after reduction (**Figure 2.5b**). After reduction treatment the peak intensities of Ni^{2+} were much lower than the pristine samples (**Figure 2.5a**). Note that it is inevitable to see considerable amount of Ni^{2+} (43%) on the particle surface layer due to the high reactivity of native Ni.

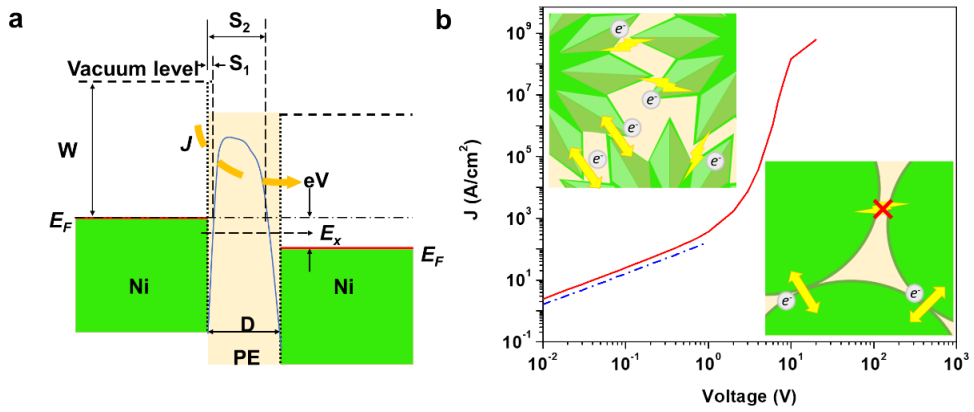

Figure 2.8 (a) A schematic of Ni-PE-Ni tunneling junction. Nickel has Fermi level EF and work function W. The PE thin film between the two Ni tip has a thickness D. V is the voltage bias. The width of the barrier for tunneling at the energy level Ex is S2-S1. (b) J-V characteristics of the Ni-PE-Ni junction. Current density as a function of voltage bias V, for two Ni tips (W= 5.15 eV[41]), separated by a PE gap (relative permittivity $\epsilon_r = 2.3$)[42] of width D = 1 nm, at T = 0 K. The blue dash-dot line is when V~0. The insets illustrate electrons transfer through conductive fillers network of nanospiky Ni (top left) and spherical Ni (bottom right), respectively.

Constructing the nanospiky structure while reducing the surface NiO turns out to be significantly important for improving conductivity. The quantum tunneling effect is more prominent and has greater possibilities to occur with such a morphology at small size. The schematic in **Figure 2.8a** illustrates a tunneling junction of the Ni-PE-Ni system, which has an insulating layer of PE with thickness *D* between two Ni particle tips. The amounts of electrons traveling through the insulating layer, or the current density, can be estimated using a model developed by Simmons[30]. And from **Figure 2.8b**, the net current density is linearly increasing and then rising rapidly at high voltage bias, which indicates a larger voltage bias can trigger a distinct tunneling effect. And this is what brings by the unique nanospiky structure: electrons tend to accumulate on the tips and then increase the voltage bias so more electrons can pass through the barrier. Also, compared with a spherical shape (insets), the nanospiky morphology provides more direct contact and

possible tunneling sites, which together offer higher overall conductivity. The advantages of having small and uniform nanospiky structure were further demonstrated by the outstanding electrical properties of the polymer composites fabricated from such Ni particles.

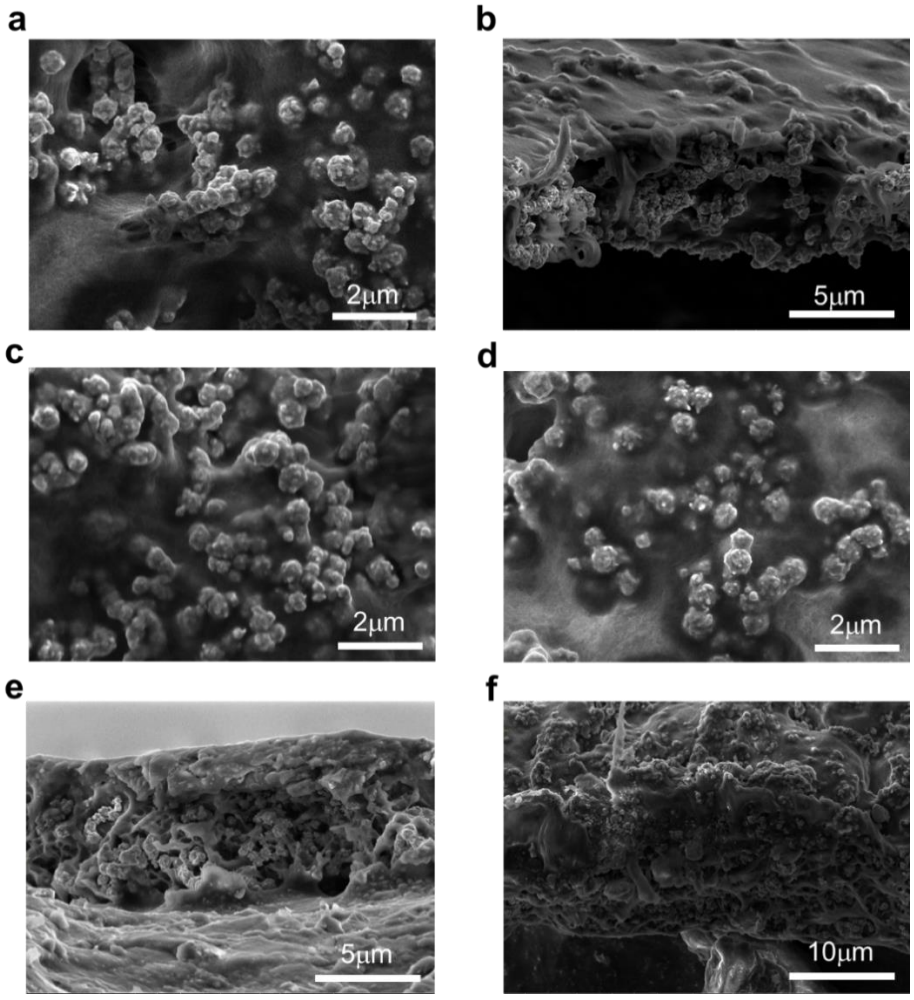

Figure 2.9. The top surface (a) and cross section (b) of a representaive Ni (9.1 vol%)/PVDF TRPS film with thickness of ~6 μm. The top surface (c) and cross section (d) of a representaive Ni (31.7 vol%)/PVDF TRPS film with thickness of ~7.8 μm. The top surface (e) and cross section (f) of a representaive Ni (31.7 vol%)/PVDF TRPS film

It is critical to first study how the thermal reduction temperature influences the conductivity of TRPS films made by these Ni particles. Films were fabricated by mixing

different Ni particles with PVDF by a solvent-casting process and the surface and cross-section view of the TRPS films with a thickness of ~6 μm were shown in **Figure 2.9a-b**. The film thickness can be easily adjusted by the slurry composition or the solvent-casting method (**Figure 2.9c-f)**. The TRPS film fabricated with pristine nanospiky Ni without reduction treatment had a R.T. conductivity of 60 S cm^{-1} at a filler volume fraction of 23.1vol%. By contrast, the conductivity of the TRPS film increased from 175 to 230 S cm^{-1} as the reduction temperature of Ni particles rose from 250 to 350 ℃. However, further increasing the reduction temperature led to a drastic drop of conductivity to 100 S cm^{-1} (**Figure 2.10a**). This trend can be explained by the composition and the morphology changes along the thermal reduction process. At relatively lower temperatures (< 350 ºC), although the thermal reduction might slightly change the spiky morphology (**Figure 2.6**), the conversion of NiO to metallic Ni significantly increased the bulk conductivity of the particles. The complete disappearance of surface nanospiky at high annealing temperature (>350 ºC) reduced the surface contact in the percolation network and eliminated quantum tunneling effect that are both critical for high conductivity.[11] In addition, high temperature reduction resulted in fusion of small Ni nanoparticles into a large lump, making it difficult to disperse them to form a uniform film. Therefore, in the following experiments, TRPS films were prepared with Ni reduced at 350 ℃ to obtain the maximum R.T. conductivity.

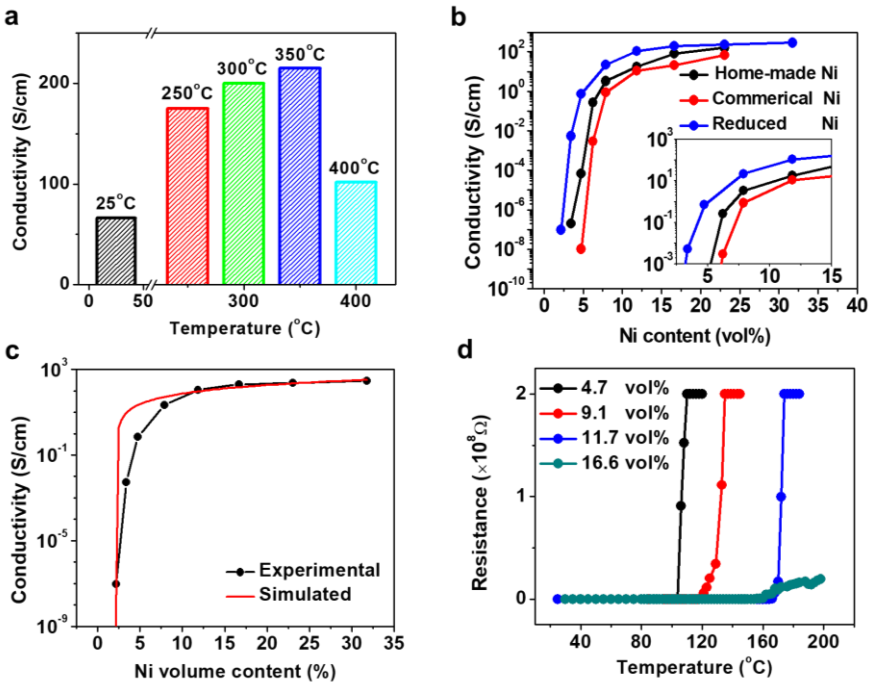

Figure 2.10 (a) Conductivity of Ni (23.1vol%)/PVDF TPRS films embedded with Ni treated at different temperatures. (b) Conductivity of Ni/PVDF films as a function of Ni volume fraction with different Ni conductive fillers (HM-Ni, C-Ni and reduced HM-Ni). (c) Experimental and simulated conductivity dependence on the volume farctio of Ni. (d) Resistance of different Ni/PVDF films as a function of increasing temperature.

The dependence of R.T. conductivity of TRPS films on the volume fraction of different Ni particles is shown in **Figure 2.10b**. Although all curves show similar trend, conductivity curves moved up for Ni with smaller sizes. Compared with the C-Ni and the as-synthesized Ni without thermal reduction, the R.T. conductivity of TRPS films with Ni reduced at 350 °C (R350) increased by 237% and 41%, respectively. The increase of R.T. conductivity is more significant at low Ni volume fraction (< 5 vol%). Specifically, the R.T. conductivity of R350 was about 10^7 times larger than that of C-Ni. Comparing with the state-of-the-art conductive composites that carbon-based PTC materials has R.T. conductivity in the range of 0.001 to 30 S cm^{-1},[43,27,44] and silver-based PTC materials shows a R.T. conductivity of < 30 S cm^{-1},[45] our TRPS films achieved the highest

conductivity of about 300 S cm^{-1} (~32 vol%). The simulated conductivity curved was also obtained by the following equation for further verification:

$$\sigma = \sigma_0(\varphi - \varphi_c)^t \quad (6)$$

where σ_0 is a constant of proportionality, φ is the volume fraction of the conductive fillers in the composites and φ_c is the percolation threshold. t is the critical exponent. For common 2D materials, the t is around 1.3.[46] in our case, t = 1.1, which indicates our system is close to 1D system. The experimental results well matched with the percolation theory (**Figure 2.10c**), with a percolation threshold at ~0.015 for R350 Ni, smaller than C-Ni (~0.02). Since the average interparticle distance in a composite matrix is proportional to the filler particle size, the decrease in particle size can enhance tunneling effect and lower the percolation threshold,[47] resulting in composites with high R.T. conductivity.

The TRPS films exhibited drastic and rapid change in conductivity once the temperature reached their thermal switching temperature (T_s). **Figure 2.10d** shows the dependence of the resistance of TRPS films on the temperature with different Ni (R350) contents. All samples displayed significant increase in resistance with rising temperature. For Ni/PVDF with 11.7 vol% of Ni, the change in resistance reached 8 orders of magnitude when temperature rises from 20 to 170 ℃, corresponding to a change rate of about 4×10^7 $℃^{-1}$ at T_s (168-174 ℃). Such a change in resistance is at least 10^4 times larger than other PTC composites.[27, 48] However, when Ni content was increased to 16.6 vol%, the resistance of TRPS film increases slowly, even when it was heated to 200 ℃, suggesting the formation of dense percolation that cannot be broken down by thermal expansion.

Tunable T_s within the range from 110 to 170 ℃ can be achieved by adjusting the Ni/PVDF volume ratio. As the Ni content increased from 4.7 to 11.7 vol%, the T_s approached to the melting temperature (T_m) of PVDF (~172 ℃). The change of T_s can be correlated to the average distance between Ni particles in the percolation network. According to Kono *et al.*,[49] at low Ni content (< 4.7 vol%), the nonlinear expansion of PVDF below the T_m is sufficient to break the conductive pathways, so high PTC intensity can be achieved at a T_s that is far below the T_m. As the Ni content increases (9.1 vol% and 11.7 vol%), the average gap distance between each filler particles decreases and higher temperature is required for the volume expansion. As Ni content reaches a specific value, volume expansion below the T_m cannot offer enough space to break the percolation network. Therefore, there was no obvious PTC effect (no T_s) when the Ni content reaches 16.6 vol%, even when the TRPS was heated to 200 ℃.

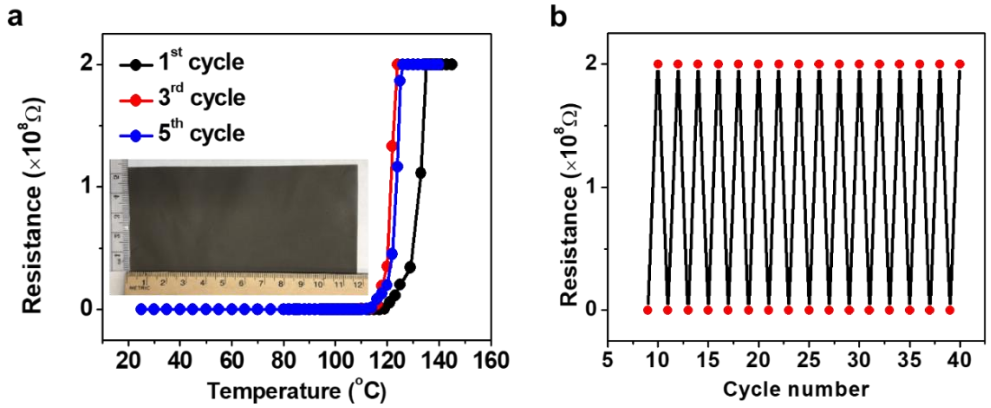

Figure 2.11 (a). Switching reversiblity of Ni/PVDF films at the 1st , 3rd and 5th cycle (with 9.1vol% of Ni). (b) Thermal cycle reversibility of a representative Ni /PVDF TRPS film (Ni loading fraction: 9.1 vol%).

Repeatable thermal switching cycles can be achieved in our TRPS films. **Figure 2.11a** shows the dependence of the film resistance on temperature for the Ni/PVDF

composites at the 1st, 3rd, and 5th heating cycles. There was no distinct change in the film conductivity below the T_s, while they exhibited a sudden leap up to 2×10^8 ohms above the T_s. After repeated thermal cycling, the T_s tended to slightly shift towards lower temperature, but the resistance at room temperature showed negligible change. Such a shift of T_s might be ascribed to the breaking and reconstruction of conductive network upon repeated switching cycling. The result for more thermal cycling test is shown in **Figure 2.11b**, which suggests highly repeatable conducting/insulting switching property. As the ratio of Ni in the composite increased to 11.7 vol%, a more stable T_s can be achieved during repeated thermal switching process, possibly due to the formation of more continuous Ni particle network.

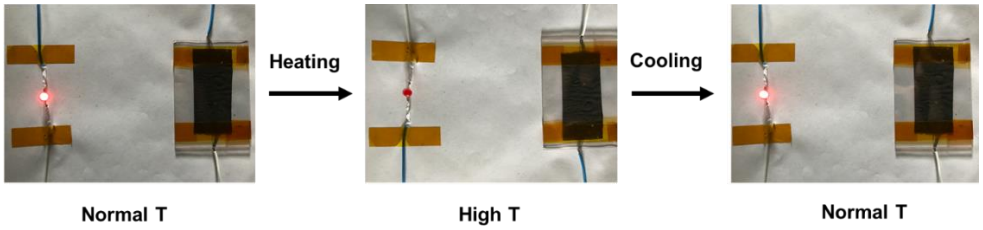

Figure 2.12 Demonstration of thermal swithcing behavior of Ni/PVDF films using hot plate. The tempeature of the hot plate under heating is 130 ºC.

In order to demonstrate the rapid and reversible thermal switching of the TRPS film for electrical circuit regulation, a simple circuit was designed (**Figure 2.12**) using a Ni/PVDF-based TRPS strip to connect a light-emitting diode (LED). The LED light can be immediately turned off after being heated up to its T_s on a hot plate. After cooling down, the LED lighted up again, indicating the reversible temperature-dependent resistance change of the TRPS film. The on-off switching can be repeated by many times without reducing the sensitivity. These properties suggest that the Ni/PVDF-based TRPS can be used to regulate the temperature of electric circuits for safety protection.

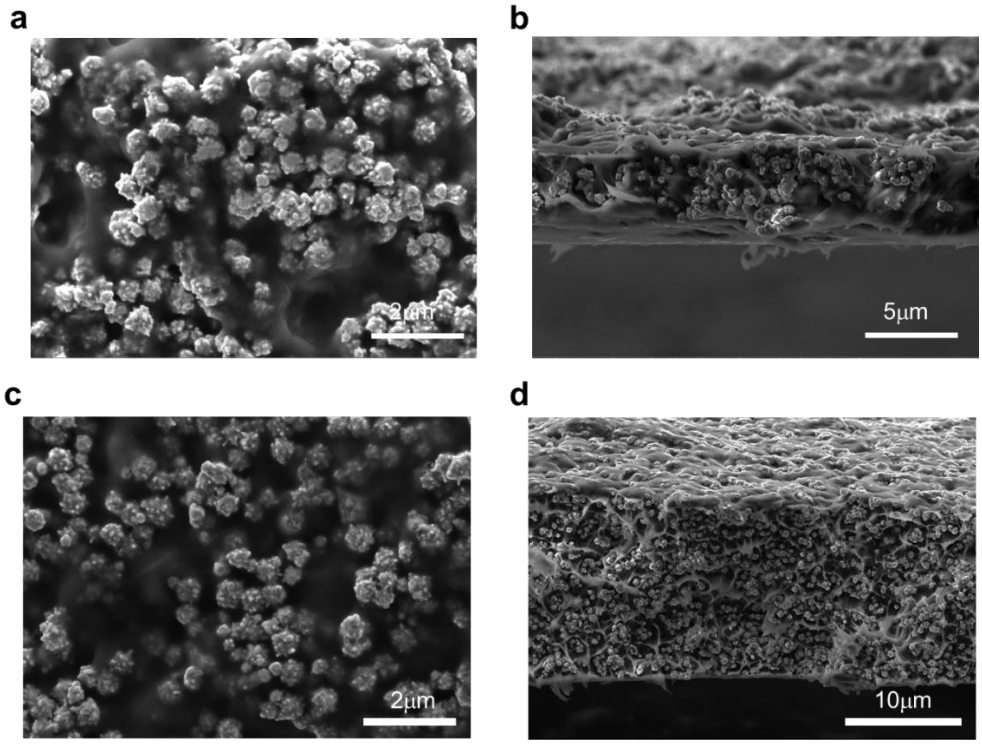

Figure 2.13. The surface (a) and cross-section (b) SEM images of a representaive Ni (30 vol%)/PE TRPS film with thickness of 5 μm. The surface (c) and cross-section (d) SEM images of a representaive Ni (30 vol%)/PE TRPS film with thickness of 14.8 μm.

Thermal switching function of TRPS in regulating LIB cells was further demonstrated. Since polar carbonate solvents are commonly used for LIB electrolyte, instead of using PVDF, here PE was used as the polymer matrix to fabricate Ni/PE-based TRPS due to its good chemical and electrochemical stability. Similar to the previous Ni/PVDF TRPS, the solvent-casting method was used to fabricate Ni/PE based TRPS films with a thickness as small as ~5 μm (**Figure 2.13a-b**). Different thicknesses can be also achieved by tuning the process parameters (**Figure 2.13c-d**). Considering a typical cylindrical cell (e.g., LG HB4) in **Figure 2.14a**, such an ultrathin TRPS film can increase the cell gravimetric and volumetric energy by 14.2 % and 9.1%, respectively, compared

with using 25 μm TRPS film the (**Figure 2.14c-d**). Such improvements are significant considering the limited weight and volume a cylindrical cell has.

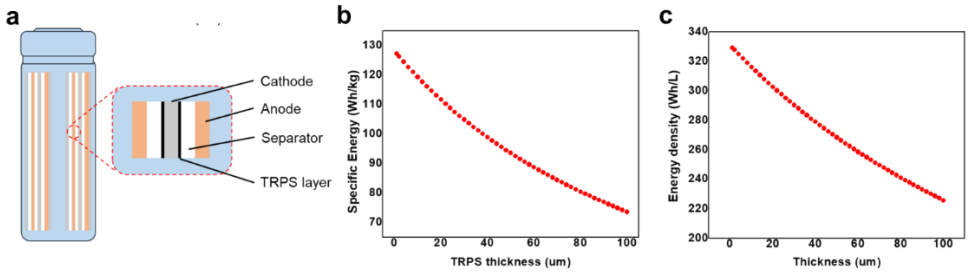

Figure 2.14. The effect of TRPS thickness on cell energy density. (a) gravimetric energy density and (b) volumetric energy density. (c) the cell structure used to calculate for energy density. (Parameters used in the energy density calculation are from Table.2.2)

Table 2.2 Detail parameters of the battery used for energy density calculation in Figure 2.14[50]

Manufacturer	Model	Capacity (Ah)	Weight (g)	Volume (cm^3)	Cathode (cm^2)
LG	HB4	1.535	43.1	16.7	778

An optimal ratio of Ni in the composites was also determined by mixing R350 with PE at different volume fractions and then identifying the dependence of the conductivity and Ni (**Figure 2.15a**). A R.T. conductivity of 100 S cm^{-1} was achieved at a Ni content of 15 vol% (10 times of that of C-Ni). Overall, the change of conductivity with the increase of Ni in the PE-based TRPS held the same trend as the Ni/PVDF system, showing higher R.T. conductivity than all the conductive PE composites reported so far. **Figure 2.15b** exhibits the dependence of T_s on the Ni content . Similar to the Ni/PVDF composites, the T_s shifted from 76 to 93 °C as Ni volume fraction increased from 5 to 15 vol%. The resistance of all samples ramps up above the testing limit (2×10^8 ohms) with rapid changing rate. Compared with Ni/PE TRPS composites fabricated by C-Ni with

large particle sizes, the T_s was higher when smaller size Ni was used in the same ratio,[11] which might be explained by the fact that closer interparticle distance requires more volume expansion to break the conductive pathways.[51] It is noted that even with a relatively high the Ni content (15 v%), the fabricated free-standing films TRPS films still maintain good flexibility (**Figure 2.15b**, **inset**).

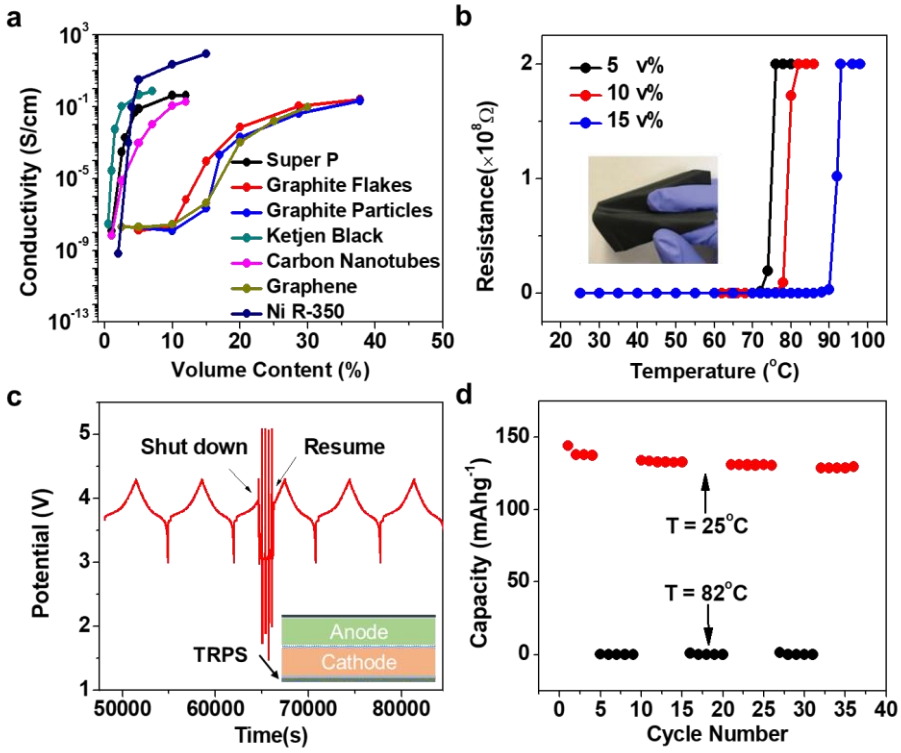

Figure 2.15 (a) Correlation between the conductivity and the volume ratio of different conductive fillers. (b) Resistance of different Ni/PE TRPS films as a function of temperature. The inset is a digital photo of a flexible Ni/PE TRPS film (5 cm x 8 cm). (c) Charge/discharge curve of a safety-improved NCM111 battery before and after thermal shut down at 82 °C. (d) Cycling stability of a safety-improved NCM111 battery between 25 and 82 °C.

Battery safety test using Ni/PE-based film was demonstrated by fabricating LIBs with oxide-based cathode ($LiMn_{1/3}Co_{1/3}Mn_{1/3}O_2$ or NCM111) and a TRPS-based thin film on its current collector (inset of **Figure 2.15c**). The LIBs were cycled at different

temperatures in a temperature chamber and their cell voltage was monitored (**Figure 2.15c)**. Initially, the LIB was cycled at R.T. condition and the battery showed normal charging/discharge behavior. It delivered a discharge capacity of 140 mAh g^{-1} in the voltage range of 3-4.3 V (*vs*. Li/Li^+), close to the theoretical reversible capacity of NMC111.[52] Once the chamber temperature increased to 82 ℃, the cell was shut down immediately due to drastically increased resistance, as indicated by the large and rapid change of cell voltage. The capacity dropped to zero when the environment temperature was above 82 ℃, indicating that the battery was completely shut down by the TRPS films. Then the battery cell can be resumed to normal cycling once it was cooled down to R.T. and the cell capacity was maintained at the same value. Such thermal shutdown can be also repeated by multiple times without appreciable change of its sensitivity (**Figure 2.15d**). The stable cycling of the TRPS-regulated LIB implies that the Ni/PE films are effective for repetitive thermal shutdown without noticeable performance decay. These properties suggest that the Ni/PE-based TRPS can be potentially used for thermal regulation of LIB for effective safety protection.

2.2.3. Conclusion

In summary, a class of novel thermo-responsive conducting polymer composites were developed using bio-inspired nanospiky Ni particles as the filler and different semi-crystalline polymers as the matrix. The unique nano-spiky Ni particles provided the composites with high room temperature conductivity, fast thermo-responsive and large PTC intensity, which were mainly due to their small particle size and abundant surface

nanospikes. In addition, the small size also allowed us to fabricate very thin (~5μm) polymer composites which were not achievable for micron-size particles. The thermo-responsive conducting polymer composites can be readily embedded into electric circuits and LIB batteries to reversibly shut down the device at high temperature and resume the function at normal conditions after cooling down, providing reliable safety regulation under thermal abuse. This work represents an important step towards the development of high-safety electronic devices without sacrificing their performance. The sub-micron nanospiky Ni particles and the derived conducting polymer composites can potentially have other applications such as thermoelectric devices and multifunctional sensors.

2.2.4. Acknowledgements

Chapter 2, in full, is a reprint of the material "Bio-Inspired Nanospiky Metal Particles Enable Thin, Flexible, and Thermo-Responsive Polymer Nanocomposites for Thermal Regulation" as it appears in Advanced Functional Materials, Mingqian Li, Yang Shi, Hongpeng Gao, Zheng Chen, 2020, 30, 1910328. The dissertation author was the first author of this paper and conducted all the essential research work.

Chapter 3. Scalable Solvent-Based Fabrication of TRPS

Embedding thermo-responsive polymer switching materials (TRPS) into LIB cells has been proved to be a promising strategy to provide consistent thermal abuse protections at coin-cell level. However, it is unrealistic to achieve large-scale applications without further demonstration in high-capacity pouch cells. Traditional fabrication methods of PE-based composites depend on extrusion, injection molding and rotational molding, [53,54] which requires bulky and expensive equipment. Besides, they are incompatible with the fabrication procedure of electrodes. A new fabrication method of TRPS films is in demand for its large-scale applications.

3.1. Introduction

3.1.1. Literature review

Strategies to foreclose potential safety hazards in commercialized LIBs have been explored in different ways. In the aspect of system-level development, combined with big data and machine learning,[3] battery management systems (BMSs) are designed to collect critical cell information such as voltage, current, resistance and temperature to predict and respond ahead of dangers.[4] In terms of structural engineering, new cell configurations,[55] pack and modules arrangement [5] have been explored to reinforce the strength of battery packs against mechanical abuses.[56] Air/liquid cooling systems are also introduced to alleviate heat accumulations. However, all the aforementioned technologies evade confronting with the intrinsic issues from the materials level. As a result of delayed response and feedback, these approaches cannot eliminate safety risks instantly.

3.1.2. Inspirations and strategies

Significant efforts have been also devoted to designing internal safety strategies at the materials level. Functional separators, [6, 57] electrolyte additives,[58] non-flammable electrolytes [5, 8] and all-solid-state electrolytes (ASSEs) [10] have been explored to improve intrinsic cell safety. They are often realized by performance compensation and additional cost for device components and fabrications. [59-61] Thermo-responsive polymer switching materials (TRPS), which are capable to effectively protect batteries from thermal abuses, [62] can achieve a good balance between safety, performance and costs. However, it cannot be widely applied unless a low-cost and scalable method is developed to obtain quality-consistent TRPS materials without interfering with the industry battery fabrication process.

In this work, we developed an efficient and scalable method to fabricate polyethylene (PE)-based ultra-thin, uniform, highly conductive TRPS for potential large-scale applications in LIBs. Using commercially available tungsten carbide (WC) nanopowder as the conductive filler, we elucidated that the embedded conductive network, which determines the performance of TRPS, largely depends on the size distribution of the conductive fillers and the fabrication process. Systematic studies on fillers and polymer selection, slurry preparation and film manufacturing were conducted to illustrate the correlation between fabrication process, filler distribution and TRPS properties. TRPS films were assembled under various conditions and inspected by surface and bulk characterization to exhibit filler distribution in the polymer matrix. Furthermore, electrical properties and thermal-responsive properties were measured. Successful assembly of

TRPS-integrated cathodes can protect pouch cells from thermal abuse conditions, which paves the way for scalable manufacturing and application of TRPS in LIBs.

3.2. Develop of scalable solvent-based fabrication method of TRPS

3.2.1. Experimental

3.2.1.1. Preparation of WC

The commercialized WC particles (C-WC) were obtained from Alfa Aesar. Before using. They were disperse in isopropyl alcohol by sonicating probe (Qsonica Sonicator Q700) with a intensity of 2 (14W) for 5 mins, then filtered through sieves with different size (500/1000/2000 mesh). Collected C-WC particles were dried in convection oven for 2 hours at 60 ^{o}C

3.2.1.2. Preparation of TRPS materials

Then as-pretreated WC were mixed with PE (Epolene® C-13 Polymer) at different ratio in xylene by a Thinky mixer (Model ARE-310) in a designed heat-insulating container. The slurry was then coated on a glass substrate or carbon-coated Al current collector (Al-TRPS) with vacuum drawing and by a doctor blade. The slurry was dried out immediately in R.T. The slurry was also tested with different soaking time to study the particle distribution and uniformity in the obtained TRPS film by using a culture dish to control the evaporation rate of xylene solvent from 0 to 60 mins in an oven at 80 ^{o}C.

3.2.1.3. Characterizations of TRPS properties

Conductivity measurement: The sample were cut into a circular shape with a diameter of 19 mm and the thickness was measured by a micrometer before testing. The surface electrical conductivity of both surface at R. T. was measured by a four-point probe with a Keithley 2400. To measure the vertical resistance, TRPS films were fabricated into a 2032 coin cell with a structure of spacer ‖ TRPS film ‖ spacer to provide constant contact areas and pressure. Then the resistance was measured at R.T. by a two-point probe method through a Keithley 2400. To obtain accurate test results, each sample was measured for multiple times at different positions and the average value were calculated to represent the conductivity.

Intensity of Switching Response (PTC intensity) measurement: The time-dependent resistance measurements of various composites was conducted with a four-probe method by putting samples into a convection oven at 100 ºC The resistance was recorded by a Keithley 2400. The time-dependent temperature measurements of TRPS was tracked by a K-type thermal couple on a temperature logger.

Rate of Switching Response measurement: A hot-air gun (YiHua SMD Reworks Station 852D+) was used for response rate testes by heating samples under different temperatures (150 ºC and 250 ºC) with different tests configurations for both coin-cell like and pouch-like structures. The resistance and temperature changes were recorded by the same way as switching resistance response tests.

Switching reversibility measurement: To obtain the performance of switching performance under repetitive heating/cooling cycle, as-prepared TRPS films were transferred into a 100 ºC convection oven until switching under overheating, then removed from the oven and cooled down to room temperature naturally until the conductivity resumed. Repeat this process consistently to get reversible switching performance. The resistance was recorded by a four-probe method through Keithley 2400.

Resistance stability measurement: TRPS films were transferred into a 100 ºC convection oven for 30 mins. A k-type temperature sensor was used to monitor the temperature variations. Resistance was recorded by a four-probe method through Keithley 2400 once the temperature reached 100 ºC.

Electrochemical Stability: 80wt %WC-PE TRPS films were fabricated into coin cells and scanned at different voltage windows by the Autolab with a scan rate at 0.5mV s^{-1} for repeated cycles. For the cathode side, the scan window is 3 to 4.5 V vs Li/Li^+ and for anode side the scan window is 0.01 to 2 V vs Li/Li^+

3.2.1.4. Battery fabrications

Cathode preparation: Cathode were made by mixing NCM111 (Toda), PVDF (HSP-1800) and Super P at a mass ratio of 8:1:1 in NMP solvent by a Thinky mixer (Model ARE-310) at 2000 rpm for 30 mins. The slurry was cast by an auto-coater (MSK-AFA-II-VC-FH) on an Al current collector or a Al-TRPS current collector and dried at a vacuum at 80 ℃ for 10 h. For coin cells, the electrodes were cut by a pouch cutter with a

12mm-diameter. For pouch cells, the electrodes were cut by precision die cutter (MTI MSK-180/MSK-180L) with a size of 57 × 44 mm. The porosity was controlled around 45% by a rolling press (MTI MSKHRP03D). The mass loading is around 1.2 mAh cm^{-1}.

Anode preparation: Anodes were made by mixing graphite (GCP-8), PVDF (HSP-1800) and Super P at a mass ratio of 90:5:5 in NMP solvent by a Thinky mixer (Model ARE-310) at 2000 rpm for 30 mins. The slurry was cast by an auto-coater (MSK-AFA-II-VC-FH) and dried at a vacuum at 80 ℃ for 10 h. For coin cells, the electrodes were cut by a pouch cutter with a 13mm-diameter. For pouch cells, the electrodes were cut by precision die cutter (MTI MSK-180/MSK-180L)with a size of 58 × 45 mm. The porosity was controlled around 45% by a rolling press (MTI MSKHRP03D).

Battery fabrications: Half cells (2032 type) were fabricated with Cathode/anode, a lithium disc and separator (25 μm Celgard 2500). The electrolyte was 1 M $LiPF_6$ in ethylene carbonate/diethylcarbonate (1:1 v/v) (LP40). Full cells(2032 type) were fabricated with cathode (Al-TRPS-NCM111 cathode), graphite anode and separator (25 μm Celgard 2500). The electrolyte was 1 M $LiPF_6$ in ethylene carbonate/diethylcarbonate (1:1 v/v) (LP40). The typical N/P ratio was ~1.1-1.2. Pouch cells were fabricated with the same components, mass loading and N/P. A compact vacuum sealer (MTI MSK-115A-S) was employed to seal the pouch at – 90 Kpa for 5 s at 170 ºC to fully remove the gas. The typical capacity for a single-layer pouch was about 30 mAh.

3.2.1.5. Battery testing

Cycling Tests: Galvanostatic charge/discharge cycling was performed on Neware BTS-4000 for tracking cycling performance. The typical cycle condition for NCM half-

cell is at the constant current 0.1 C (1C = 160 mA) for first 2 cycles from 3 to 4.3 V (vs Li/Li^+), then the rest is cycle at 1C. The typical cycle condition for NCM/graphite full-cell is at the constant current 0.1 C (1C = 160 mA) for first 2 cycles from 2.7 to 4.3 V (vs Li/Li^+), then the rest is cycle at 1C. All cells cycled after resting for 12 hours.

Overheating Tests: The TRPS-based batteries were tested in a convection oven (MTI EQ-DHG-9015) held at 100 ºC to verify the thermal shutdown capability. The voltage and temperature changes were recorded by the Neware and a K-type thermal couple with a temperature logger, respectively.

External Shorting Tests: The external shorting tests were conducted by applying an extra-large current (120 ºC, corresponding to ~200 mA for the coin cells) through a Keithley 2400. The resistance and temperature changes were recorded by a Keithley 2400 and a K-type thermal couple with a temperature logger, respectively.

3.2.1.6. Characterizations

The morphology of the purchased and WC particles and the surface and cross section of TRPS films were examined with Scanning Electron Microscopy (SEM) using a FEI Quanta 250 SEM. X-ray diffraction (XRD) patterns were obtained by an X-ray diffractometer equipped with a Cu Kα radiation source (λ=1.5146 Å) at 30 kV and 10 mA (Bruker D2 Phaser, Germany).

3.2.2. Results and discussions

Conductive filler selection. To ensure the TRPS films can function well, a good conductive filler should reach the following properties: (1) high intrinsic electrical conductivity at room temperature (R.T.), (2) good electrochemical stability in the battery operation window, and (3) small thermal expansion coefficient in a wide temperature range (i.e. R.T. to 200 ºC), Based on above requirements, WC stands out as a promising candidate. WC is one of the most conductive materials among the carbide family, which has a bulk electrical conductivity ~ 5.2×10^4 S cm^{-1}.[63] As a comparison, the conductivity of typical cathode/anode is only ~ 2 S cm^{-1}.[64] In addition, the electrochemical stability of WC was measured by cyclic voltammetry for both cathode and anode sides with coin cells embedded with polyethylene-based TRPS 80 wt.% of WC (PE-80WC). The result indicates that WC is able to tolerate wide electrochemical window (**Figure 3.1a-b**) for the LIBs applications. In addition, WC has one of the smallest thermal expansion coefficients in common carbides/metals (**Table 3.1**), which is only 5.8 $10^{-6} \cdot K^{-1}$. Also, its melting temperature is ~2870 ºC, almost twice as Ni, which can ensure its structure won't be destroyed at some extreme temperature during shorting in LIBs. For a better control and simplicity of the fabrication, here we use commercial WC powder (Alfa Aesar, 99.5%) as the conductive fillers to fabricate the TPRS and explore the structure-property relationship. The XRD and SEM images were presented in **Figure 3.1c-d**.

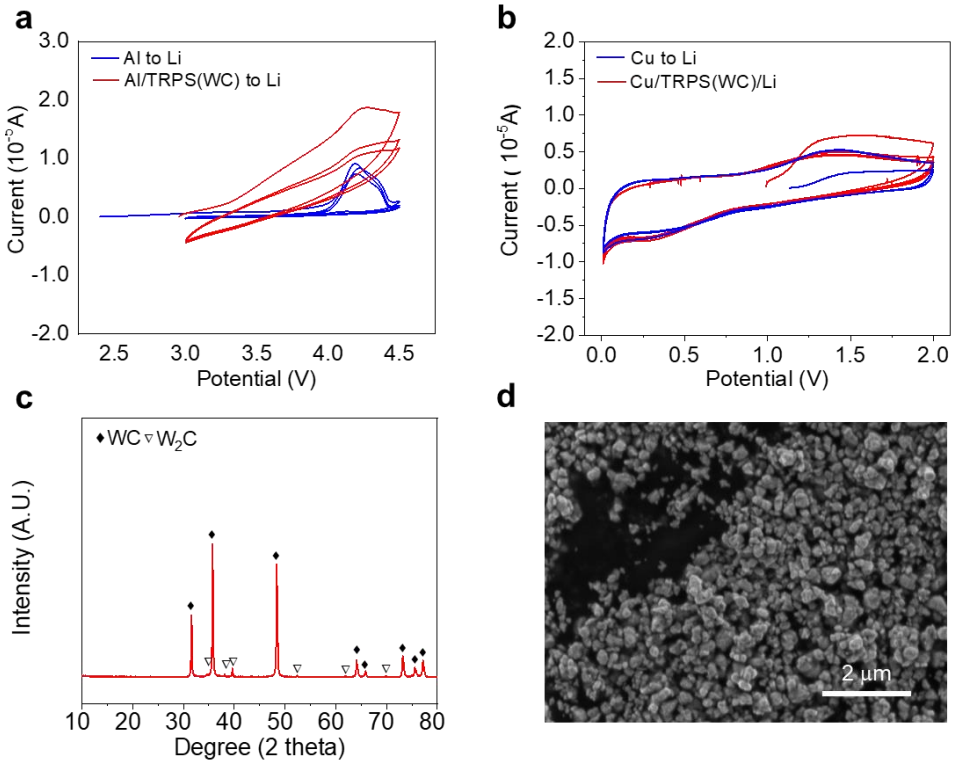

Figure 3.1 Cyclic voltammetry curves of (a) Al/TRPS (80wt% WC) films and Al current collector in the potential window of 3 to 4.5 V (versus Li/Li^+) and (b) Cu/TRPS (80wt% WC) films and Cu current collector in the potential window 0.01 to 2 V (versus Li/Li^+). Compared with Al and Cu current collector, WC-based TRPSs exhibit similar behavior. (c) X-ray diffraction patterns of C-WC. (d) SEM images of C-WC powders from Alfa Aesar.

Table 3.1 Properties of common carbides/metals

	Conductivity (10^6 S/m)	Thermal expansion factor ($10^{-6} \cdot K^{-1}$)	Melting temperature (°C)
Nickel	14.3	13.3	1455
Copper	59	17	1085
Tungsten carbide	5.22	5.8	2870
Titanium carbide	0.95	7.9	3065
Niobium carbide	2.8	6.9	3500
Carbon (Amorphous)	0.002	4.25	3550

Polymer selection. To exhibit an effective thermal response, a qualified polymer matrix must satisfy several requirements: (1) large thermal expansion coefficient (α), (2) suitable melting temperature (T_m), (3) electrochemically and physically compatible with electrolytes in the operation process, and (4) wide availability and low cost. Considering the aforementioned standards, polyethylene (PE), is the best candidate among promising candidates such as polyvinylidene fluoride (PVDF), polypropylene (PP), ethylene-vinyl acetate (EVA), cellulose acetate butyrate (CAB) and polytetrafluorethylene (PTFE). As one of the most commonly used polymers, it has a large α around 200×10^{-6} K^{-1} with a T_m in the range of 100~140 ^{o}C, which enables the largest thermal expansion response of TRPS near the self-heating temperature (the onset of the battery self-heat process, i.e., 115.2 ^{o}C) of LIBs before thermal runaway.[65] Composing only carbon and hydrogen atoms, PE is employed as the separator material for LIBs. Due to the demonstrated stability, there would be no chemical interaction when PE is used as the polymer matrix for TRPS. Furthermore, its nonpolar structure eliminates the potential swelling in electrolytes. However, to minimize the viscosity and maximize thermal expansion, low-density PE is preferred. Thus, its solvent compatibility, such as swelling effect, should be evaluated.

Table 3.2 Properties of polymer candidates for TRPS

	Thermal expansion coefficient -α (10^{-6} m/(m•°C))	Melting temperature T_m (°C)	Hansen solubility parameter δ_d	δ_p	δ_h	Interaction radius	RED
LP40	/	/	17.3	14	4.3	/	/
Polyethylene	200	99-138	16.9	0.8	2.8	6.6	2
Poly(vinylidene fluoride)	125	158-200	19.4	15.9	11.3	9.6	0.9
Polypropylene	105	120-176	17.7	2.9	1.2	6.2	1.9
Ethylene-vinyl acetate	205	58-112	18.9	-1.8	3.1	7.6	2.1
Polycarbonate	145	150-240	17.2	13.8	2.8	12.6	0.1
Polytetrafluorethylene	165	317-345	16.2	1.8	3.4	3.9	3.2

Swelling is the volume expansion of polymer due to the penetration of solvent molecules, which will deteriorate the switching capability. Hansen solubility parameters (HSB) [66] are introduced to describe the relative energy difference (RED) between the solvent and polymer quantitatively, which are:

$$RED = \frac{R_a}{R_0} \tag{1}$$

$$(R_a)^2 = 4(\delta_{d2} - \delta_{d1})^2 + (\delta_{p2} - \delta_{p1})^2 + (\delta_{h2} - \delta_{h1})^2 \tag{2}$$

where R_a is the Euclidean distance between the HSP for the solvent (s) and polymer, and it can be calculated by 3 solubility parameters: (1) δ_d , dispersion forces, (2) δ_p , polarity, and (3) δ_h, hydrogen bonding. R_0 is the interaction radius. To estimate the physical compatibility of polymer in the electrolytes, ethylene carbonate (EC)/ diethyl

carbonate (DEC) (50/50 vol%) was selected as the target system to evaluate the polymer-solvent interaction. The results are presented in **Table 3.2**. $RED < 1$ indicates that the polymer can swell and dissolve in the solvent. While PE has a $RED = 2$, so it is an excellent anti-swelling polymer against common electrolytes. The overall properties of different polymer candidates are summarized in **Figure 3.2**, which shows that PE is the best candidate as a polymer matrix for TRPS.

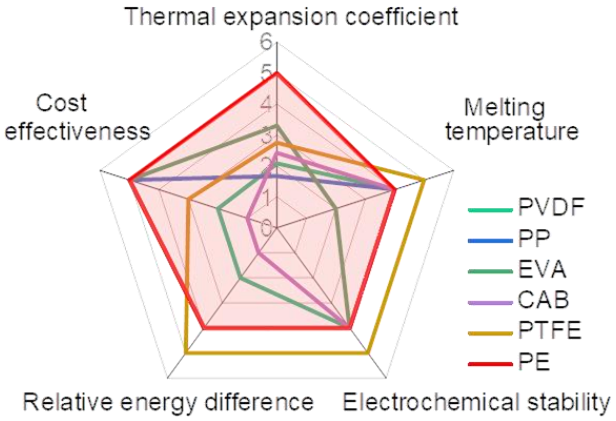

Figure 3.2 The required properties of the polymer candidates.

Slurry preparation and film casting

Common PE films are fabricated by film extrusion, injection molding and rotational molding, [67, 68] which require bulky and expensive equipment. To fabricate polyethylene (PE)-based TRPS films, a new casting technology needs to be developed because the current hot mixing method cannot meet such requirements: the film is often thick (~40-50 um) and the surface is nonuniform. As a result, a low-cost and convenient solvent-based casting method was developed in our lab. It is easier to control the thickness since the viscosity of the system is much less than that of the slurry mixtures obtained by

hot melting cast. As a result, the thickness can be readily manipulated by controlling the casting thickness. At the same time, a doctor-blade coating process help to minimize the variations of the film thickness. However, PE is a nonpolar polymer, and it cannot dissolve in common solvents to achieve desired viscosity, which makes it difficult to process. A great effort has been made to optimize solvent properties to make a desired slurry for film casting. Again, HSB model was employed to find a suitable solvent. Several non-polar solvents such as *p*-xylene, limonene, *n*-butylbenzene and cyclohexane are potential options since their RED with PE is smaller than 1 (**Table 3.3**).

Table 3.3 Data summary of Hansen solubility parameter, viscosity, vapor pressure and interaction distance between target solvent and solute (R).

	Hansen solubility parameters			Viscosity C_p (25 °C)	Vapor pressure K_{pa} (70 C°)	R	RED
	δ_d	δ_p	δ_h				
Polyethylene	16.9	0.8	2.8	/	/	/	/
Xylene	17.6	1	3.1	0.81(20 °C)	7.86	1.4	0.20
Limonene	17.2	1.8	4.3	0.92	3.20	1.9	0.29
n-butylbenzene	17.4	0.1	1.1	1.03	1.97	2.1	0.32
Cyclohexane	16.8	0	0.2	1.02(17 °C)	10.4(20 °C)	2.7	0.41

On the other hand, viscosity and volatility are critical in the film fabrication process. As a result, *p*-xylene was selected as the solvent for this study due to its good solubility ($RED = R/R_0 = 0.72$), small viscosity and reasonable volatility. A heat-insulating vessel was designed for the Thinky mixer to obtain consistent and uniform mixing

conditions. A typical solvent-cast fabrication procedure is shown in **Figure 3.3**. There are three major steps: mixing, casting and drying. First, PE, WC and xylene solvent were added into the container with desired ratios, then the container was transferred into a convection oven (80 °C) so that PE could be fully dissolved into the xylene solvent. After that, the precursor was thoroughly mixed in a Thinky mixer within the vessel to maintain the dissolving temperature of PE. Finally, the slurry was cast onto a glass/current collector in an oven (80 °C) and dried out to get the film.

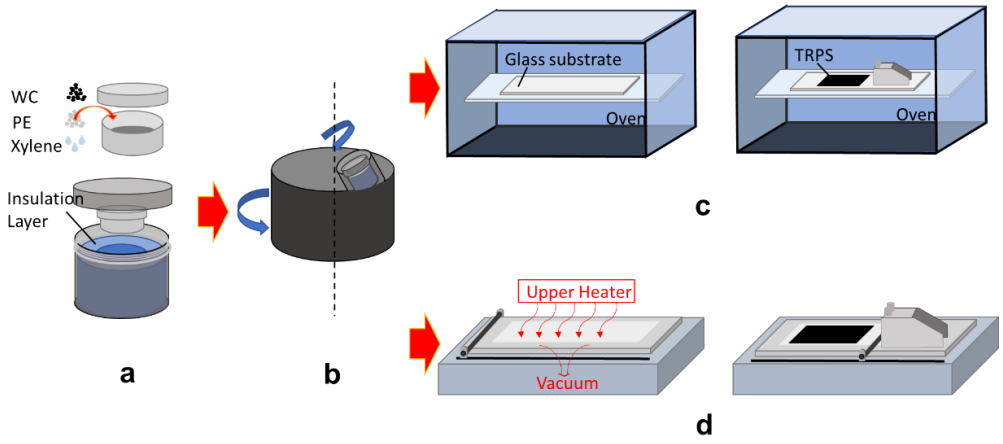

Figure 3.3 Schematic illustration of the solvent casting process on a glass substrate (a-c) or on current collectors (a, b &d). (a) raw materials and solvent are added into a mixer container and transfer into a heat insulation box for mixing. (b) The slurry is mixed by a Thinky mixer. (c) TRPS is directly cast on a glass substrate in a vacuum oven to get a freestanding film. (d) TRPS is cast on a current collector on an auto-coater with vacuum drawing

Filler size and distribution effects on TRPS properties.

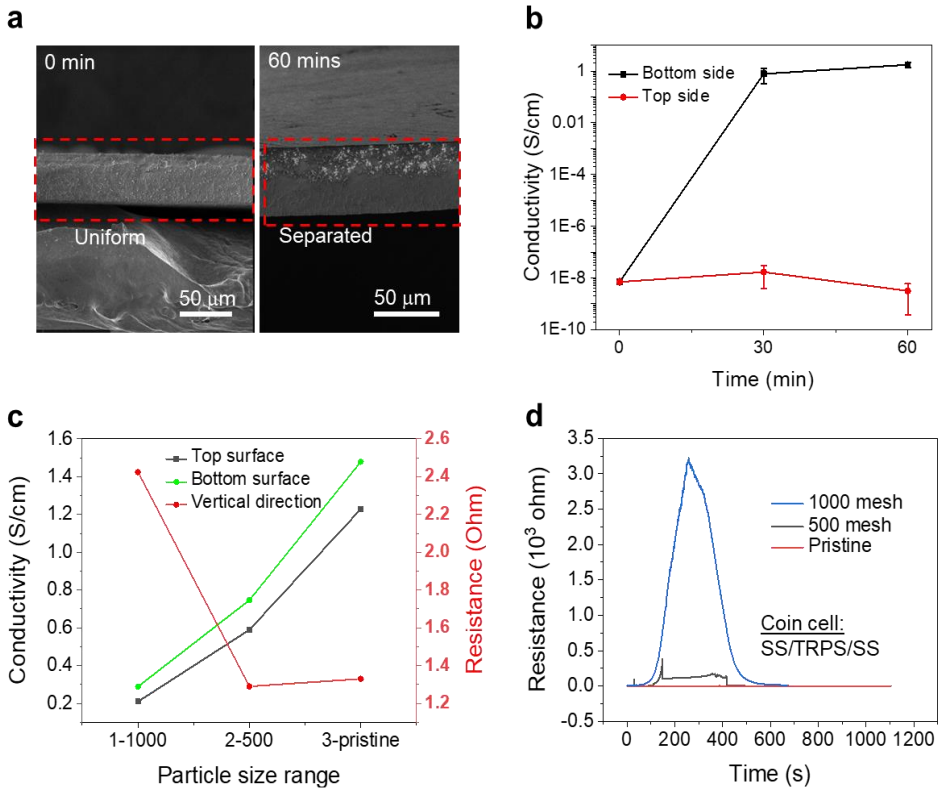

Figure 3.4 (a) Cross-section SEM images of TRPS samples prepared with different soaking time before drying (weight percent of WC was 60%; corresponding to a volume fraction of 16%). (b) Surface (lateral direction) conductivity of WC/PE films as a function of soaking time. (c) Top, bottom conductivities and resistance of the vertical direction of TRPS with WC fillers (80 wt%) at different size ranges (soak time = 0 min). (d) Corresponding switching response of TRPSs made from WC with a different size distribution.

The spatial distribution of fillers in the polymer matrix, which determines TRPS properties, highly correlates with the fabrication process. Depending on the drying temperature, evaporation rate and slurry viscosity, fillers will continually rearrange their distribution before fixing their position. To demonstrate filler reorganization during the drying process, time-based experiments were designed and the results are shown in **Figure 3.4a**. A culture dish was used to limit the evaporation rate by isolating the air convection from the slurry surface and therefore controlling the "soak time", which

indicates the duration of filler rearrange process. The cross-section scanning electron microscopic (SEM) images of two TRPS films with 60 wt. % of WC fillers exhibit distinct distribution behaviors upon different soak time. A uniform filler distribution with consistent conductivity on both sides was achieved when the film dries out instantly after casting, while an extended drying procedure leads to a filler separation and rearrangement, resulting in a 9-order of magnitude of conductivity difference between top and bottom surface (**Figure 3.5b**).

Table 3.4 Average size (in areas), and size variations of WC powders.

	Average areas (um^2)	Standard derivation	Range (Max-Min) (um^2)
1000 mesh	2.29	7.54	22
500 mesh	2.38	8.83	115
Pristine	3.99	14.10	282

*The areas were calculated by counting all pixel points which are identified as part of a single particle in SEM image by the Software Image J, then converted into areas in μm2. (The mechanism behind this is that, the software records the scale bar length (i.e. 10 μm) as how many pixels it occupies (i.e. 5 pixels), then it calculates the total areas of the SEM images (i.e. SEM images is 100 μm × 200 μm, which means it has 50 × 100 = 5000 pixels, so each pixel represents 4 μm2). This allows calculation of the area of each particle by knowing the number of pixels it has.

Moreover, the size distribution of WC is also a decisive parameter of TRPS properties. **Figure 3.5c-d** show the conductivity and thermal switching capability of TRPS films fabricated with WC fillers with different particle size range, which were prepared by screening through various mesh sizes (1000 and 500 mesh, more details in **Table 3.4**). TRPS films integrated with pristine WC particles (P-TRPS) have the highest conductivity but the slowest switching response under a high temperature (100 ^{o}C).

Further investigation from the SEM images in **Figure 3.5** shows that big WC chunks exist in P-TRPS. Large particles can facilitate the electron transport through the film more effectively but can also attenuate switching performance since it transfers electrons by bulk instead of inter-particle network. For the following demonstration, all WC particles were pre-treated by 1000 mesh screening and the TRPS films were prepared by immediate drying (soak time = 0 min) after casting to maintain a uniform spatial distribution of WC particles.

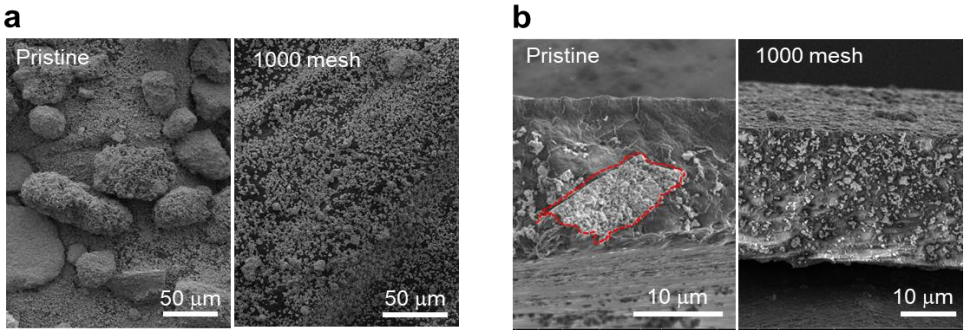

Figure 3.5 (a) SEM images showing the general distribution of particle size before (left) and after (right) screening by a mesh. (b) Cross-section SEM images of TRPS with pristine (left) and screened (right) WC particles (weight percent of WC was 80 wt.%; corresponding to a volume fraction of 20%).

Uniformity of TRPS Fabrication

To verify the uniformity and repeatability of the fabrication process, the conductivity and thickness variations among 9 identical pieces of films were measured for each batch of casting (Table 3.5). To evaluate, each sample was cut into 9 discs with a diameter of 18mm from a large piece of Al-TRPS (**Figure 3.6a**). All of the samples showed good consistency not only in conductivity and thickness, but also in the switching performance under high temperature (100 ^{o}C in convection oven). **Figure 3.6b** shows the

change of resistance a of two random samples upon temperature change. The two samples have similar resistance ramping rate.

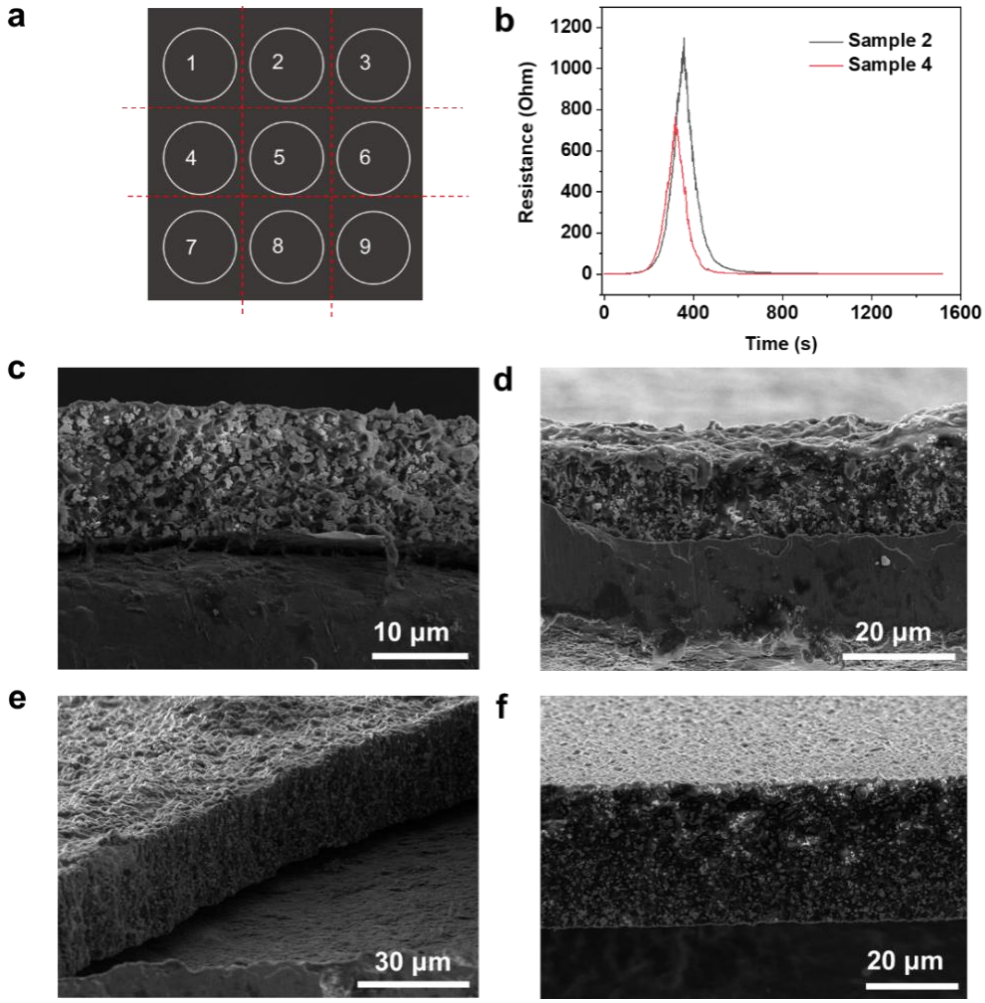

Figure 3.6 (a). Schematic illustration of the sample preparation to study the thickness and conductivity variation of WC/PE films. Note that the TRPS film was peeled off from the Al current collector for measurement. (b) Thermal swtiching response as a function of time for two random samples taken from the same piece of TPRS film (with 80wt.% of WC). (c-d) Cross-section SEM images of Al-TRPS films with different thickness.

Another benefit brought by our solvent-casting method is that the film thickness can be finely controlled. **Figure 3.6c-f** show different TRPS films casted on Al current collector, with the thickness around ~13, 18, 25 and 40 μm, respectively. By contrast, it

is difficult to obtain TRPS films with similar thickness by the hot-melting casting, which also causes coarse surfaces of the film.

Table 3.5 Summary of thickness and R.T. conductivity of Al-TRPS with 80wt.% of WC.

	Average	Standard derivation
Thickness	40.8	2.29
Top Conductivity	1.76	0.19
Bottom Conductivity	2.52	0.27
Vertical Resistance	1.10	0.30

Basic properties of TRPS.

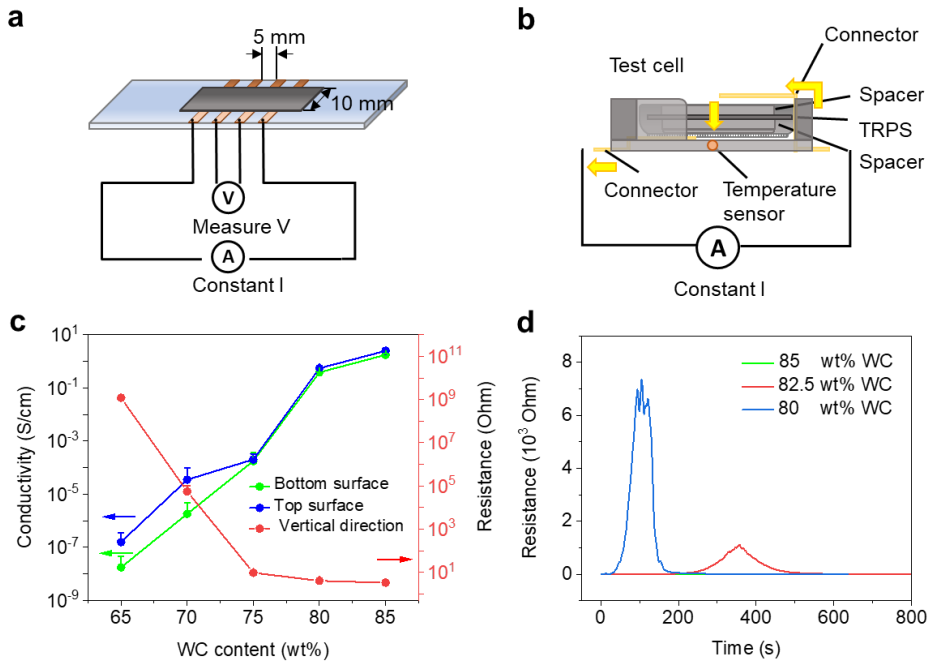

Figure 3.7 (a) Setup of the surface conductivity by the 4-probe method. (b) Setup of perpendicular resistance test. The TRPS is fabricated into a coin cell structure with the structure of Cathode cap ‖ spacer ‖ TRPS ‖ spacer ‖ anode cap. (c) Surface conductivity and vertical resistance of WC/PE films as a function of the WC ratio for TRPS. (d) Thermal switching response of TRPS as a function of time for samples made with different WC ratios.

TRPS films were prepared and the surface conductivity on both sides as well as the vertical resistance were measured as a function of WC contents by the setup shown in **Figure 3.7a**. The results can be found in **Figure 3.7c**. The surface conductivity reaches around 2 S cm^{-1} from 10^{-8} S cm^{-1} as the WC weight ratio increases from 65% to 85%, with a conductive threshold of 60 wt%. There is 1 order of magnitude difference in terms of conductivity between the top and bottom surface at low WC contents (below 75 wt%), which might be attributed to the nonuniform distribution of WC in PE matrix. However, the conductivities become consistent as WC content increases due to the formation of a robust conductive network. On the other hand, the vertical resistance rapidly reaches the same order as the robust network formed, and the resistance slightly decreases to ~ 3 **Ω**. Such anisotropic conductivity property of the as-prepared TRPS may provide more possibilities for other applications such as electronic sensors.[53, 69]

To investigate the potential of the as-prepared TRPS films for battery safety application, switching capability was measured within a coin cell-like setup (**Figure 3.7b**) and the results are shown in **Figure 3.7d**. TRPS with WC ratio between 80 wt% to 85 wt% were selected and stored in a 100 ^{o}C convection oven to stimulate a thermal-abuse condition. The PTC intensity (the logarithm of the ratio of the maximum resistivity to the resistivity at room temperature) increases to 3 for WC/PE films with 80 wt%. The TRPS barely shows switching response if continues raising WC contents to 85 wt% (PTC = 0.3). Consider both the PTC intensity and the R.T. conductivity, TRPS films with 80 wt% seems to be a good composition for real battery applications.

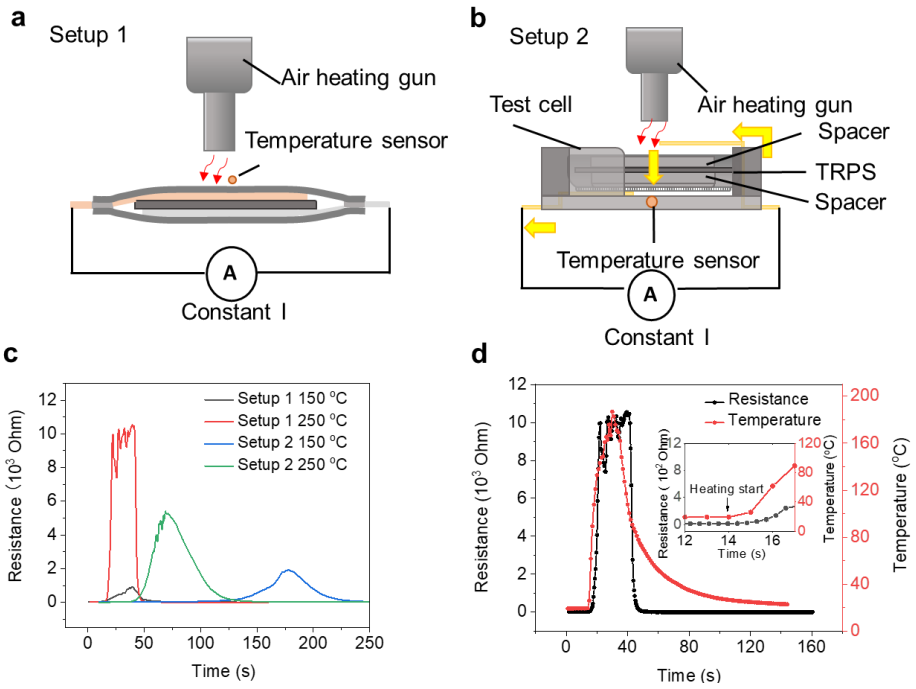

Figure 3.8 (a) Setup of the switching response rate test with a pouch-cell structure. The hot air gun was used to control the heating temperature at 150 °C and 250 °C, respectively. (b) Setup of the switching response rate test with a coin-cell structure. The hot air gun was used to control the heating temperature at 150 °C and 250 °C, respectively. (c) Resistance response of TRPS upon different heating rate through a hot-air gun (hot-air temperature set as 150 °C and 250 °C, respectively) for coin cell-like setup (1) and pouch-like setup (2). (d) Changes of temperature (surface) and resistance as a function of time for WC/PE film with 80 wt% of WC at different heating rate in a pouch cell.

To further exam the switching response rate corresponding to various thermal-abuse conditions in different scenarios, TRPS films were integrated into both coin-cell and pouch-cell structures to be tested with a hot air gun under different heating temperatures (**Figure 3.8a-b**). As shown in **Figure 3.8c**, a higher heating temperature (250 °C) gave rise to a more rapid and intense response of resistance change than a lower temperature (150 °C). Compared with coin-cell architecture, TRPS embedded in a pouch structure reveals a faster and more intense response to temperature changes, which indicates that the PTC intensity as well as the switching response rate are highly correlated

to the thermal abuse conditions. Overall, an instant and rapid temperature change will induce a more prompt and significant resistance increase. More details with temperature and resistance change with time were tracked and presented in **Figure 3.8d**. The rapid increase of temperature from R.T. to 110 °C triggers rapid increase of resistance without any delay (**Figure 3.8d, inset**), which can guarantee a real time shutdown of battery at safety events to prevent catastrophic consequences. In addition, the maximum resistance is about 10 times of that obtained at low heating temperature (150 °C, in a pouch-like structure), which further ensures the capability of the TRPS to immediately shut down cells at an extreme heating rate or high current conditions.

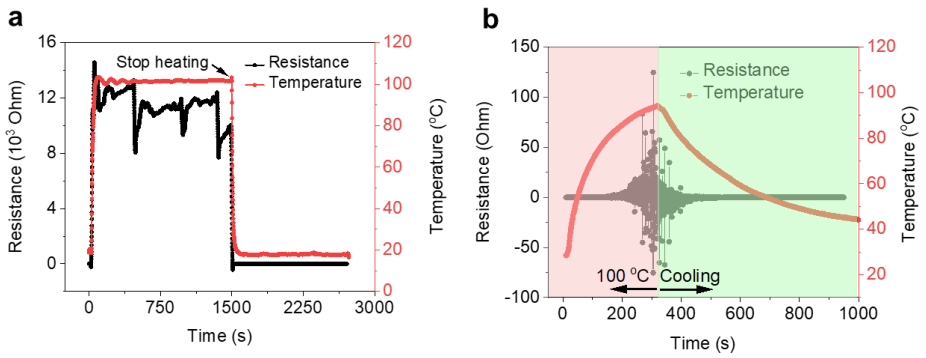

Figure 3.9 (a) Changes of resistance of WC/PE film in a convection oven held at 100 °C for 1500s. (b) Resistance variations per second and temperature change vs time of TRPS in the temperature chamber at 100 °C.

Ideally, TRPS films should maintain a high resistance under extreme temperature conditions (i.e. aging at 100 °C) for extended operation time while exhibiting stable resistance under normal temperature for battery operation, which are further demonstrated. As show in **Figure 3.9a**, even though the resistance fluctuates over time (1500s), the resistance value is higher than that obtained at shut down condition (**Figure 3.10d**). Meanwhile, the TRPS films are capable of retaining small resistance over a wide

temperature window. In **Figure 3.9b**, the resistance change is about ~0.001 Ω s^{-1} (0.065% of its initial resistance (1.54 Ω)) below 45 °C, even when the temperature goes up to 70 °C, the resistance change rate is only ~ 0.02 Ω s^{-1}.

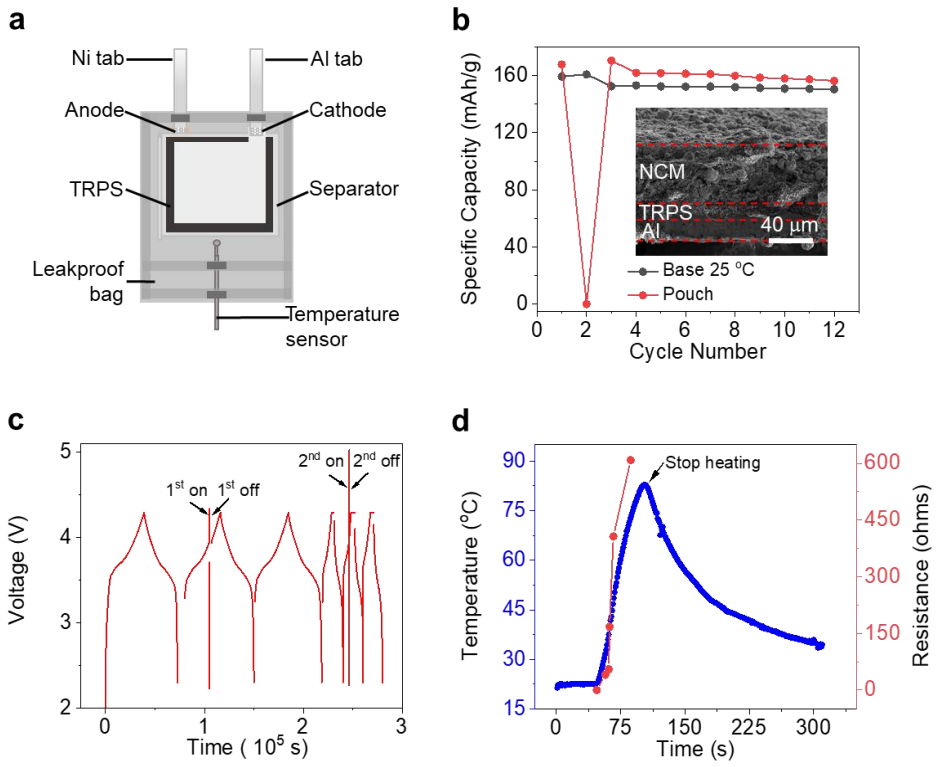

Figure 3.10 (a) Structures of the pouch cells for monitoring the temperature change vs time. The cathode size is 57 × 44 mm, and the anode is about 58 × 45 mm. The cathode mass loading is about 10 mg cm-2 for all cells, with a N/P ratio of ~1.1 to 1.2 for a full cell. (b) Cycling stability of the safety-improved TRPS pouch cell and a control NCM111/graphite cell without using any TRPS. Inset is the cross-sectional SEM image of a presentative cathode made with NCM111 coated on an Al-TRPS current collector. (c) Charge-discharge curves of Al-TRPS-embedded NCM111/graphite pouches before and after thermal shut down in a 100 °C convection oven. (d) Resistance and temperature changes as a function of time for a NCM111/graphite pouch cell with Al-TRPS during and after a thermal abuse.

To verify the safety properties of the TPRS for LIB applications, $LiNi_{1/3}Co_{1/3}Mn_{1/3}O_2$ (NCM111)/graphite pouch cells were fabricated with a temperature

sensor to monitor the temperature variations as in **Figure 3.10a**. The normal Al current collector was replaced with the TRPS- coated Al (Al-TRPS, inset of **Figure 3.10b**) in assembling the cell. A TRPS layer with a thickness of around 20 μm is in intimate contact between the Al substrate and NCM active layer, which is prepared through the aforementioned solvent casting method. The cycling results of the TRPS-integrated pouch cell and the control pouch (TRPS-free) are compared in **Figure 3.10b**, which shows similar capacity and stability at 25^{o}C.

Thermal abuse conditions were simulated by exposing the cycling TRPS-pouch to a convection oven at 100 ^{o}C to investigate the response of TRPS-cells against temperature variation . As shown in **Figure 3.10c**, at the beginning the TRPS-pouch cycled very well at R.T. conditions and then shut down immediately when it suffered from an overheating environment (100 ^{o}C in the oven). Meanwhile, it can resume to normal charge/discharge cycling once the temperature returns to the R.T. In thermal abuse conditions, the TRPS-pouch can effectively shut down for multi-times at various C-rate or charge/discharge condition (**Figure 3.11a-b**). To further verify the TRPS function in a more realistic condition, a bi-layer pouch with a capacity of 70 mAh was fabricated and tested (**Figure 3.11c**), which shows the same switching result. This experiment indicates that such an Al-TRPS-NCM integrated electrode can be extended to real multilayer pouches with excellent thermal switching capacities for improved LIB safety.

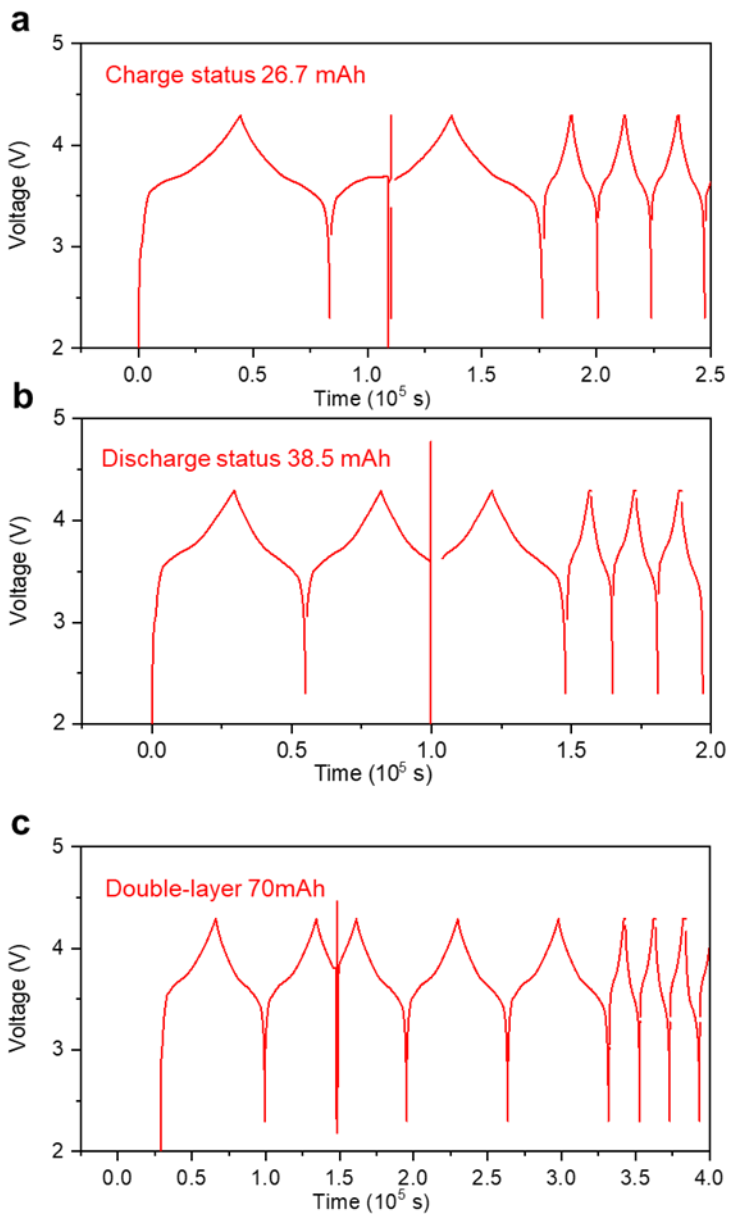

Figure 3.11 (a-c). Charge-discharge curves of Al-TRPS-embedded NCM111/graphite pouches before and after thermal shut down in a 100 ºC convection oven. (a) Shutdown test at charge status. (b) Shutdown test at discharge status. (c) Shutdown test of a double-layer pouch with a capacity of 70 mAh.

In addition, the evolution of resistance and temperature were recorded during a simulated overheating process (**Figure 3.10d**). The cell resistance reaches above 600 Ω after being exposed to the convection oven at 70 ºC for 20 s, showing a rapid and intense

thermal response. As the cell was intentionally cut off at 4.29 V in our experiment setting, the actual maximum cell resistance upon switching should be significantly larger than the calculated value based on Ohm's law. Nevertheless, the resistance curve is synchronous with the temperature curve, which indicates a fast and sensitive cell resistance change upon heating the TRPS in the pouch.

Cell electrical abuse testing

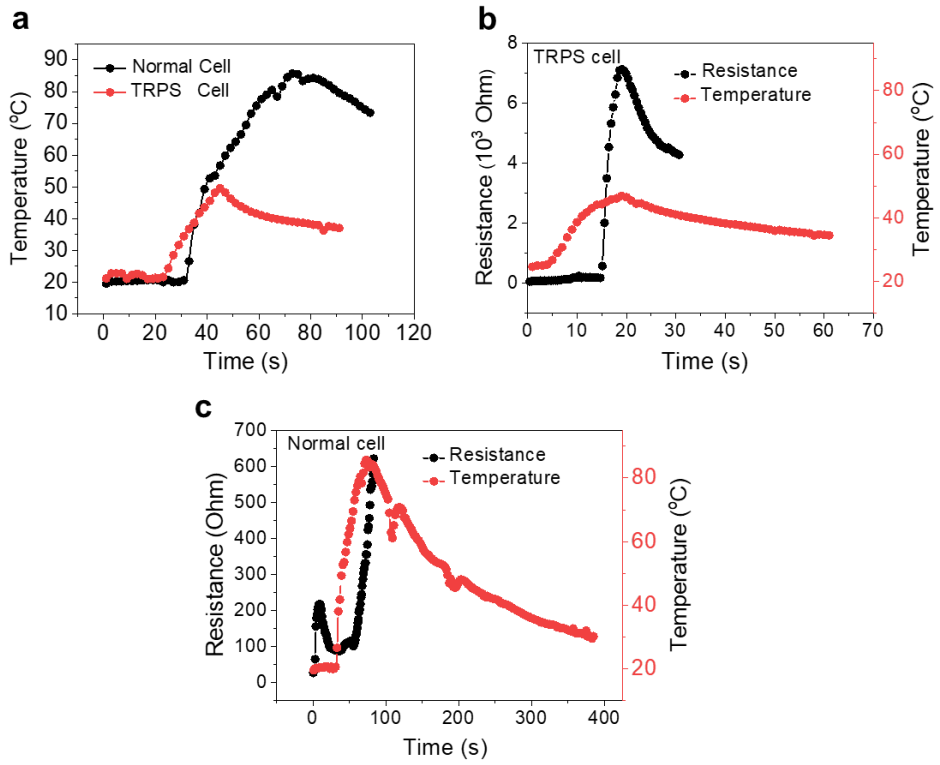

Figure 3.12 (a) Temperature profiles for different cells under external shorting using constant current (120 °C). For the TRPS cell, the temperature increasing rate was 1.27 °C s^{-1}, for the control cell the rate was 1.55 °C s^{-1}. (b). Temperature and resistance as a function of time for the TRPS cell. (c) Temperature and resistance as a function of time for a control coin cell (NCM111/graphite). The temperature rapidly increased to ~90 °C due to joule heating, then the current was terminated manually.

To more comprehensively inspect the safety protection capabilities of TRPS, electrical abuse tests were also conducted and the results are shown in **Figure 3.12**. To simulate the external shorting, a large current at 120 C rate (corresponding to ~200 mA, with a voltage upper limit at 21 V) was forced to pass through the cell, which can generate a huge amount of heat to trigger the thermal response of the TRPS and result in temperature ramping. As a result of the thermal response, the temperature of the TRPS cell stopped increasing at around 45 to 50 ^{o}C, while the temperature of the control cell continued to ramp to ~90 ^{o}C until the end of the simulated external short test. The results from resistance and temperature response with time indicate a rapid resistance change (PTC ~ 2.1) occurred after the initial temperature ramping due to the large current which leads to the reduction of "short" current. This greatly reduces the Joule heating and therefore prohibits further increase of temperature. On the contrary, the cell without TRPS showed negligible addition of resistance and the temperature showed no sign of decrease up to 90 ^{o}C before the end of the testing. (**Figure 3.12c**).

3.2.3. Conclusion

In summary, a scalable solvent-based fabrication process of TRPS films from slurry preparation to casting was designed and optimized specifically for PE matrix. WC was employed as conductive fillers to assemble highly conductive thermo-responsive switching composites. Systematic studies on fillers and polymer selection were conducted to illustrate the essential requirements for a good filler-polymer matrix system for TRPS materials. The fabrication process and the size distribution of fillers were investigated extensively to demonstrate their decisive roles in the properties of TRPS. By integrating

a thin TRPS directly into the current collector, LIB pouch cells with thermal abuse protection features can be assembled without additional modification of current industrial fabrication processes, which brings TRPS one step closer to large scale applications in LIBs.

3.2.3. Acknowledgement

Chapter 3, in full, is a reprint of the material “Scalable Solvent-Based Fabrication of Thermo-Responsive Polymer Nanocomposites for Battery Safety Regulation” as it is in preparation, Mingqian Li, Panpan Xu, Suk-woo Lee, Bum-young Jung, Zheng Chen The dissertation author was the first author of this paper and conducted all the essential research work.

Chapter 4. Synthesis of WC for TRPS

As discussed in Chapter 3, Tungsten carbide has been demonstrated to be a promising candidate as the conductive filler for TRPS materials. However, commercialized tungsten can achieve a uniform size with desired morphology (i.e. spiky structure), which can benefit the conductivity of TRPS composites. Traditional methods to synthesize tungsten carbide generally direct mix carbon materials with tungsten or tungsten ores such as scheelite ore by ball milling and carbonization at very high temperature ~1500 ºC. After pulverization and sieving process, tungsten carbide powder can obtain. A new synthetic method is required to prepare tungsten carbide with ideal morphology and shapes for TRPS applications.

4.1. Introduction

4.1.1. Literature review

Tungsten carbide as one of the most important raw materials, plays critical role in industrial machinery. Different strategies have been developed to synthesize tungsten carbide nano powders such as mechanical ball milling, [70-72] spray conversion process, [73, 74] and chemical vapor reaction, [75, 76] which usually demand prolonged reaction time and very high reaction temperature. Most of those methods dedicated to obtaining tungsten carbides with nano size smaller than 200 nm, but none of them emphasis the morphology control of tungsten carbide, which is also important for the applications of tungsten carbides.

4.1.2. Inspirations and strategies

To obtain WC with a desired morphology. Precursors with deigned morphology are good templates since for the solid-solid reaction, it is very difficult to control the growth of morphology uniformly. And based on previous experience, spiky structure can benefit the conductivity of TRPS materials. Also, to solve this potential issue from the interface of solid-solid phase, a hydrothermal method to coat glucose as the carbon source on the surface of WO_3, which should give a better mixing condition between carbon and precursor than physical mixing like ball milling and ensure there is no damage on their shape. Most importantly, a 2-step conversion is developed to separate the direct conversion process into reduction – carbonization process, which turns out to be the critical step to maintain the morphology of WO_3 precursor.

4.2. Synthesis of Appearance Controllable Carbides

4.2.1. Experimental

4.2.1.1. Synthesis of $WO_3 \cdot H_2O$ precursor

Spiky $WO_3 \cdot H_2O$ synthesis (~300nm): 3g of sodium tungstate dihydrate ($Na_2WO_4 \cdot H_2O$) was dissolved into 60 ml of H_2O, then 80 ml of 3M HCl was added into the solution to form light yellow depositions ($H_2W_4O_{13}$). After washing by water and ethanol for 3 times, the obtained $H_2W_4O_{13}$ was dried out in a convection oven at 80 ^oC. Then the $H_2W_4O_{13}$ was dissolved into 160 ml of 12 M HCl until the solution became transparent. 90 ml of water was dropped into the solution and kept stirring for 12 hrs to

get the spiky $H_2W_4O_{13}$. To convert as-synthesized spiky $H_2W_4O_{13}$ into WO_3, it was annealed at 500 ^oC for 30 mins.

Sphere $WO_3 \cdot H_2O$ synthesis (~1.5 um): 1.304 g of $Na_2WO_4 \cdot H_2O$ was dissolved into 16 ml H_2O with 0.5 g oxalic acid ($H_2C_2O_4$). Then 6 ml of 2 M HCl was added into the solution and sonicated for 1 hr by a probe sonicator. The product was washed by water and ethanol for 3 times and converted into WO_3 by the same heating procedure as mentioned before.

4.2.1.2. Annealing treatment of $WO_3 \cdot H_2O$

As-synthesized $WO_3 \cdot H_2O$ was transferred into a muffle oven (KSL-1100X-S-UL-LD) and heated up to 500 ^oC with a heating rate of 10 $^oC\ min^{-1}$ and held up at 500 ^oC for 30 mins to fully convert into WO_3.

4.2.1.3. Carbon Coating process of WO_3

Hydrothermal coating: Glucose and as-synthesized WO_3 with a different mole ratio of ~1.3-1 to 1 were dissolved in water and stirred for 20 mins. Then the solution was transferred into a Teflon container with a stainless autoclave and kept in a 150 - 170 ^oC convection oven for 7 several hours depending on the study.

High-temperature annealing coating: Phenolic resin (containing about 30% carbon) and as-synthesized WO_3 with different C to W ratio were dissolved into ethanol and stirred until uniformly disperse. After drying out the solvent, the precursor was put

into a tube furnace and heated up to 350 ºC for 1 hr and then ramped to 700 ºC and held for 1.5 hours in Ar to carbonize to obtain the carbon-coated WO_3.

4.2.1.4. WC Synthesis

1-step conversion: The carbon-coated WO_3 was directly heated to the carbonization temperature of 1000 ºC for 3 hours in 5% H_2 - 95% Ar to convert WO_3 into WC with a heating rate of 2 to 8 ºC min^{-1}.

2-step conversion: The carbon-coated WO_3 was heated up to 750 ºC and kept for 5 hours to be completely converted into W, then further carbonized into WC at 1000 ºC in 5% H_2 - 95% Ar with with a heating rate of 2 to 8 ºC min^{-1}.

4.2.1.5. Synthesis of MoO_2 hollow sphere precursor

0.28 g of molybdenyl acetylacetonate (sigma) was dissolved in 60 mL of n-butyl alcohol (sigma) under vigorous stirring. Then 10 ml of 1mol L HNO_3 was added dropwise into the above mixture until the formation of homogeneous yellow solution. After stirring for 1 h, the well-mixed solution was transferred into a Teflon-lined stainless autoclave and heated at 220°C for 12 h. After cooling down to room temperature, the black solid precipitate was collected and washed by DI water and ethanol for several times. After being annealed at 400°C in a muffle oven for 2 h, the white sample of α-MoO_3 hollow spheres were obtained. To successfully coat with carbon by the hydrothermal method, as-

synthesized MoO_3 was first converted into MoO_2 by reducing at 700 ºC for 5 hours in 5% H_2 - 95% Ar since MoO_3 will decompose during the hydrothermal condition.

4.2.1.6. Carbon coating process of MoO_2

Hydrothermal coating: Glucose and as-synthesized MoO_2 with a different mole ratio of ~1 to 1 were dissolved in water and stirred for 20 mins. Then the solution was transferred into a Teflon container with a stainless autoclave and kept in a 150 - 170 ºC convection oven for 7 several hours depending on the study.

4.2.1.7. Mo_2C Synthesis

2-step conversion: The carbon-coated MoO_2 was heated up to 700 ºC and kept for 5 hours to be completely converted into Mo, then further carbonized into Mo_2C at 1000 ºC in 5% H_2 - 95% Ar with with a heating rate of 5 ºC min^{-1} for 3 hours.

4.2.1.8. Preparation of TRPS materials

Solvent-casting method preparation of PE-based TRPS : The as-pretreated WC were mixed with PE (Epolene® C-13 Polymer) at different ratio in xylene by a Thinky mixer (Model ARE-310) in a designed heat-insulating container. Before mixing, the mixture was heated in a 80 ºC convection for 15 mins oven to dissolve PE completely. To maintain the temperature of the slurry, a designed heat-insulating container was employed. The slurry was mixed in the Thinky mixer at 2000 rpm for 8 mins. Then the slurry was then coated on a glass substrate or carbon-coated Al current collector with vacuum drawing and by a doctor blade. The slurry was dried out immediately. The slurry was also

tested with different soaking time to study the particle distribution and uniformity in the obtained TRPS film.

4.2.1.9. Characterizations of TRPS properties

Conductivity measurement: The sample were cut into a circular shape with a diameter of 19 mm and the thickness was measured by a micrometer before testing. The surface electrical conductivity of both surface at R. T. was measured by a four-point probe with a Keithley 2400. To measure the vertical resistance, TRPS films were fabricated into a 2032 coin cell with a structure of spacer ‖ TRPS film ‖ spacer to provide constant contact areas and pressure. Then the resistance was measured at R.T. by a two-point probe method through a Keithley 2400. To obtain accurate test results, each sample was measured for multiple times at different positions and the average value were calculated to represent the conductivity.

Intensity of Switching Response (PTC intensity) measurement: The time-dependent resistance measurements of various composites was conducted with a four-probe method by putting samples into a convection oven at 120 ^{o}C. The resistance was recorded by a Keithley 2400. The time-dependent temperature measurements of TRPS was tracked by a K-type thermal couple on a temperature logger.

Rate of Switching Response measurement: A hot-air gun (YiHua SMD Reworks Station 852D+) was used for response rate testes by heating samples under different temperatures (250 ^{o}C and 350 ^{o}C) with different tests configurations for both coin-cell

like and pouch-like structures. The resistance and temperature changes were recorded by the same way as switching resistance response tests.

Switching reversibility measurement: To obtain the performance of switching performance under repetitive heating/cooling cycle, as-prepared TRPS films were transferred into a 120 ºC convection oven until switching under overheating, then removed from the oven and cooled down to room temperature naturally until the conductivity resumed. Repeat this process consistently to get reversible switching performance. The resistance was recorded by a four-probe method through Keithley 2400.

Resistance stability measurement: TRPS films were transferred into a 50/100 ºC convection oven for 15 mins. A k-type temperature sensor was used to monitor the temperature variations. Resistance was recorded by a four-probe method through Keithley 2400 once the temperature reached 100 ºC.

4.2.1.10. Battery fabrications

Cathode preparation: Cathode were made by mixing NCM111 (Toda), PVDF (HSP-1800) and Super P at a mass ratio of 8:1:1 in NMP solvent by a Thinky mixer (Model ARE-310) at 2000 rpm for 30 mins. The slurry was cast by an auto-coater (MSK-AFA-II-VC-FH) on an Al current collector or a Al-TRPS current collector and dried at a vacuum at 80 ℃ for 10 h. For coin cells, the electrodes were cut by a pouch cutter with a 12 mm-diameter.

Anode preparation: Anodes were made by mixing graphite (GCP-8), PVDF (HSP-1800) and Super P at a mass ratio of 90:5:5 in NMP solvent by a Thinky mixer (Model ARE-310) at 2000 rpm for 30 mins. The slurry was cast by an auto-coater (MSK-AFA-II-VC-FH) and dried at a vacuum at 80 ℃ for 10 h. For coin cells, the electrodes were cut by a pouch cutter with a 13mm-diameter. For pouch cells, the electrodes were cut by precision die cutter (MTI MSK-180/MSK-180L) with a size of 58 × 45 mm. The porosity was controlled around 45% by a rolling press (MTI MSKHRP03D).

Battery fabrications: Half cells (2032 type) were fabricated with Cathode/anode, a lithium disc and separator (25 μm Celgard 2500). The electrolyte was 1 M $LiPF_6$ in ethylene carbonate/diethylcarbonate (1:1 v/v) (LP40). Full cells (2032 type) were fabricated with cathode (Al-TRPS-NCM111 cathode), graphite anode and separator (25 μm Celgard 2500). The electrolyte was 1 M $LiPF_6$ in ethylene carbonate/diethylcarbonate (1:1 v/v) (LP40). The typical N/P ratio was ~1.1-1.2.

4.2.1.11. Battery testing

Cycling Tests: Galvanostatic charge/discharge cycling was performed on Neware BTS-4000 for tracking cycling performance. The typical cycle condition for NCM half-cell is at the constant current 0.1 C (1C = 160 mA) for first 2 cycles from 3 to 4.3 V (vs Li/Li^+), then the rest is cycle at 1C. The typical cycle condition for NCM/graphite full-cell is at the constant current 0.1 C (1C = 160 mA) for first 2 cycles from 2.7 to 4.3 V (vs Li/Li^+), then the rest is cycle at 1C. All cells cycled after resting for 12 hours.

Overheating Tests: The TRPS-based batteries were tested in a convection oven (MTI EQ-DHG-9015) held at 120 ºC to verify the thermal shutdown capability. The voltage and temperature changes were recorded by the Neware and a K-type thermal couple with a temperature logger, respectively.

4.2.1.12. Characterizations

The morphology of the purchased and WC particles and the surface and cross section of TRPS films were examined with Scanning Electron Microscopy (SEM) using a FEI Quanta 250 SEM. X-ray diffraction (XRD) patterns were obtained by an X-ray diffractometer equipped with a Cu Kα radiation source (λ=1.5146 Å) at 30 kV and 10 mA (Bruker D2 Phaser, Germany).

4.2.1.13. Calculation of reaction energy

Reaction energies for different WO_x phases were obtained from the method described by Ong,[77] as

$$\Delta G = G_{products} - G_{reactants}$$

$$\approx H_{products} - H_{reactants} - T(S_{gascous\ prodcuts} - H_{gascous\ reactants})$$

Where the enthalpy, H, is approximated as the internal energy E, at 0 K.

To determine ΔG, the internal energy for different WO_x phases were adopted from the Materialsproject database. For gas phase like O_2, CO H_2 and H_2O, all related thermodynamic data were obtained from NIST-JANAF Thermochemical Tables. Calculations for redox reactions are based on per O_2 eV.

4.2.2. Results and discussions

Figure 4.1. schematic illustration of the synthesis methods. The 2-step conversion consists of one reduction procedure separated with the following carbonization process at high temperature; The 1-step conversion reduce and carbonize WO_3 at high temperature.

A novel universal 2-step conversion synthesis method was designed, and the overall synthesis pathways are illustrated in **Figure 4.1a**. Compared with traditional synthesis method (referred as 1-step conversion in the following), which only has 1-step, the transformation process from WO_3 to WC is divided into two steps: convert WO_3 into W completely at low temperature, then carbonization W into WC at high temperature. Great advances are brought by such a reduction-carbonization process, which allows us to maintain the morphology of WO_3. As shown in **Figure 4.2d**, WC particles exhibit a hierarchical secondary structure with a spherical shape, which is almost identical as its WO_3 precursor and W intermediate **Figure 4.2c-d**. To the best of our knowledge, this is the first time WC with such an ordered spherical structure were synthesized. More importantly, this strategy can be easily extended to obtain WC with any desired architecture. For example, flower-like spiky WC particles with a size ~ 200 to 300 nm

were successfully synthesized by employing WO_3 with similar structure (**Figure 4.3**). To future demonstrate the possibility of this method, a pure Mo_2C phase (**Figure 4.4a**) with a hollow structure were managed to synthesize (**Figure 4.4d**). The hollow spherical structure of MoO_2 with a uniform size around 800 nm is well maintained (**Figure 4.4b-c**).

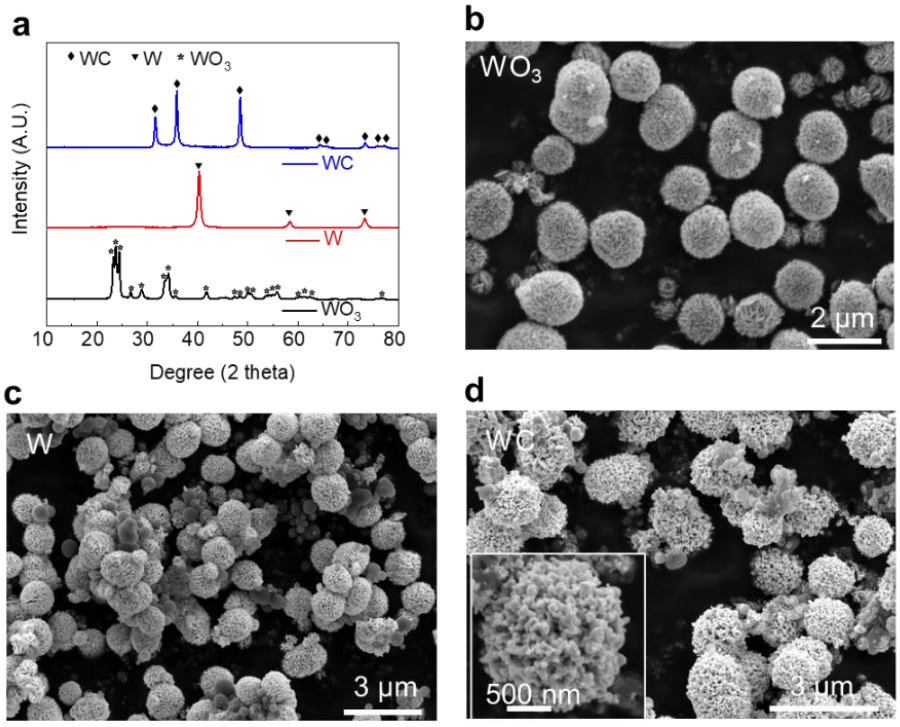

Figure 4.2. (a) XRD patterns of as-prepared WO_3 before (black line) and after reduction (red line) and carbonization (blue line). (b) SEM image of as-prepared WO3. (c) SEM image of W after reduction at 750 °C for 5 hours. (d) SEM images of the as-synthesized spherical WC (p-WC).

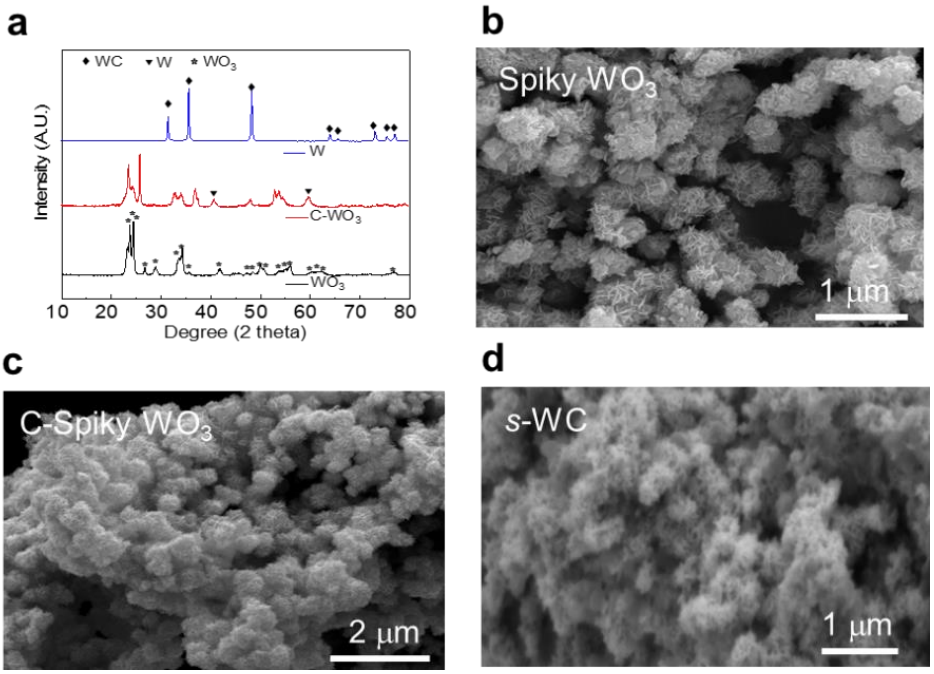

Figure 4.3. (a) XRD patterns of as-prepared spiky C-WO_3 before (black line) and after reduction (red line) and carbonization (blue line). (b) SEM image of spiky as-prepared WO_3. (c) SEM image of W after reduction at 750 ºC for 5 hours. (d) SEM images of the as-synthesized spiky WC (p-WC).

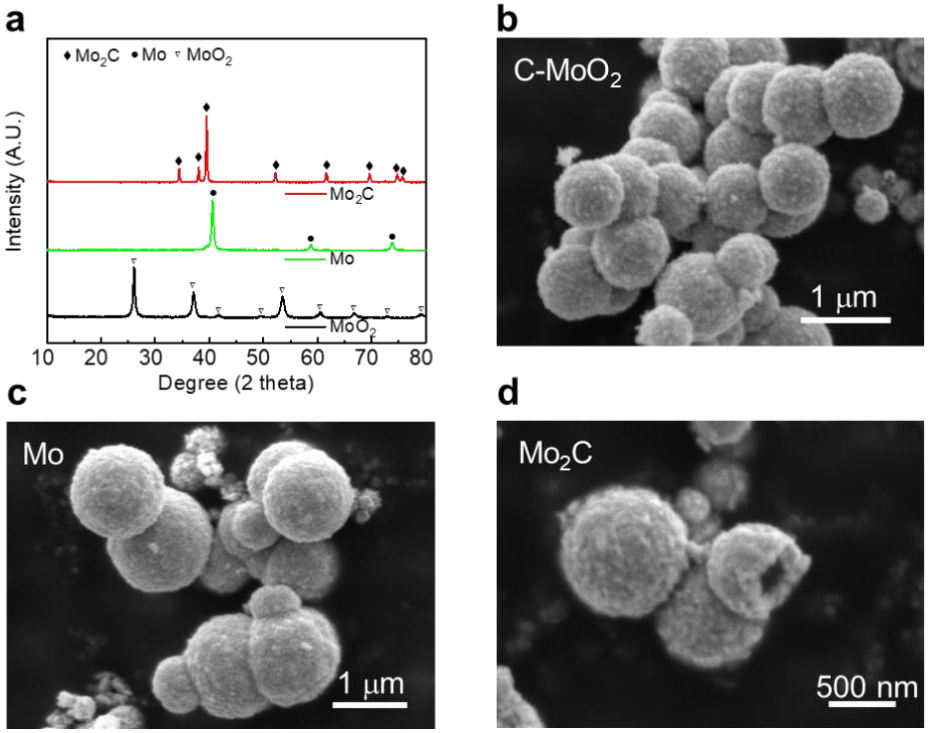

Figure 4.4 (a) XRD patterns of as-prepared C-MoO_2 before (black line) and after reduction (green line) and carbonization (red line). (b) SEM image of as-prepared C-MoO_2. (b) SEM image of Mo after reduction at 700 ºC for 5 hours. (c) SEM image of Mo_2C after carbonization at 1000 ºC for 3 hours.

Phase compositions and morphology were investigated carefully through comprehensive studying of synthesis variables. To obtain WC free from impurities, factors such as carbon ratios, conversion time and temperature are critical, and **Figure 4.5** shows the X-ray diffraction pattern (XRD) of WC synthesized at different conditions under 2-step conversion. It turns out carbon ratio between glucose to WO_3 precursor (in molar) not only dominate the phases but also the morphology. A pure phase can be obtained as the ratio is larger than 1 (**Figure 4.1a**), but it cannot retain the pristine structure when the ratio is lower than 1.2 (**Figure 4.5b-c**). In addition, 1000 ºC is the minimal carbonation temperature to eliminate impurity phases such as W and W_2C (**Figure 4.6**),

and the prolong of reaction time above 3 hours won't bring any change of the WC phase (**Figure 4.7a**). No distinct morphology changes bring by varying the synthesis time or temperature (**Figure 4.7b-c**). As a result, carbonization at 1000 ºC for 3 hours is employed as the optimal synthesis condition, which requires lower energy than traditional ball milling synthesis.

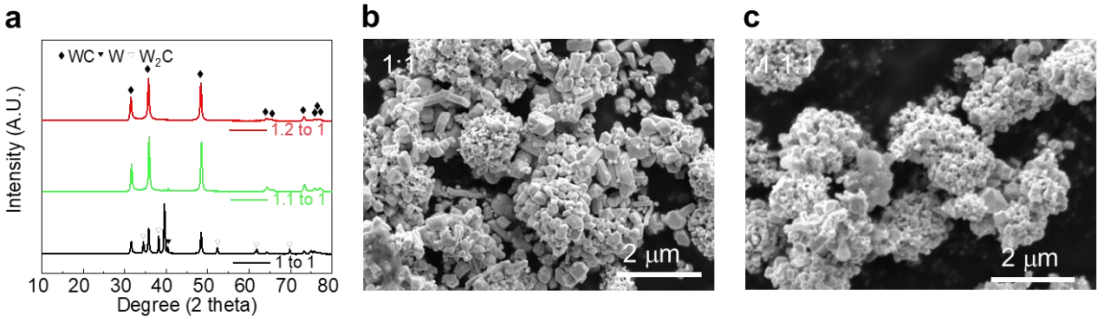

Figure 4.5. (a) XRD patterns of WC synthesized with different carbon ratio at 1000 ºC for 3 hours.(b) SEM image of WC synthesized with C to W ratio = 1:1. (c) SEM image of WC synthesized with C to W ratio = 1.1:1.

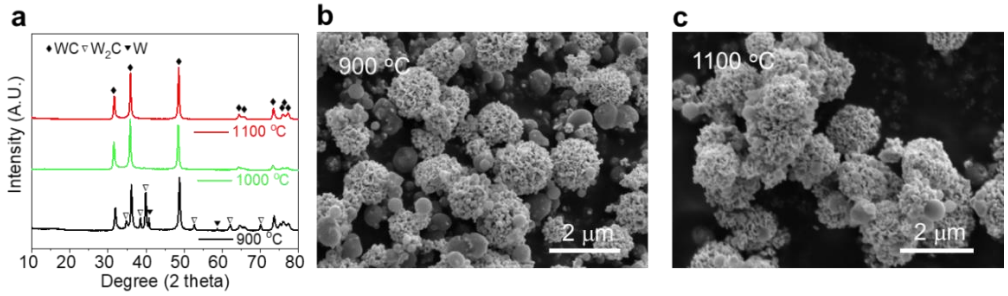

Figure 4.6. (a) XRD patterns of WC synthesized at different temperature with same C to W ratio (b) SEM image of WC synthesized at 900 ºC. (c) SEM image of WC synthesized at 1100 ºC.

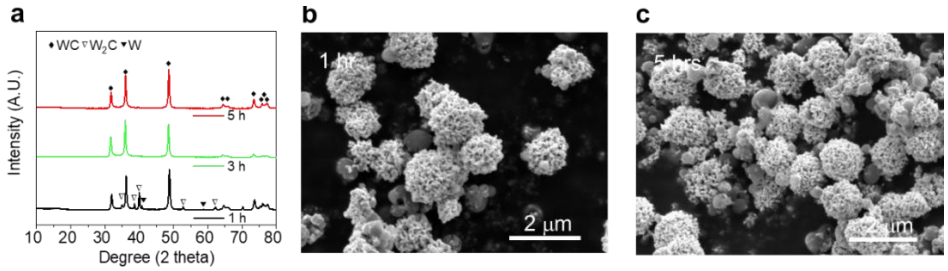

Figure 4.7. (a) XRD patterns of WC synthesized for different time with same C to W ratio (1.2) at 1000 ºC. (b) SEM image of WC synthesized at 1000 ºC for 1 hour. (c) SEM image of WC synthesized at 1000 ºC for 3 hours.

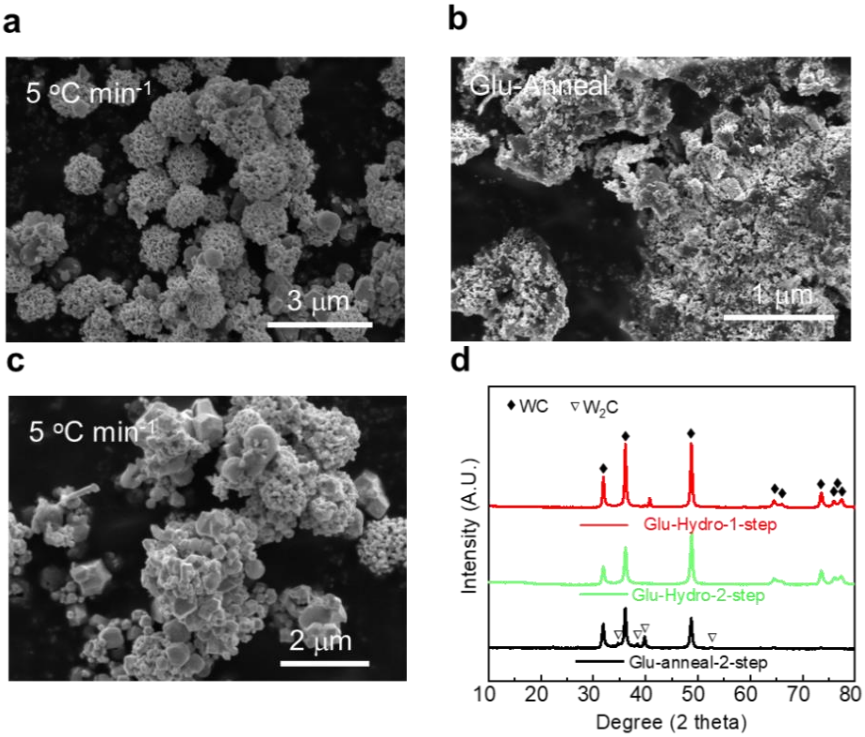

Figure 4.8 (a) SEM image of hydrothermal-coated WC synthesized by the 2-step conversion with a heating rate of 5 ºC min^{-1}. (b) SEM image of anealled-coated WC synthesized by the 2-step conversion with a heating rate of 5 ºC min^{-1} (c) SEM image of hydrothermal-coated WC synthesized by the 1-step conversion with a heating rate of 5 ºC min^{-1} (d) XRD patterns of as-synthesized WC under different conditions.

To maintain the architecture of WO_3 precursor after the reduction-carbonization conversion process, the coating method, conversion steps and temperature ramping rate are vital. **Figure 4.8a-b** show the morphology of as-synthesized WC through different

coating methods. The spherical secondary structure of WO_3 is well-maintained even after carbonization at 1000 ^oC, while only big chunks of WC and carbon mixture without a particular structure exist when the same WO_3 precursor prepared by the annealing coating method. Such a huge difference might be result from the uniformity of coating. During the hydrothermal process, glucose form a carbonaceous layer on WO_3 surface by dehydration[78], which is more uniform than that from simple physical mixing process. However, the architecture will be destroyed even with a good coating if it is 1-step conversion. **Figure 4.8c** displayed the WC synthesized through the 1-step method. The original structure collapsed, and the primary particles gradually fused together into polyhedrons. To further demonstrate the transformation process dominates the shape evolution, C-WO_3 precursors were converted into WC with different temperature ramping rates for both methods and the corresponding SEM images and XRD can be found in **Figure 4.9**. The spherical structure can be maintained for WC synthesized by 2-step conversion method even with a ramping rate at 8 $^oC\ min^{-1}$, but it degraded into small cubic or polyhedron at 2 $^oC\ min^{-1}$ if C-WO_3 directly transform into WC. As a result, the two-step conversion process is an indispensable step to obtain WC with desired structure.

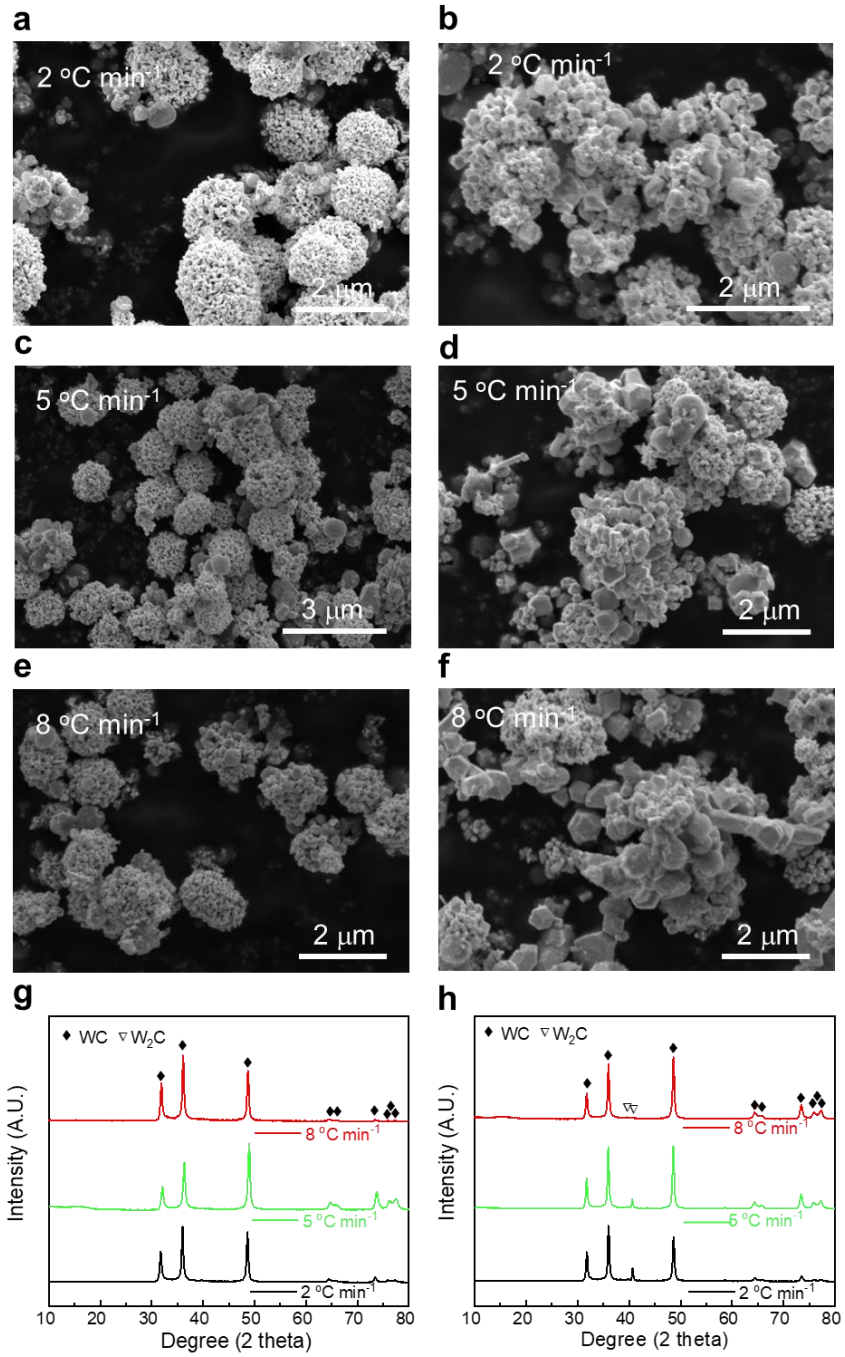

Figure 4.9 (a,c,e) SEM images of WC prepared by 2-step conversion with different heating rate at 2 °C min^{-1}, 5 °C min^{-1}, and 8 °C min^{-1}, respectively. (b,d,f) SEM images of WC prepared by 1-step conversion with different heating rate at 2 °C min^{-1}, 5 °C min^{-1}, and 8 °C min^{-1}, respectively. (g) XRD patterns of WC prepared by 2-step conversion. (h). XRD patterns of WC prepared by 1-step conversion.

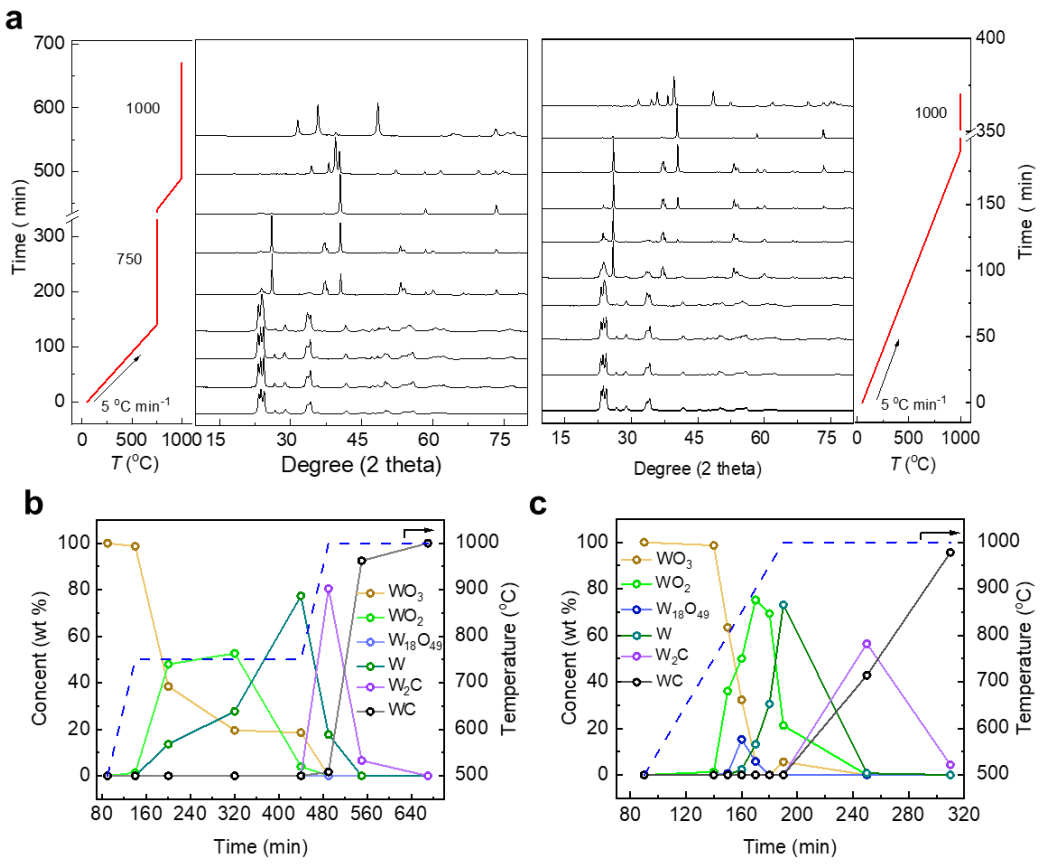

Figure 4.10 (a) XRD patterns of WC at different stages during synthesis for 2-step conversion (left) and 1-step conversion. (b) The phase weight percent of obervered phase at different reaction time for the 2-step conversion method obtained from Rietveld refinement of the XRD patterns. (c) The phase weight percent of obervered phase at different reaction time for the 1-step conversion method obtained from Rietveld refinement of the XRD patterns.

To understand the formation of WC, ex-situ XRD were conducted to observe the phase evolution process for both synthetic routes from the precursors to the final product. **Figure 4.10a** shows the results of the transition process: During the first step of WO_3 reduction, the as-prepared C-WO_3 mixture is heated up with a heating rate (5 ^{o}C min^{-1}) to 750 ^{o}C and held for 5 hours under 5% H_2-Ar. Only WO_3 is observed at 500 ^{o}C since the coated carbon is an amorphous phase. No new phase appears until the temperature reaches 750 ^{o}C, where the WO_3 starts to reduce to WO_2. And as temperature maintained still, a

new phase such as W formed, the conversion of WO_2 to W processes simultaneously as WO_3 keeps converting to WO_2, which indicates both steps are thermodynamical favorable at 750 ºC. The reduction process is slow during the transition since there is still a minor amount of WO_3 (18 wt%) in the system even after 5 hours of reaction, while the following carbonization process is rapid: the dominated phase change from W (77% at 750 ºC) to W_2C (80.5 % at 1000 ºC) within 50 mins during the ramping process, followed by deep carbonization of W_2C into WC when holding at 1000 ºC for 1 hour. More than 90 wt% of WC was obtained. Such a fast phase formation indicates the diffusion of C into the body-centered cubic W framework is quick. A pure WC phase was obtained in the end of carbonization at 1000 ºC for 3 hours. The overall conversion process can be summarized as follow 2 steps:

$$WO_3 \rightarrow WO_2 \rightarrow W \quad (1)$$

$$W \rightarrow W_2C \rightarrow WC \quad (2)$$

On the other hand, the reduction process is different for the 1 step method in **Figure 4.10c**. Initially, the phase compositions are identical to that of the mentioned 2-step method, but as temperature keeps increasing without holding at 750 ºC, WO_3 contents drops dramatically. Near 40 wt% of the compounds are WO_2 at 800 ºC (10 mins). Almost all WO_3 are replaced by suboxide within 30 mins, and A new phase $W_{18}O_{49}$, appears at 800 ºC and then vanishes after reaching 950 ºC, suggesting a rapid reorganization of the W-O structure. At the same time, W starts to accumulate from 850 ºC and accounts for 70 wt% of the mixture at 1000 ºC, with some WO_2 and WO_3 residues exist. After 3 hours of carbonization, compounds of WC (95.6%) and W_2C (4.4%) are synthesized. The reduction and carbonization process are interlaced, which may stand by:

$$WO_3 \rightarrow WO_2 \rightarrow W_{18}O_{49} \rightarrow W \quad (3)$$

$$W \rightarrow W_2C \rightarrow WC \quad (4)$$

What brings such differences in terms of reduction species and sequences? To unveil the phase transition mechanism, the reaction energies for various WO_x phases during the reduction process are calculated at the WO_3/C/H_2 interface in **Figure 4.11a**.[79] For the WO_3 reduction reactions, the temperature effect on the free energy mainly reflects in the entropy change of gaseous O_2, without considering the minimal variations of entropy in the solids.[77] At the interface between powder precursors, there are no stoichiometric constraints from the macroscopic WO_3/C ratio and therefore reactions with the maximum reaction energy are preferred. As a result, with the presence of H_2 as the reductant, WO_2 phase is demonstrated to have the lowest negative reaction energy of all WO_x phases at reduction temperatures and is most likely present in the reduction process first, which is confirms by ex-situ XRD in **Figure4.10** for both methods.

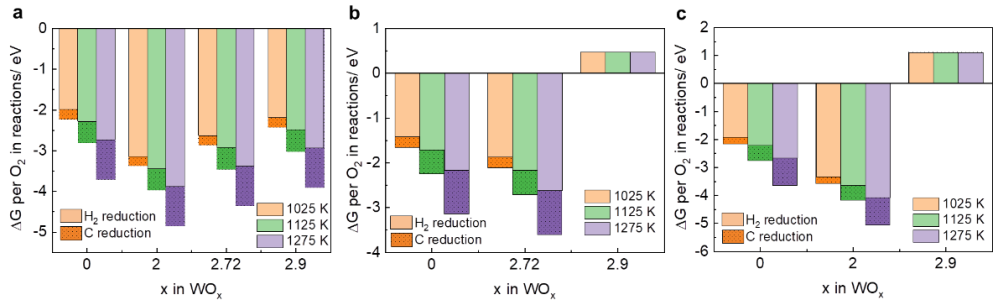

Figure 4.11. Reaction energies for the formation of the lowest WO_x phase as a function of x. (a) reaction energy per O_2/eV of the reduction of WO_3. (b) Reaction energy per O_2/eV of the reduction of WO_2. (c) Reaction energy per O_2/eV of the reduction of $W_{18}O_{49}$.

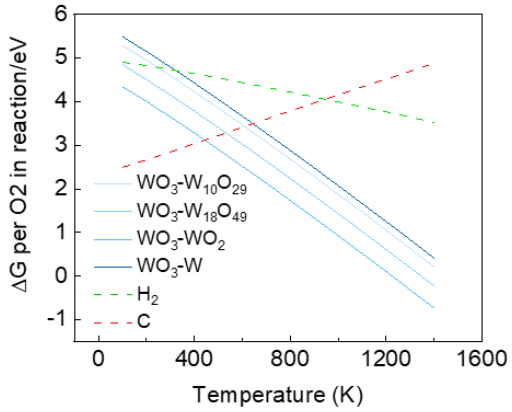

Figure 4.12. Modified Ellingham diagram for reduction reactions of WO_3 with the present of C and H_2

Differences appear when WO_2 experiences further reduction. To figure out the ideal reduction species and sequences, the reaction energy at the $WO_2/WO_3/H_2/C$ interface under unconstraint stoichiometric condition is estimated in **Figure 4.11b**. $W_{18}O_{49}$ is the most favorable products with the lowest negative reaction energy, followed by W metal. Experimentally, it matches well with the 1-step method, while no $W_{18}O_{49}$ phase is detected during the 2-step conversion. Considering of the reducing process such as temperature and reactants for both methods, the difference may drive from what is the actual reducing agent under different circumstances. Thermodynamically, C and H_2 are capable to reduce WO_3 starting from 300 K (**Figure 4.12**), and carbon exhibits a better reducing capability, especially at high temperature. However, H_2 reducing is dominated at a lower temperature (i.e. 1025K) since the reduction driving force from both C and H_2 is similar, while H_2 has a higher diffusion capability. This is verified by the XRD result in **Figure 4.13a**.

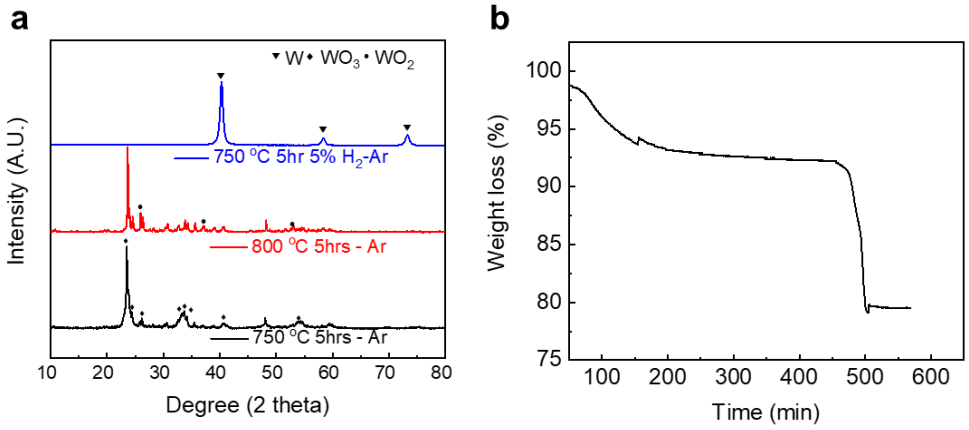

Figure 4.13 (a) XRD patterns of C-WO_3 prepared under different reducing conditions. 750 °C for 5 hours with a heating rate of 5 °C min^{-1} under 5% H_2-Ar (blue). 800 °C for 5 hours with a heating rate of 5 °C min^{-1} under Ar (red). 750 °C for 5 hours with a heating rate of 5 °C min^{-1} under Ar (black). (b) The TG result of C-WO_3 sample heated under Ar and hold at 750 °C for 5 hours. The mass changed from 93.6 to 92.3 wt% after 5 hours.

The WO_3 is completely converted into W under 5% H_2-Ar without any carbon agent at 750 °C for 5 hours. Result of the C-WO_3 mixture under Ar shown in **Figure 4.13a** is still WO_3 phase. Also, TG exhibits that only 1% weight loss after hold the sample at the same condition (**Figure 4.13b**), so the reduction effect of C to WO_3 at 750 °C is negligible. On the other hand, when temperature increases, C starts to participate into the reduction process. For example, WO_2 is generated after the C-WO_3 mixture keeping at 800 °C for 3 hours under Ar (**Figure 4.13a**). All results are well matched with the thermodynamic calculation in **Figure 4.11**. Therefore, the possible reaction mechanisms for different methods are proposed in **Figure 4.14**.

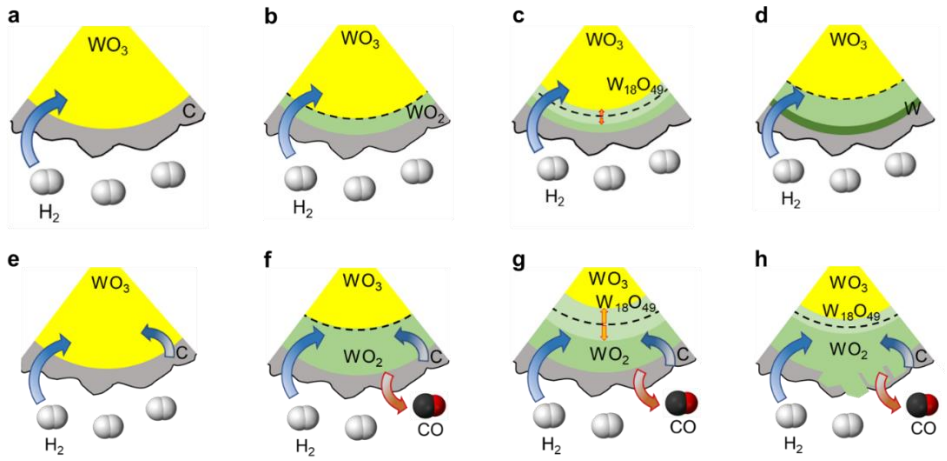

Figure 4.14 Schematic illustration of phase transition process for the 2-step conversion (a-d) and the 1-step conversion (e-f).

When the temperature is maintained at 750 ^{o}C, WO_2 thin layer is formed at the interface first between the outside carbon layer and WO_3 only by H_2 reduction (**Figure 4.14b**), which promotes the further reduction of inside WO_3 and generated a $W_{18}O_{49}$ intermediate phase as a boundary between WO_3-WO_2 layers (**Figure 4.14c**). Due to the large negative reaction energy (**Figure 4.11c**), such a $W_{18}O_{49}$ boundary is readily to be further reduced to WO_2, consistently moving inward. The outer area where is WO_3-scarced with rich H_2 can only be reduced to W (**Figure 4.14d**). Kinetically, the activation energy of $W_{18}O_{49}$ – WO_2 is the lowest among the series of WO_x reductions (**Table 4.1**), suggesting a fast conversion from $W_{18}O_{49}$ to WO_2 in the circumstance of sufficient supply of reductant. Considering the overall reduction of WO_3 is sluggish, this intermediate phase is difficult to detect by the lab-source XRD so it doesn't capture.

Table 4.1. Activation energies of various WO_x under reduction[80]

Reaction step	E_a (KJ/mol)
$WO_3 \leftrightarrow W_{10}O_{29}$	98.2
$W_{10}O_{29} \leftrightarrow WO_{2.72}$	70.45
$WO_{2.72} \leftrightarrow WO_2$	69.94
$WO_2 \leftrightarrow W$	84.21

On the other hand, carbon starts to participate into the reduction when temperature is ramping over 750 ^oC (**Figure 4.14f**). Together with faster reaction kinetics, a large amount of WO_2 is generated in a short time by H_2 and C, which is consistent with the XRD refinement result (**Figure 4.10c**). Then the WO_2 at the WO_3 interface tend to convert into $W_{18}O_{49}$ (**Figure 4.14g**). As temperature keeps increase, the fast $W_{18}O_{49} – WO_2$ starts to limit by the diffusion process of reactants such as C and H_2, especially when solid diffusion of carbon has a much lower diffusion coefficient that H_2. Therefore, more $W_{18}O_{49}$ tends to accumulate in the system, and it is easier to detect by XRD.

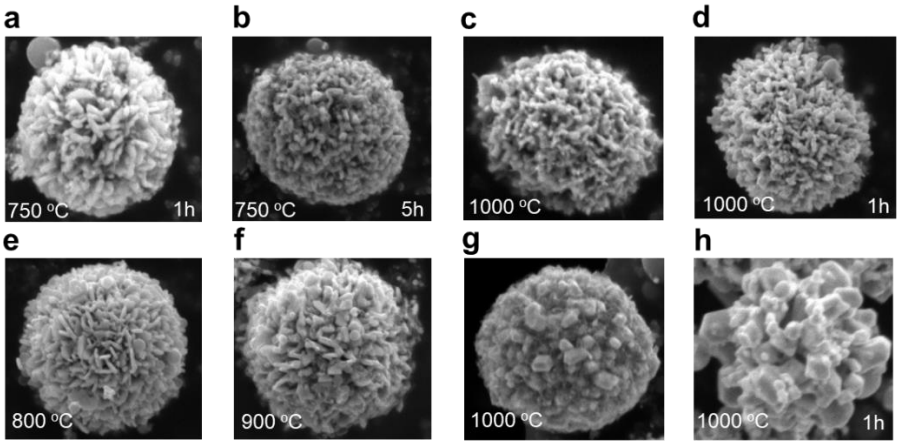

Figure 4.15. SEM images of the morphology evolution of WO_x-W-W_xC for the 2-step conversion (a-d) and the 1-step conversion (e-f)

To study the morphology evolution process. SEM images were collected at different stages of reactions and the results are presented in **Figure 4.15**. Although slightly morphology deformation of the primary nano-plates with degraded corner appears, the secondary spherical structure of WO_3 is well-maintained even after fully converted into WC after holding at 1000 ºC for 3 hours for the 2-step conversion (**Figure 4.15a-d**). Whereas the shape characteristics of WO_3 precursor can barely preserve after the 1-step transition: The sign of structure deformation starts from the WO_3 reduction process, at the temperature between 800 – 900 ºC, when the carbon starts to play roles in reduction. Initially, part of the nano-plates loses their corners into a round shape and gain dimensions in their thickness. As temperature reaches 1000 ºC, the fast phase conversion process brings all nano-plates primary particles into chunk particles, and final carbonization process at 1000 ºC drives the collapse of the spherical structure into polyhedrons with different sizes.

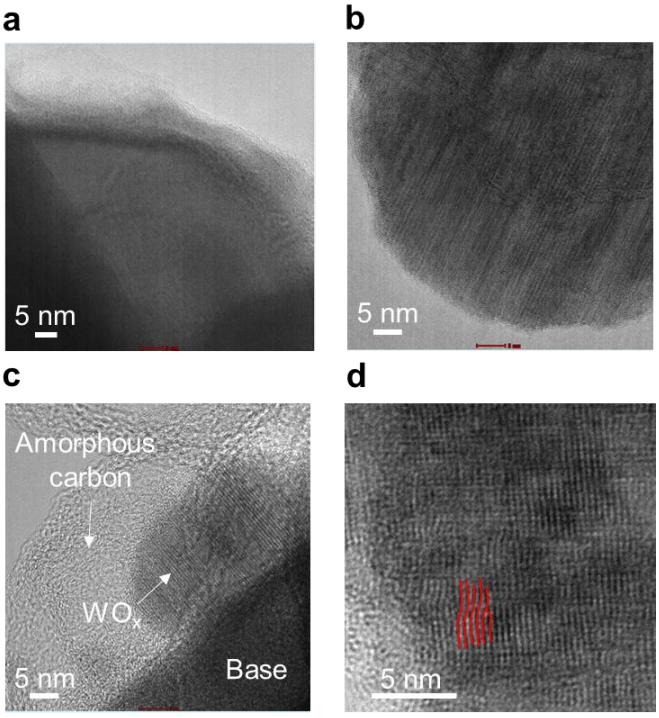

Figure 4.16 (a) TEM images of the edge of C-WO_3 particle during the 1st stage of reduction in the 2-step method at 750 ºC for 3 hours. (b) TEM images of the edge of C-WO_3 particle in the 1-step method at 900 ºC. (c) TEM image of a nanoparticle growth out from the WO_x-C interface preprared by the 1-step method at 900 ºC. (d) Defects such as dislocation on the edge of one particle prepared by the 1-step method at 900 ºC.

Obviously, the structure change stems from the WO_3 reduction process under different heating conditions, and TEM results in **Figure 4.16** display more information to establish relations between the phase and morphology transition process. For the 2-step conversion, even at the end of the reduction process, the W crystal structure is inaccessible due to the well-preserved amorphous carbon coating layer (**Figure 4.16a**), while the carbon layer is consumed (**Figure 4.16b**) rapidly during the 1-step conversion. Rob-like structure stretched out from the WO_x bulk into the carbon amorphous layer (**Figure 4.16c**), and defects such as dislocation are found in at the edge of the particle **(Figure 4.16d)**, which may be attributed to the fast phase transition process during the 2-step conversion.

Such lattice strain variations may lead to the final collapse of the original structure. To further investigate the variations of lattice strain during the reduction process for both methods, the Williamson-Hall equation[81] was employed to extract data from XRD and the results are shown in **Figure 4.17**. It confirms that WO_3 experienced a higher lattice strain under the 1-step conversion process. So the lattice strain could be an indicator for the degradation of structure. Here, few possibilities would be responsible for the increase of lattice strain and structure change. The rapid reduction and/or the carbothermal reduction. The XRD result in **Figure 4.13a** already demonstrates that when C-coated WO_3 was annealed at 800 ^oC under Ar for 5 hours, the carbothermal reduction is feasible but slow. But the SEM image in **Figure 4.18a** exhibits morphology change, which is totally different than the sample annealed at 750 ^oC (**Figure 4.18b**). Although the overall shape of the spherical secondary particle is still recognizable, but some rods growth out on the surface. On the other hand, although pristine WO_3 reducing at 750 ^oC under 5% H_2-Ar for 5 hours completely transforms into W (**Figure 4.18c**), the structure is destroyed. So both the reaction rate and reducing agent matters in terms of morphology maintenance.

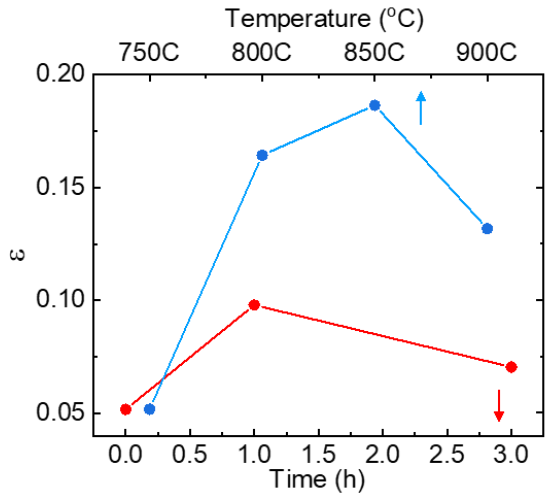

Figure 4.17. Lattice strain variations of WO_3 under different status during the synthesis process of 1-step conversion (blue) and 2-step conversion (red).

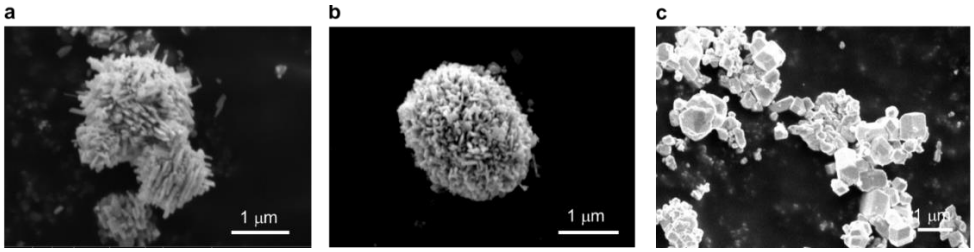

Figure 4.18. Lattice strain variations of WO_3 under different status during the synthesis process of 1-step conversion (blue) and 2-step conversion (red).

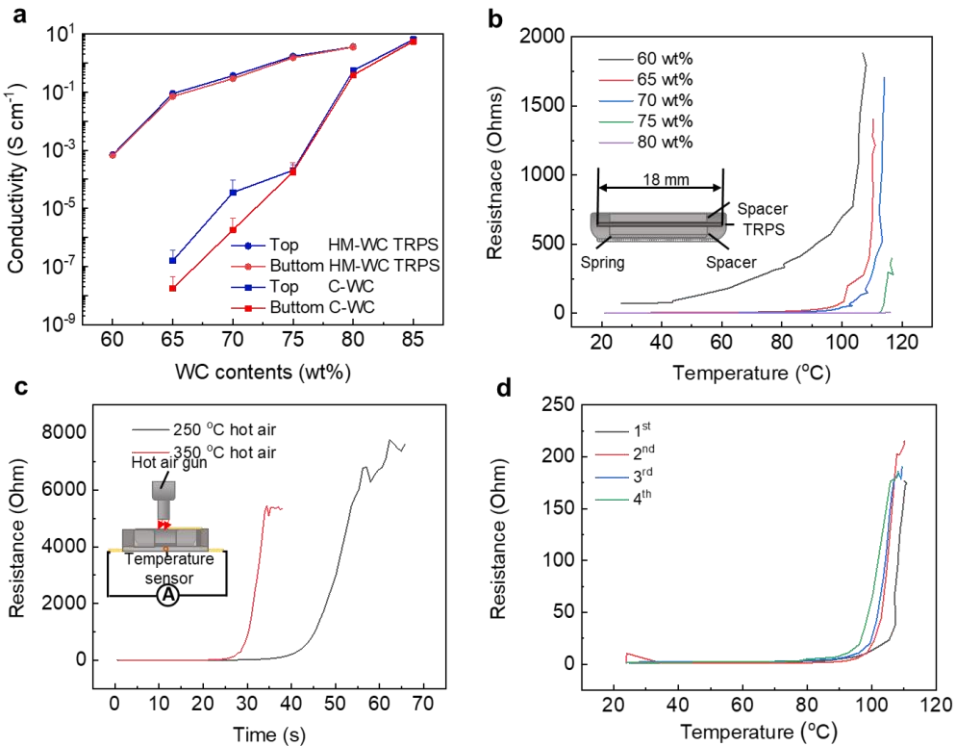

Figure 4.19. (a) Surface conductivity of WC/PE TRPS films as a function of the WC ratio for both commercial WC (C-WC) and as-synthesized WC (HM-WC). (b) Thermal switching response of TRPS with different WC ratios under the overheating conditions (120 ºC), the inset is the configuration of the switching response test in the vertical direction. (c) Resistance response of 70WC-TRPS upon different heating rate through a hot-air gun (hot-air temperature set as 250 ºC and 350 ºC). (d) Switching reversibility of 70WC-TRPS when it was repeated exposed at a 120 ºC environment.

The as-synthesized WC was used as the conductive filler for TRPS. The electrical conductivities of WC/PE system based on commercial WC (C-WC) and as-synthesized WC (HM-WC) as a function of WC contents are shown in **Fig 4.19a**. Overall, TRPS embedded with as-synthesized WC exhibits a higher electrical conductivity, especially when the WC loading is low. A boost of electrical conductivity over 10^5 order can be achieved. The electrical conductivity raises from a 0.083 S cm^{-1} to 3.86 S cm^{-1} as the WC contents increase from 65 to 80 wt%, while corresponding values for C-WC based TRPS are only 1.59×10^{-7} S cm^{-1} to 0.41 S cm^{-1}, respectively. In addition, uniform and narrow

size distribution of HM-WC enables a better consistency of electrical conductivity. No variations of conductivity on both surfaces. However, surface conductivities of TRPS integrated with C-WC appeared to be inconsistent.

To evaluate the thermal response capability of resistance against temperature under extreme thermal abuse conditions, TRPSs were exposed to a 120 ºC[68] convection oven and corresponding resistance vibrations were recorded in **Figure 4.19b** TRPSs displayed different on-site temperature and PTC intensity with different WC ratios. TRPS can show feedback to temperature at only 40 ºC when the WC ratio drops to 60 wt%, while it can be impervious even at 120 ºC as the WC contents reach 80 wt%. Such a wide temperature response range guarantees TRPS can be qualified for various applications.[82] Specifically, WC-65/70 are compatible for battery safety application since they demonstrated high on-site temperature (~90 ºC) and large PTC intensities (~2.85), which ensure batteries can operate normally at high temperature (i.e. 50 ºC) but can be shut down under overheating environment (~90-110 ºC). Resistance stability of 70TRPS was monitored under 50 ºC and 90 ºC for further confirmation (**Figure 4.21a**). No obvious change of the resistance when the TRPS immersed in a 50 ºC environment, while the resistance generally increase and stable at ~700 **Ω** in a 90 ºC convection oven.

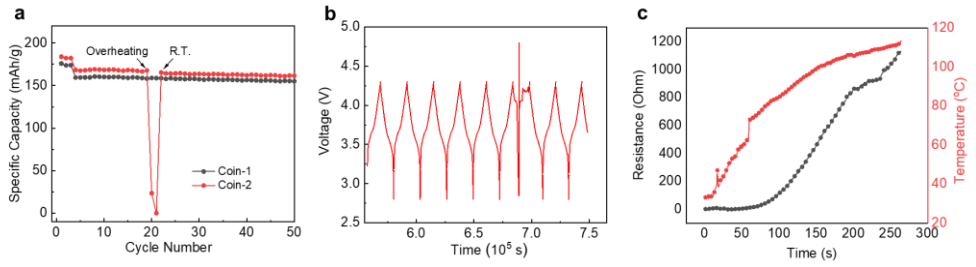

Figure 4.20 (a) Cycling stability of the safety-improved TRPS coin cell and the control cell without using any TRPS. The TRPS cells can tolerate overheating by switching off and resume its normal cycling after cooling down to R. T. condition (red line). (b). Charge-discharge curves of the safety-improved TRPS coin cell before and after thermal shut down in a 120 °C convection oven. (c) Resistance and temperature changes as a function of time for a safety-improved TRPS coin cell during a thermal abuse.

What's more, the switching response rate and PTC intensity are highly correlated to the abuse conditions. **Figure 4.19c** illustrates the resistance response curve against different overheating scenarios. TRPSs react to temperature variations more rapid and intense when encounter violent temperature fluctuations. For example, TRPS with 70wt % WC displays faster response to thermal abuse under heating of 350 °C hot air than that from 250 °C hot air, and both show larger PTC intensities (3.3-3.47). Details of temperature, resistance behaviors against time are in **Figure 4.21b**. Such properties further enhance the protective capability of TRPS for some extreme conditions such as potential local overheating due to internal short. Also, resistance reversibility was examined and shown in **Figure 4.19d**. The resistance response to abuse environment (120 °C oven) exhibit a good repeatability for cycles.

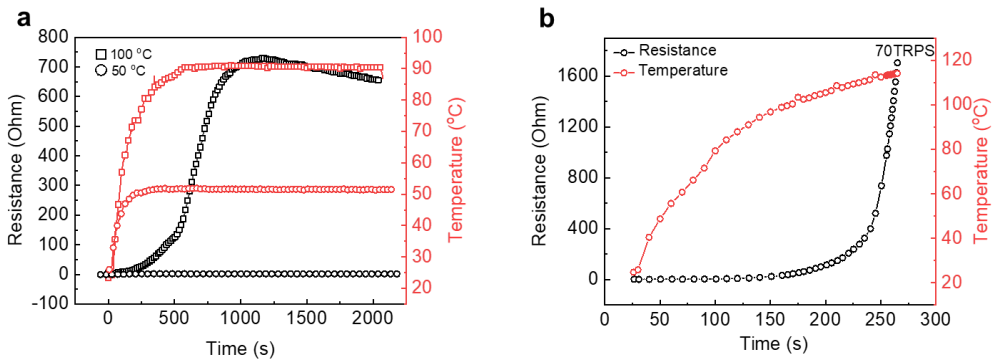

Figure 4.21 (a) Thermal stablity tests of resistance for 70WC-TRPS film in a convection oven held at 50 ºC and 100 ºC for 1500s. (b) Resistance and temperature changes as a function of time for a 70WC-TRPS film during a thermal abuse.

70TRPS-integrated coin cells (NCM 622 ‖ Gr) were fabricated to evaluate cycle performance and capability of abuse protection. As shown in **Figure 4.20a**, the cell fabricated with 70TRPS delivered the same capacity and cycle retention as the control cell. Furthermore, the cell can be totally shutdown if it is placed in an overheating environment (110 ºC), and it can resume back to normal operation once the temperature drops down to R.T. Specifically, the voltage of cells approached lower cut off rapidly when it suffered from high temperature, and during the charge process, it hit the protection cutoff voltage immediately (**Figure 4.20b**), which indicates the large internal resistance of the cell. To be more persuasive, the dynamic change of resistance with time was plotted in **Figure 4.20c**. Internal resistance accumulated up to 1200 Ω when the cell temperature reached ~110 ºC, guaranteed a complete shutoff of the cell and prevent the generation of joule heat.

4.2.3. Conclusion

In summary, we design a new synthesis strategy to obtain carbides (e.g. Tungsten carbide, Molybdenum carbide) with controllable morphology by a 2-step conversion method as conductive fillers of TRPS. Systematic studies of the phase and morphology evolutions by ex-situ X-ray diffraction, scanning electron microscope and transmission electron microscope illustrates that the reducing agent and reduction rate are critical for morphology maintenance. As a result, TRPS embedded with as-synthesized WC with a desired shape exhibits more than 5 order of conductivity improvement, demonstrating reversible shutdown performance and provide effective thermal abuse protection of LIBs.

4.2.3. Acknowledgement

Chapter 4, in full, is a reprint of the material "Synthesis of Appearance Controllable Carbides as Conductive Fillers of Thermo-Responsive Polymer Nanocomposites for Battery Safety" as it is in preparation, Mingqian Li, Hongpeng Gao, Zheng Chen. The dissertation author was the first author of this paper and conducted all the essential research work.

Chapter 5. Summary and Outlook

Integrating TRPS materials into LIBs has been demonstrated to be an effective strategy to provide safety protection against thermal abuses intrinsically in both coin cells and industrial pouch cells level. A solvent-based fabrication method of TRPS was developed to prepare TRPS directly on current collector, which can be easily transplanted into the electrode production section for potential large-scale applications. The limitation of TPRS was pushed and Ni-based TRPS materials with a higher electrical conductivity and large energy density were obtained. A novel method was designed to synthesize appearance controllable carbides, and tungsten carbide was used as a new class of conductive fillers for TRPS materials for the first time. All results indicate that TRPS material is a promising option for safer batteries.

However, there are still plenty of spaces that researchers can focus on to further improve the safety of LIBs. At the top of that, a fundamental understanding of the LIBs failure mechanism is still needed to explore and clarify. Although enormous experimental results have already pointed out that no matter what abuses scenarios the battery suffers from (*i.e.* thermal abuses, electrical abuses and mechanical abuses), all of them end up with uncontrolled heat accumulations and thermal runaway, but the difficulty is how to deconvolute usefully information from the experiments: the interval time between the initiation of internal short caused by different abuses and the following thermal runaway and explosion is just in seconds, for most case researchers can only collect and analyze data from the result of experiments. Real-time and local information inside the batteries related to the chemical reactions or the temperature/current/voltage is difficult to obtain.

Advanced and accurate characterizations need to develop and utilize to extract the critical data which is responsible for the collapse of batteries.

Since the uncontrollable heat accumulations are the consequence of different abuses also the trigger of catastrophic thermal runaway. The thermal regulation of the battery system by TRPS should gain more attention from the community. And for a typical process of thermal runaway. there are 3 stages: First is the onset of overheating, then is the accumulation of heat, and the last is the combustion and explosion. So, strategies should be designed to stop or retard the development of thermal runaway from all stages. The top priority should be the inhibit the start of overheating. And TRPS material is one of the most promising candidates since it can provide consistent and reversible protection for the batteries. The next generation of TRPS materials should be part of current battery components, instead of an extra layer since it compromises the energy density. It could be integrated into the current collector, but the mechanical strength is a potential issue. It also could be a component of the electrodes, acts as the role as binder in the electrode. For the second stage, to stop the accumulation of heat, it requires TRPS responds to temperature but react to the chemical or electrochemical reactions. To stop the electrochemical reactions, cutting off the flow of ions or the electrons is the only method. In abuse conditions, physical blocking the transfer of electrons/ions would be an effective way. For the chemical reactions, isolating the reactants / lower local temperature can slow the reaction. These require extra functions should be developed for TRPS. For example, TRPS with a polymer matrix which has a large thermal capacity or phase change capability during the heating accumulation window are preferred. For the last stage, Additives with some functional groups which

can work as fire retardants can be added into the TRPS to increase the difficulty of catching fire.

References

1. Energy Information Administration, Annual Energy Outlook 2021. https://www.eia.gov/outlooks/aeo/ **2021**.

2. BloombergNEF, Electric Vehicle Outlook 2020. https://about.bnef.com/electric-vehicle-outlook/ **2021**.

3. Li, W.; Zhu, J.; Xia, Y.; Gorji, M. B.; Wierzbicki, T., Data-Driven Safety Envelope of Lithium-Ion Batteries for Electric Vehicles. *Joule* **2019,** *3* (11), 2703-2715.

4. Xiong, R.; Li, L.; Tian, J., Towards a smarter battery management system: A critical review on battery state of health monitoring methods. *Journal of Power Sources* **2018,** *405*, 18-29.

5. Kang, D.; Lee, P.-Y.; Yoo, K.; Kim, J., Internal thermal network model-based inner temperature distribution of high-power lithium-ion battery packs with different shapes for thermal management. *Journal of Energy Storage* **2020,** *27*.

6. Gonzalez, M. S.; Yan, Q.; Holoubek, J.; Wu, Z.; Zhou, H.; Patterson, N.; Petrova, V.; Liu, H.; Liu, P., Draining Over Blocking: Nano-Composite Janus Separators for Mitigating Internal Shorting of Lithium Batteries. *Adv Mater* **2020,** *32* (12), e1906836.

7. Tim Dagger, B. R. R., Falko M. Schappacher, and Martin Winter, Comparative Performance Evaluation of Flame Retardant Additives for Lithium Ion Batteries – I. Safety, Chemical and Electrochemical Stabilities. *Energy Technology* **2018,** *6*, 1-13.

8. Sun, H.; Zhu, G.; Zhu, Y.; Lin, M. C.; Chen, H.; Li, Y. Y.; Hung, W. H.; Zhou, B.; Wang, X.; Bai, Y.; Gu, M.; Huang, C. L.; Tai, H. C.; Xu, X.; Angell, M.; Shyue, J. J.; Dai, H., High-Safety and High-Energy-Density Lithium Metal Batteries in a Novel Ionic-Liquid Electrolyte. *Adv Mater* **2020,** *32* (26), e2001741.

9. Yang, H.; Guo, C.; Chen, J.; Naveed, A.; Yang, J.; Nuli, Y.; Wang, J., An Intrinsic Flame-Retardant Organic Electrolyte for Safe Lithium-Sulfur Batteries. *Angew Chem Int Ed Engl* **2019,** *58* (3), 791-795.

10. Jiang, T.; He, P.; Wang, G.; Shen, Y.; Nan, C. W.; Fan, L. Z., Solvent‐Free Synthesis of Thin, Flexible, Nonflammable Garnet‐Based Composite Solid Electrolyte for All‐Solid‐State Lithium Batteries. *Advanced Energy Materials* **2020,** *10* (12).

11. Chen, Z.; Hsu, P.-C.; Lopez, J.; Li, Y.; To, J. W. F.; Liu, N.; Wang, C.; Andrews, Sean C.; Liu, J.; Cui, Y.; Bao, Z., Fast and reversible thermoresponsive polymer switching materials for safer batteries. *Nat. Energy.* **2016,** *1* (1).

12. Li., J.; Chen., J.; Lu, H.; Jia, M.; Jiang, L.; Lai, Y.; Zhang, Z., A Positive-Temperature-Coefficient Layer Based on Ni-Mixed Poly(Vinylidene Fluoride Composites for LiFePO4 Electrode. *Int. J. Electrochem. Sci.* **2013,** *8*, 5223 - 5231.

13. Feng, X. M.; Ai, X. P.; Yang, H. X., A positive-temperature-coefficient electrode with thermal cut-off mechanism for use in rechargeable lithium batteries. *Electrochem. Commun.* **2004,** *6* (10), 1021-1024.

14. Song, R.; Fang, R.; Wen, L.; Shi, Y.; Wang, S.; Li, F., A trilayer separator with dual function for high performance lithium–sulfur batteries. *J. Power Sources* **2016,** *301*, 179-186.

15. Balakrishnan, P. G.; Ramesh, R.; Prem Kumar, T., Safety mechanisms in lithium-ion batteries. *J. Power Sources* **2006,** *155* (2), 401-414.

16. Zhai, Y.; Wang, N.; Mao, X.; Si, Y.; Yu, J.; Al-Deyab, S. S.; El-Newehy, M.; Ding, B., Sandwich-structured PVdF/PMIA/PVdF nanofibrous separators with robust mechanical strength and thermal stability for lithium ion batteries. *J. Mater. Chem. A* **2014,** *2* (35), 14511-14518.

17. Liao, H.; Zhang, H.; Qin, G.; Hong, H.; Li, Z.; Lin, Y.; Li, L., Novel Core-Shell PS-co-PBA@SiO2 Nanoparticles Coated on PP Separator as “Thermal Shutdown Switch” for High Safety Lithium-Ion Batteries. *Macromol Mater Eng* **2017,** *302* (11).

18. Li, J.; Huang, Y.; Zhang, S.; Jia, W.; Wang, X.; Guo, Y.; Jia, D.; Wang, L., Decoration of Silica Nanoparticles on Polypropylene Separator for Lithium-Sulfur Batteries. *ACS Appl Mater Interfaces* **2017,** *9* (8), 7499-7504.

19. K. Liu, W. L., Y. Qiu, B. Kong, Y. Sun, Z. Chen, D. Zhuo, D. Lin, and Y. Cui, Electrospun core-shell microfiber separator with thermal-triggered flame-retardant properties for lithium-ion batteries. *Sci. Adv* **2017,** *3* (1601978).

20. Behl, W. K.; Chin, D.-T., Electrochemical Overcharge Protection of Rechargeable Lithium Batteries II. Effect of Lithium Iodide-Iodine Additives on the Behavior of Lithium Electrode in LiAsF6Tetrahydrofuran Solutions. *J. Electrochem. Soc.* **1988,** *135* (1), 21-25.

21. Golovin, M. N.; Wilkinson, D. P.; Dudley, J. T.; Holonko, D.; Woo, S., Applications of Metallocenes in Rechargeable Lithium Batteries for Overcharge Protection. *J. Electrochem. Soc.* **1992,** *139* (1), 5-10.

22. Buhrmester, C.; Moshurchak, L. M.; Wang, R. L.; Dahn, J. R., The Use of 2,2,6,6-Tetramethylpiperinyl-Oxides and Derivatives for Redox Shuttle Additives in Li-Ion Cells. *J. Electrochem. Soc.* **2006,** *153* (10), A1800-A1804.

23. Zhang, L.; Zhang, Z.; Wu, H.; Amine, K., Novel redox shuttle additive for high-voltage cathode materials. *Energy Environ. Sci.* **2011,** *4* (8).

24. Wang, Q.; Ping, P.; Zhao, X.; Chu, G.; Sun, J.; Chen, C., Thermal runaway caused fire and explosion of lithium ion battery. *J. Power Sources* **2012,** *208*, 210-224.

25. Zhong, H.; Kong, C.; Zhan, H.; Zhan, C.; Zhou, Y., Safe positive temperature coefficient composite cathode for lithium ion battery. *J. Power Sources* **2012,** *216*, 273-280.

26. Zhang, X.; Zheng, X.; Ren, D.; Liu, Z.; Yang, W.; Yang, M., Unusual positive temperature coefficient effect of polyolefin/carbon fiber conductive composites. *Mater. Lett.* **2016,** *164*, 587-590.

27. Kim, J.-i.; Kang, P. H.; Nho, Y. C., Positive Temperature Coefficient Behavior of Polymer Composites Having a High Melting Temperature. *J. Appl. Polym. Sci.* **2004,** *92*, 394–401.

28. Xia, L.; Zhu, L.; Zhang, H.; Ai, X., A positive-temperature-coefficient electrode with thermal protection mechanism for rechargeable lithium batteries. *Chin. Sci. Bull.* **2012,** *57* (32), 4205-4209.

29. Ji, W.; Wang, F.; Liu, D.; Qian, J.; Cao, Y.; Chen, Z.; Yang, H.; Ai, X., Building thermally stable Li-ion batteries using a temperature-responsive cathode. *Journal of Materials Chemistry A* **2016,** *4* (29), 11239-11246.

30. Simmons, J. G., Generalized Formula for the Electric Tunnel Effect between Similar Electrodes Separated by a Thin Insulating Film. *J. Appl. Phys.* **1963,** *34* (6), 1793-1803.

31. Park, J. W.; Chae, E. H.; Kim, S. H.; Lee, J. H.; Kim, J. W.; Yoon, S. M.; Choi, J.-Y., Preparation of fine Ni powders from nickel hydrazine complex. *Mater. Chem. Phys.* **2006,** *97* (2-3), 371-378.

32. Guan, J.; Liu, L.; Xu, L.; Sun, Z.; Zhang, Y., Nickel flower-like nanostructures composed of nanoplates: one-pot synthesis, stepwise growth mechanism and enhanced ferromagnetic properties. *CrystEngComm* **2011,** *13* (7).

33. Zhang, Y. F.; Zhang, L. Y.; Wang, J.; Wei, L. M.; Liu, P.; Wei, H., Synthesis of Ni nanowires via a hydrazine reduction route in aqueous ethanol solutions assisted by external magnetic fields. *Nano-Micro Letters* **2010,** *1* (1).

34. Cartwright, M., Investigation of Preparation, Solubility and Stability Properties of Nickel Hydrazine Nitrate (NiHN). *Propellants, Explosives, Pyrotechnics* **2018,** *43* (12), 1270-1276.

35. Aghazadeh, M.; Ghaemi, M.; Sabour, B.; Dalvand, S., Electrochemical preparation of α-Ni(OH)2 ultrafine nanoparticles for high-performance supercapacitors. *J. Solid State Electrochem.* **2014,** *18* (6), 1569-1584.

36. Chen, J. P.; Lim, L. L., Key factors in chemical reduction by hydrazine for recovery of precious metals. *Chemosphere* **2002,** *49*, 363–370.

37. Biesinger, M. C.; Payne, B. P.; Grosvenor, A. P.; Lau, L. W. M.; Gerson, A. R.; Smart, R. S. C., Resolving surface chemical states in XPS analysis of first row transition metals, oxides and hydroxides: Cr, Mn, Fe, Co and Ni. *Appl. Surf. Sci.* **2011,** *257* (7), 2717-2730.

38. Prieto, P.; Nistor, V.; Nouneh, K.; Oyama, M.; Abd-Lefdil, M.; Díaz, R., XPS study of silver, nickel and bimetallic silver–nickel nanoparticles prepared by seed-mediated growth. *Appl. Surf. Sci.* **2012,** *258* (22), 8807-8813.

39. Xing, W.; Qiao, S.; Wu, X.; Gao, X.; Zhou, J.; Zhuo, S.; Hartono, S. B.; Hulicova-Jurcakova, D., Exaggerated capacitance using electrochemically active nickel foam as current collector in electrochemical measurement. *J. Power Sources* **2011,** *196* (8), 4123-4127.

40. Goh, C. F.; Yu, H.; Yong, S. S.; Mhaisalkar, S. G.; Boey, F. Y. C.; Teo, P. S., The effect of annealing on the morphologies and conductivities of sub-micrometer sized nickel particles used for electrically conductive adhesive. *Thin Solid Films* **2006,** *504* (1-2), 416-420.

41. Michaelson, H. B., The work function of the elements and its periodicity. *J. Appl. Phys.* **1977,** *48* (11), 4729-4733.

42. D M Taylor, T. J. L., Electrical conduction in polyethylene terephthalate and polyethylene films
J. Phys. D: Appl. Phys. **1971,** *4*, 1346.

43. Jakubinek, M. B.; Ashrafi, B.; Zhang, Y.; Martinez-Rubi, Y.; Kingston, C. T.; Johnston, A.; Simard, B., Single-walled carbon nanotube–epoxy composites for structural and conductive aerospace adhesives. *Compos Part B Eng.* **2015,** *69*, 87-93.

44. Li, H.; Wang, F.; Zhang, C.; Ji, W.; Qian, J.; Cao, Y.; Yang, H.; Ai, X., A temperature-sensitive poly(3-octylpyrrole)/carbon composite as a conductive matrix of cathodes for building safer Li-ion batteries. *Energy Storage Materials* **2019,** *17*, 275-283.

45. Pourabbas, B.; Peighambardoust, S. J., PTC effect in HDPE filled with carbon blacks modified by Ni and Au metallic particles. *J. Appl. Polym. Sci.* **2007,** *105* (3), 1031-1041.

46. Frank, D. J.; Lobb, C. J., Highly efficient algorithm for percolative transport studies in two dimensions. *Phys Rev B Condens Matter* **1988,** *37* (1), 302-307.

47. Kan, X.; Ding, J.; Zhu, H.; Deng, C.; Yu, C., Low temperature synthesis of nanoscale titanium nitride via molten-salt-mediated magnesiothermic reduction. *Powder Technology* **2017,** *315*, 81-86.

48. Yang, M. M.; Peng, Z. J.; Wang, C. B.; Fu, X. L., Influence of $(Bi_{0.5}M_{0.5})TiO_3$ (M=Li, Na, K, Rb) Addition on the Curie Temperature and PTC Effect of $BaTiO_3$-Based Ceramics. *Key Engineering Materials* **2016,** *697*, 239-242.

49. Kono, A.; Shimizu, K.; Nakano, H.; Goto, Y.; Kobayashi, Y.; Ougizawa, T.; Horibe, H., Positive-temperature-coefficient effect of electrical resistivity below melting point of poly(vinylidene fluoride) (PVDF) in Ni particle-dispersed PVDF composites. *Polymer* **2012,** *53* (8), 1760-1764.

50. Lain; Brandon; Kendrick, Design Strategies for High Power vs. High Energy Lithium Ion Cells. *Batteries* **2019,** *5* (4).

51. JING, X.; ZHAO, W., The effect of particle size on electric conducting percolation threshold in polymer/conducting particle composites. *J. Mater. Sci. Lett.* **2000,** *19*, 377–379.

52. Kasnatscheew, J.; Evertz, M.; Streipert, B.; Wagner, R.; Nowak, S.; Cekic Laskovic, I.; Winter, M., Changing Established Belief on Capacity Fade Mechanisms: Thorough Investigation of $LiNi_{1/3}Co_{1/3}Mn_{1/3}O_2$ (NCM111) under High Voltage Conditions. *The Journal of Physical Chemistry C* **2017,** *121* (3), 1521-1529.

53. Hong, S.-I.; Rhim, J.-W., Preparation and properties of melt-intercalated linear low density polyethylene/clay nanocomposite films prepared by blow extrusion. *LWT - Food Science and Technology* **2012,** *48* (1), 43-51.

54. Yu, F.; Deng, H.; Bai, H.; Zhang, Q.; Wang, K.; Chen, F.; Fu, Q., Confine Clay in an Alternating Multilayered Structure through Injection Molding: A Simple and Efficient Route to Improve Barrier Performance of Polymeric Materials. *ACS Appl Mater Interfaces* **2015,** *7* (19), 10178-89.

55. Thompson, D. L.; Hartley, J. M.; Lambert, S. M.; Shiref, M.; Harper, G. D. J.; Kendrick, E.; Anderson, P.; Ryder, K. S.; Gaines, L.; Abbott, A. P., The importance of design in lithium ion battery recycling – a critical review. *Green Chemistry* **2020,** *22* (22), 7585-7603.

56. Akinlabi, A. A. H.; Solyali, D., Configuration, design, and optimization of air-cooled battery thermal management system for electric vehicles: A review. *Renewable and Sustainable Energy Reviews* **2020,** *125*.

57. Lei, T.; Chen, W.; Hu, Y.; Lv, W.; Lv, X.; Yan, Y.; Huang, J.; Jiao, Y.; Chu, J.; Yan, C.; Wu, C.; Li, Q.; He, W.; Xiong, J., A Nonflammable and Thermotolerant Separator Suppresses Polysulfide Dissolution for Safe and Long-Cycle Lithium-Sulfur Batteries. *Advanced Energy Materials* **2018,** *8* (32).

58. Baginska, M.; Sottos, N. R.; White, S. R., Core-Shell Microcapsules Containing Flame Retardant Tris(2-chloroethyl phosphate) for Lithium-Ion Battery Applications. *ACS Omega* **2018,** *3* (2), 1609-1613.

59. Doux, J. M.; Nguyen, H.; Tan, D. H. S.; Banerjee, A.; Wang, X.; Wu, E. A.; Jo, C.; Yang, H.; Meng, Y. S., Stack Pressure Considerations for Room‐Temperature All‐Solid‐State Lithium Metal Batteries. *Advanced Energy Materials* **2019,** *10* (1).

60. Doux, J.-M.; Yang, Y.; Tan, D. H. S.; Nguyen, H.; Wu, E. A.; Wang, X.; Banerjee, A.; Meng, Y. S., Pressure effects on sulfide electrolytes for all solid-state batteries. *Journal of Materials Chemistry A* **2020,** *8* (10), 5049-5055.

61. Joscha Schnell, T. G., Thomas Knoche, Christoph Vieider, Larissa Köhler,Alexander Just, Marlou Keller, Stefano Passerini, Gunther Reinhart, All-solid-state lithium-ion and lithium metal batteries–paving the way tolarge-scale production. *Journal of Power Sources* **2018,** *382*, 160-175.

62. Zheng Chen, P.-C. H., Jeffrey Lopez, Yuzhang Li, John W. F. To, Nan Liu, Chao Wang, Sean C. Andrews, Jia Liu, Yi Cui & Zhenan Bao, Fast and Reversible Thermo-Responsive Polymer Switching for Safer Batteries. *Nature Energy* **2016,** *1*.

63. Guo, X.; Li, L.; Liu, Z.; Yu, D.; He, J.; Liu, R.; Xu, B.; Tian, Y.; Wang, H.-T., Hardness of covalent compounds: Roles of metallic component and d valence electrons. *Journal of Applied Physics* **2008,** *104* (2).

64. Ghalkhani, M.; Bahiraei, F.; Nazri, G.-A.; Saif, M., Electrochemical–Thermal Model of Pouch-type Lithium-ion Batteries. *Electrochimica Acta* **2017,** *247*, 569-587.

65. Li, J.; Cheng, Y.; Ai, L.; Jia, M.; Du, S.; Yin, B.; Woo, S.; Zhang, H., 3D simulation on the internal distributed properties of lithium-ion battery with planar tabbed configuration. *Journal of Power Sources* **2015,** *293*, 993-1005.

66. Zhao, R.; Liu, J.; Gu, J., Simulation and experimental study on lithium ion battery short circuit. *Applied Energy* **2016,** *173*, 29-39.

67. Wang, Y.; Zheng, H.; Qu, Q.; Zhang, L.; Battaglia, V. S.; Zheng, H., Enhancing electrochemical properties of graphite anode by using poly(methylmethacrylate)–poly(vinylidene fluoride) composite binder. *Carbon* **2015,** *92*, 318-326.

68. Liu, X.; Ren, D.; Hsu, H.; Feng, X.; Xu, G.-L.; Zhuang, M.; Gao, H.; Lu, L.; Han, X.; Chu, Z.; Li, J.; He, X.; Amine, K.; Ouyang, M., Thermal Runaway of Lithium-Ion Batteries without Internal Short Circuit. *Joule* **2018,** *2* (10), 2047-2064.

69. Hansen, C.M., Hansen Solubility Parameters A Users Handbook, 2nd Ed ,ISBN-0849372488.

70. Ma, X., Zhao, L., Ji, G., Dong, Y.D; Preparation and structure of bulk nanostructured WC-Co alloy by high energy ball-milling. *J. Mater. Sci. Lett* **1997**, 16, 968-970.

71. Uribe, R., Baudin, C; Sub-micron sized Al_2TiO_5 powders prepared by high-energy ball milling, *J. Mater. Sci.* **2001**, 36, 5105-5113.

72. Porat, R.; Berger, S.; Rosen, A., Sintering Behavior and Mechanical Properties of Nanocrystalline WC/Co. *Materials Science Forum* **1996,** *225-227*, 629-648.

73. Oskarsson,R., Rönninge; US patent. US6228139B1, Fine-grained WC-Co cemented carbide.**2000**.

74. Seegopaul, P., Gao, L; US patent. US 6524366B1, Method of forming nanograin tungsten carbide and recycling tungsten carbide, **2000**.

75. Medeiros, F.F.P., De Oliveira, S.A., De Souza, C.P., Da Silva, A.G.P., Gomes,U.U., De Souza, J.F., Synthesis of tungsten carbide through gas–solid reaction at low temperatures, *Mater. Sci. Eng* **2001**, A315, 58-62.

76. Kim, J. C.; Kim, B. K., Synthesis of nanosized tungsten carbide powder by the chemical vapor condensation process. *Scripta Materialia* **2004,** *50* (7), 969-972.

77. Ong, S. P., Wang, L., Kang, B.W., Ceder, G; Li-Fe-P-O_2 Phase Diagram from First Principles Calculation. *Chem. Mater.* **2008**, 20, 1798–1807.

78. Aydıncak, K.; Yumak, T.; Sınağ, A.; Esen, B., Synthesis and Characterization of Carbonaceous Materials from Saccharides (Glucose and Lactose) and Two Waste Biomasses by Hydrothermal Carbonization. *Industrial & Engineering Chemistry Research* **2012,** *51* (26), 9145-9152.

79. Bianchini, M.; Wang, J.; Clement, R. J.; Ouyang, B.; Xiao, P.; Kitchaev, D.; Shi, T.; Zhang, Y.; Wang, Y.; Kim, H.; Zhang, M.; Bai, J.; Wang, F.; Sun, W.; Ceder,

G., The interplay between thermodynamics and kinetics in the solid-state synthesis of layered oxides. *Nat Mater* **2020,** *19* (10), 1088-1095.

80. Estupinan Donoso, A. A.; Peters, B., XDEM employed to predict reduction of tungsten oxide in a dry hydrogen atmosphere. *International Journal of Refractory Metals and Hard Materials* **2015,** *49*, 88-94.

81. Bindu, P.; Thomas, S., Estimation of lattice strain in ZnO nanoparticles: X-ray peak profile analysis. *Journal of Theoretical and Applied Physics* **2014,** *8* (4), 123-134.

82. Li, M.; Shi, Y.; Gao, H.; Chen, Z., Bio‐Inspired Nanospiky Metal Particles Enable Thin, Flexible, and Thermo‐Responsive Polymer Nanocomposites for Thermal Regulation. *Advanced Functional Materials* **2020,** *30* (23).